Sputter Deposition of Iridium and Iridium Oxide for Stimulation Electrode Coatings

Von der Fakultät für Elektrotechnik und Informationstechnik
der Rheinisch-Westfälischen Technischen Hochschule Aachen
zur Erlangung des akademischen Grades eines
Doktors der Ingenieurwissenschaften
genehmigte Dissertation

vorgelegt von
Diplom-Ingenieur
Börge Wessling

Berichter: Universitätsprofessor Dr. rer. nat. W. Mokwa
                 Universitätsprofessor Dr. rer. nat. H. Lüth

Tag der mündlichen Prüfung: 09.11.2007

Diese Dissertation ist auf den Internetseiten der Hochschulbibliothek online verfügbar.

Danksagung

Contents

Chapter 1

Introduction

1.1   Motivation

The interest in iridium (Ir) and iridium oxide (IrOx) has been growing due to their remarkable chemical, electrochemical and physical properties. Ir(Ox) has been evaluated for applications in a wide range of fields, including pH-sensing, electrochromic devices and optical information storage, chlorine or oxygen evolution, neural stimulation, field emission cathodes, and advanced memory technology.[1]

For the latter, IrOx as one of the few naturally highly conducting oxides can be used as electrode or diffusion barrier material for nonvolatile memory devices based on ferroelectric materials such as $Pb(Zr, Ti)O_3$ (PZT) [1–8]. The memory devices have to undergo 10^{11}-10^{13} read/write cycles [8], calling for extraordinary long-term reliability. Different from other electrode materials such as Pt, and based on high thermal and chemical stability, IrOx does not react with the capacitor environment during annealing steps and use. It further acts as an oxygen diffusion barrier, which inhibits the deterioration of ferroelectric and contact properties.

IrOx has recently attracted interest as an emitter or protective coating material in field emission cathode arrays, used in vacuum microelectronic devices or as displays [9–11]. The emission surface has to be stable in the presence of residual oxygen in the vacuum environment. Compared to conventional Ir/Pt/Au top electrodes, the performance is improved due to the chemical and thermal stability, a high diffusion resistance, and a low surface work function of 4.2 eV.

---

[1]In the course of this work, and following the majority of research published, the material is generally termed IrOx irrespective of particular chemical composition.

Most applications of IrOx are based on its electrochemical properties. One of the earliest investigated fields was electrochromism [12–16]. Rapid (within 50 msec [13]) and reversible coloration and bleaching of the material occurs during redox cycling in electrolyte. The material is transparent in the reduced state, and becomes blue-black in the oxidized state. Reflectance changes of up to 60% were reported, which, however, is less than values achieved with other materials such as Ni oxide [12]. Different electrochromic coloring mechanisms have been proposed, based on hydroxide and proton movement to the redox centers [15, 17, 18].

Similarly, IrOx has also been evaluated as material for optical information storage [19, 20]. Thermally induced dehydration of hydrated IrOx films resulted in regions of distinct transmission characteristics.

Regarding the use in potentiometric pH-sensing applications, IrOx thin film electrodes exhibit a fast and strong change in open circuit potential upon pH alterations. Furthermore, the material is stable over a wide pH range even under high temperatures and in aggressive environments [21–25]. The stability is one of the main reasons for its application as durable electrodes for chlorine or oxygen evolution [26–29].

A further important field is the use of IrOx as coating for electrodes in functional electrical stimulation [30–40]. The electrodes are used to electrically excite nerve cells. The application draws on biocompatibility, high electrochemical activity and corrosion resistance.

Ir(Ox) is employed for commercial heart pace maker or implantable defibrillator electrodes. As examples, Biotronik's Solox and Arox pacing leads are coated with Ir, and IrOx is used on Dr. Osypka's KY-5 permanent pacing lead.

The application as stimulation electrode coating is currently expanded to uses in functional medical implants based on micro systems technology. Smaller devices enable the bridging of disrupted functions at sites that have so far not been accessible. Furthermore, miniaturized implants have several advantages over existing large-dimensioned counterparts: Due to softness, flexibility and low weight, damage by the implant can be prevented. Adding to this, smaller implants allow the utilization of minimal invasive surgery. Moreover, these devices consume little power so that it can be transmitted in a wireless manner, rendering the use of batteries and cables unnecessary.

An example for an implantable functional device based on micro system technologies is the wireless Epi-Ret implant. It is supposed to generate an impression of vision in people that suffer from a progressive blindness due to degeneration of the retinal photo receptors [31]. Fig. 1.1 shows the second generation of implants. The receiver coil for energy and data transmission can be seen on the left. It is directly mounted onto a flexible foil. Receiver

and stimulator chip are assembled in the middle of the implant. An array of three-dimensional microelectrodes electrically stimulates retinal ganglion cells. The pulses are then transferred to the visual center via the visual nerve, both unaffected by the disease.
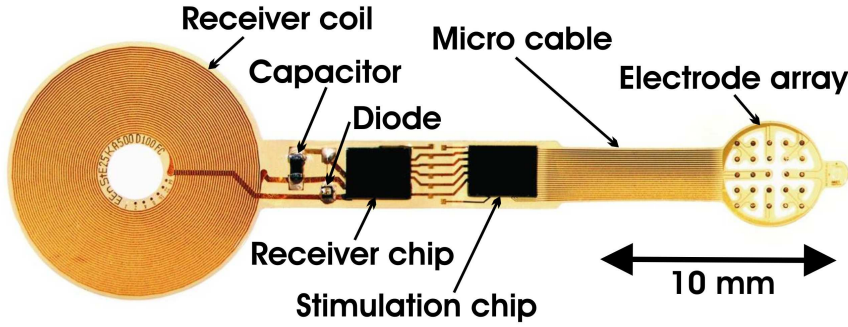
Figure 1.1: The Epi-Ret implant in its second generation. It includes a receiver coil for wireless data and energy transfer, receiver and stimulator chips, and an array of stimulation electrodes [31].

In order to evoke an action potential in neuronal cells, a certain amount of charge needs to be delivered to the tissue [41,42]. For safe stimulation, the electrode has to be capable of delivering this charge in a reversible manner, meaning that the critical potentials for gas evolution or electrode corrosion are not reached. The amount of reversibly transferred charge is determined by the electrode size and deliverable charge per area. The latter depends on the stimulation material.

An optimized material allows the design of smaller electrodes that are still able to deliver sufficient charge to depolarize neurons. A greater number of smaller electrodes can be integrated on the area available for the implant. This enhances the stimulation resolution, because a lower number of neurons is excited by the activation of one electrode.

In the Epi-Ret implant, an increased stimulation resolution corresponds to a higher number of independently triggered pixels, which can be reconstructed to an image by the intact visual center. An increase in charge delivery per area also allows a safety margin needed in case the excitation threshold of neurons increases. Furthermore, the lower interface impedance of an optimized electrode limits energy losses, which is important as the systems have to be trimmed for minimal power consumption.

Thus, the material has to enable high charge delivery, and provide a low impedance to the surrounding extracellular solution. Accordingly, there is a

need to further develop materials for stimulation electrode coatings. Apart from Ir(Ox), Pt, Ti or TiN can be used (as an example, Medtronic's implantable defibrillator lead CapSure Sense 4574 features a Pt-Ir alloy electrode with TiN coating). Electrode materials such as Ti or TiN stimulate neurons only capacitively, i.e. via the charging and discharging of the electrical double layer. Higher charges can be delivered using faradaic mechanisms. There, current flows across the electrode-electrolyte boundary due to reversible changes in oxidation states of the materials. Of electroactive materials such as Pt and Ir or IrOx, the latter have been shown to transfer the highest charges per geometrical area across the electrode-electrolyte boundary (see e. g. [35, 43–45] and references therein for material comparisons).

This thesis deals with the sputter deposition of Ir and IrOx as coatings of stimulation electrodes. The thin films are characterized regarding their capacity of transferring charge across an electrode-electrolyte boundary. Focussing on material development for macro-sized electrodes, the work details the relationships between sputter parameters, film growth, film microstructure and charge delivery capacity.

1.2   State of the art

1.2.1   Preparation of Ir and IrOx coatings

IrOx can be deposited by a variety of methods. For each of these techniques, the film characteristics such as chemical composition, porosity, crystallinity, and density depend on the exact process conditions.

The anodic growth of oxide from Ir metal films (anodic IrOx films, AIROF) is one of the most common techniques, and has often been reported on [27, 29, 33, 34, 46]. AIROF is formed by potential cycling of Ir in electrolyte within certain potential windows. It is mostly amorphous or nano-crystalline, highly hydrated and can be regarded as a gel-like material [47]. The starting metal layer can be deposited e. g. by electrochemical methods, by sputtering or by electron beam evaporation [35, 39]. The characteristics of the starting layer, especially its porosity, influence the growth of AIROF. At a high metal density, the growing AIROF can crack and delaminate due to stress developing between the metal and the less dense oxide [35].

The material prepared by electrolysis of solutions containing Ir complexes, e. g. K_3IrCl_6, is similar in characteristics [36, 48–50]. Electrodeposited IrOx films (EIROF) are less expensive to prepare than AIROF, as no Ir substrates are required. However, the preparation of the solution adds complexity to the process.

A further process is the thermal formation of IrOx [9,21,50,51]. It is either grown by pyrolysis of Ir salts such as $IrCl_3$, or via annealing of Ir in oxygen environment. Both routes require high temperatures of at least 400-500°C, and Cl residuals can remain in the case of pyrolysis [52].

Less common techniques include the growth of IrOx by sol-gel dip-coating from $IrCl_4$ solution [53], the pulsed laser deposition from Ir targets in reactive atmosphere [54, 55], and the deposition of IrO_2 nano-rods by metal oxide chemical vapor deposition [11, 56].

This work focusses on the sputtering of Ir(Ox) films (often called SIROF) [28,30,32,57,58]. The process combines several advantages: First, it is highly versatile and offers a wide range of process parameters. Second, electrodes of variable size can be deposited on various kinds of substrates. Third, sputtering is compatible with technologies used in the fabrication of microsystems, and does not introduce potentially harmful substances to the device. Finally, the deposited films can be activated anodically.

1.2.2 Sputtering of Ir and IrOx

During reactive sputtering, the plasma generates free radicals of the introduced reactive gas, allowing reactions with the target material on the substrate.

The general dependence of reactive gas partial pressure and deposition rate on reactive gas supply is illustrated by the generic curves of Fig. 1.2. Generic curves are well known from the analysis of reactive sputtering systems such as Ti-N or Ti-O, Zn-O or Al-O (see [59, 60] for reviews).

The reactive gas flow (i. e., oxygen flow) to the plasma is increased at constant power and Ar carrier gas pressure. The oxygen is at first consumed by the film growth, and does not notably increase the chamber pressure (Fig. 1.2). This condition prevails until at a certain stage, the oxygen supply to the chamber is greater than the getter rate of the growing film. At that point, reactive gas starts to adsorb at or even binds with the target material. The sputter yield decreases, leading to less gettering and stronger target poisoning. A rapid increase in reactive gas partial pressure is recorded, as well as a decrease in deposition rate. This transition point separates the metallic from the compound sputtering mode. Decreasing the oxygen supply from high values, the indicators shape a hysteresis, as shown in Fig. 1.2 [59].

Several authors have studied the above described effects for IrOx deposition by DC sputtering. The investigations applied mainly to deposition of electrodes or diffusion barriers for memory applications (mainly onto heated substrates, and followed by annealing) [1–3, 5, 61], but also for stimulation electrode coatings [30].
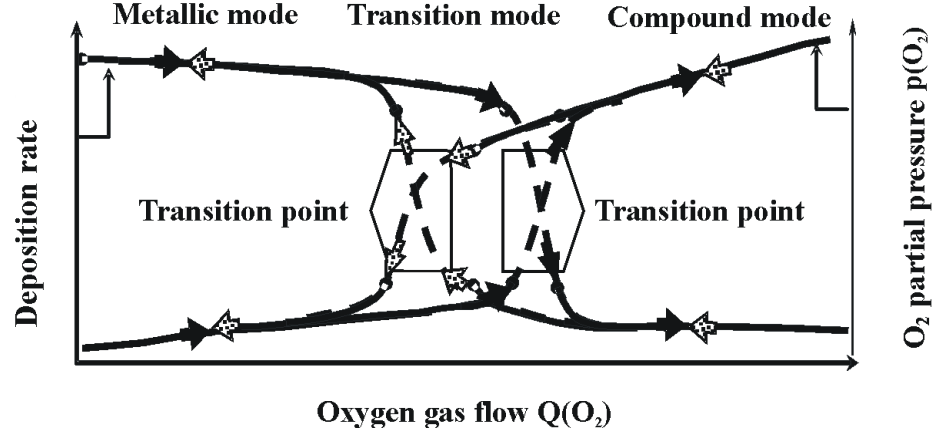
Figure 1.2: Generalized dependence of reactive gas partial pressure and deposition rate on the supply of reactive gas to the sputter chamber (from [30]).

The authors reported that the dependence of oxygen partial pressure on oxygen supply follows the above described trend and goes through a transition point. However, no hysteresis effect was found. This was explained by the target condition at high oxygen supplies: oxygen does not react, but rather adsorb at the target, and is quickly sputtered when the partial pressure decreases. Furthermore, the deposition rate dependence on oxygen gas supply was shown to behave differently from the general theory of Fig. 1.2: It increases to a maximum and then decreases again. The increase can be explained by the greater volume of the oxide phase forming under oxygen supply. The subsequent decrease results from the reduced sputter yield in the poisoned target mode.

The transition point is of great influence on the film properties. Dealing with application in memory technologies, Cho et al. [1] described morphology changes from smooth to rough and platelet structure with increasing oxygen supply. Furthermore, they linked the phase variations found by x-ray diffraction to sputtering in metallic or oxidized target mode. Similarly, Horng et al. [61] showed that an increase in oxygen supply leads to a decrease in film crystallinity. The lower ordering was explained by a lower surface mobility, and the oxidation of the used Si substrates. Phase formation analysis was employed by Fox et al. [2] to find the transition point. It marked significant changes in film stress and resistance.

Pinnow et al. [5] analyzed generic curves as a function of system pumping speed and input power. Similar to the previously mentioned works, the

deposition conditions could be separated into different regions depending on the target state and the oxygen integrated into the growing films. The importance of the evaluation of generic curves was pointed out, and film texture, stress, resistivity and the behavior during annealing were linked to the transitions between the regions.

Inoue and Hayashi [3] described a fabrication process for stacked Ir/IrO_2 random-access memory electrodes by varying the input power at constant oxygen and argon supply. At high sputter powers, more Ir metal is released from the target. Compared to reactive oxygen species, its supply overweighs on the substrate, and the IrO_2 phase becomes negligibly small. A reduction in power can be used to balance the arrival of metal and oxygen species.

With respect to application as stimulation electrode coatings, the most comprehensive investigations were performed by Slavcheva et al. [30]. IrOx was DC-sputtered onto cold substrates, under conditions previously analyzed by generic curves. It was shown that electrode impedance and charge delivery to an electrolyte strongly depend on the oxygen supply to the plasma. The changes were attributed to alterations of film surface morphology and roughness, however, the interrelations between sputter parameters, film growth and electrode characteristics were not detailed. The charge delivery and impedance characteristics were optimal at the transition point between metal and compound sputtering. Chemical analysis by x-ray photoelectron spectroscopy showed that unbound metal was present even at the highest oxygen flow rate. The thin films characteristics were stable over 150000 potential cycles in electrolyte.

Klein et al. [62] deposited onto wires in H_2O/O_2 atmospheres. The film consisted of platelets, which differed in orientation in dependence of the H_2O/O_2 ratio. The charge delivery decreased with an increasing fraction of platelets that were oriented perpendicular to the wire.

Enhanced electrochemical activity was linked to increasing IrOx film thickness by Cogan et al. [32]. The films exhibited an open, cauliflower-type appearance, however, the reason for their evolution was not discussed.

In the mentioned publications, changes in stimulation characteristics are related to film composition and the porosity of microstructures. However, the influence of process parameters on film growth, the resulting microstructure and the measured electrochemical performance is not investigated in detail. Furthermore, the published works focus solely on reactive DC sputtering, the reactive RF sputtering as well as Ir metal sputtering are not investigated.

Similarly, comparisons between RF and DC sputtering of IrOx have not yet been performed. RF- and DC-powered sputter deposition have been evaluated for other target materials [63–65], investigating energy flux to the substrate, energetic distributions of plasma species and differences in film

characteristics. As to reactively sputtered systems, the deposition and film characteristics of Ti-O, Cr-O [66], Al_2O_3 [67], ZnO:Al [68, 69], indium tin oxide [70] and In_2S_3 [71] were compared regarding the plasma excitation mode.

It was found that RF deposition rates are lower than those recorded during DC sputtering [66, 67, 69, 71]. In addition, the RF plasma is denser [63, 72], which results in a higher rate of dissociation of reactive species [66, 69]. It was also shown that the plasma region expands further from the target during RF sputtering [68]. Consequently, the flux of energetic plasma species to the growing film is higher [64, 65, 68], resulting in higher film densities.

1.2.3   Electrochemical performance of Ir and IrOx

In this work, the electrochemical activity of Ir and IrOx stimulation electrode coatings is assessed mainly by cyclic voltammetry (CV). Not only the material characteristics, but also measurement (electrolyte and scan rate [62]), evaluation procedure, and the number of potential cycles run on the sample before evaluation determine the achieved values (see section 2.2.1 for details on measurement and evaluation).

Measurements made on microelectrodes (diameters smaller than 300 μm) can not be compared to the ones presented here because of altered diffusion mechanisms at the microscale [73].

Considering only macro-sized electrodes and CV excitation, Table 1.1 gives an overview of literature data and commercially available materials. Not only sputtered IrOx films are included, but also electroplated IrOx films and those grown anodically from an Ir electrode.

1.3   Aims of the work

Ir and IrOx are used as thin film coatings of stimulation electrodes, but the mechanisms that allow the sputter deposition of electrochemically highly active coatings are not well understood. The goal of this work is to determine the processes and underlying effects enabling the deposition of Ir and IrOx thin films of high activity, suitable for use in miniaturized functional medical implants. The influence of a wide range of sputter deposition parameters on the evolving thin film microstructure, chemical composition and electrochemical behavior are characterized. This includes the understanding and modelling of film deposition in dependence of sputter parameters. Based on the results, prerequisites necessary for the optimization of electrochemical activity are outlined.

IrOx type	Q_a [mC/cm^2]	Electrolyte	Scan Rate [mV/s]	Ref.
AIROF	18.6	70 % H$_2$SO$_4$	100	[74]
AIROF	85	BBS$^{(*)}$, 80 $\Omega \cdot$ cm	100	[75]
AIROF	9.7	0.1M H$_2$SO$_4$	100	[38]
EIROF	30	PBS$^{(*)}$	50	[76]
SIROF	36	CBS$^{(*)}$	100	[57]
SIROF	95	0.9% NaCl	100	[30]
SIROF	30	0.5M H$_2$SO$_4$	100	[13]
SIROF	70	0.5M H$_2$SO$_4$	100	[28]
SIROF	31	0.5M H$_2$SO$_4$	10	[77]

Table 1.1: Literature values of anodic charge deliveries Q_a retrieved from cyclic voltammetry on IrOx films. Different IrOx formation methods (anodic, electroplated, sputtered) are considered. Apart from the material itself, the measurement results are strongly dependent on the used electrolyte and scan rate. The table only includes measurements on macro-sized electrodes.
$^{(*)}$BBS: bicarbonate buffered saline, PBS: phosphate buffered saline, CBS: carbonate buffered saline.

The thesis is organized as follows. After the outline of experimental details (chapter 2), chapter 3 includes the first comprehensive investigation of the general behavior of the reactively RF-sputtered IrOx system. The films are discussed with respect to application as stimulation electrode coating. The analysis focusses on the influence of oxygen integration into the growing film. Based on the evaluation of the deposition characteristics, the films are characterized regarding surface topography, chemical composition and electrochemical behavior.

In chapter 4, the reactive deposition of IrOx by DC and RF plasmas onto cold and heated substrates is compared for the first time. Furthermore, the electrochemical activation of IrOx is discussed and related to earlier published results pertaining to the activation of metallic Ir. The results allow to lay out the main mechanisms responsible for electrode performance.

The subsequent chapters include detailed investigations of the evolution of microstructure during sputtering. In chapter 5, an overview of literature is presented, dealing with the understanding of film growth during metal deposition. The protocols of simulations are presented that were written to model Ir sputter transport and film growth.

Chapter 6 contains the first comprehensive investigation regarding the microstructural design of metallic Ir. Experiment and simulation are used to characterize and optimize Ir sputter conditions regarding film morphology,

density, electrochemical characteristics, and texture. The film properties are evaluated as a function of energy and angular distributions of sputtered Ir atoms.

The experiments presented in chapter 7 combine all earlier findings of reactive sputtering, microstructural design and activation. The prerequisites for deposition of thin films of highest electrochemical activity are specified.

Chapter 2

Experimental

2.1 Sputter deposition

All sputter experiments were performed on a Nordiko NS 2550 top-down magnetron tool. Prior to sputtering, the chamber was evacuated to at least $4 \cdot 10^{-6}$ mbar by means of a cryogenic pump. All films were deposited in Ar or Ar/O_2 plasmas, prior to which a Ti adhesion layer of either 25 or 50 nm thickness was deposited on the oxidized Si substrates. The film thicknesses were determined via lift-off process with a Tencor P-10 profilometer, and totaled approximately 300-400 nm. All quoted thicknesses are mean values of six profilometer measurements on the same substrate. The uncertainties of deposition repeatability and thickness measurement were determined for a number of protocols by repeated processing and profilometer runs and comparison with x-ray reflectance (XRR) measurements. Within-substrate homogeneity was maximized by aligning the long side of the rectangular glass substrates with the rotation direction of the substrate plate (see section 6.1.1). The rotation speed around the substrate plate axis (capable of holding six 4-inch wafers) was set to a constant value of 8 rpm. Rotation around a substrate axis was not provided for.

For both radio frequency (RF) as well as direct current (DC)-powered plasmas, the generators were set to the constant power mode. The RF power (13.56 MHz) was coupled in via an automated inductive matching network. During experiments on reactive sputtering of IrOx films, the input power was held constant at 180 W (forward power for RF), the filling gas flow was set to 100 sccm. Here, in some cases, the substrate was heated to 250 °C (termed warm sputtering in the course of this work), in all other cases, the substrate was at room temperature (cold sputtering).

15

For experiments on non-reactive sputtering of Ir, the DC power, pressure and target-substrate-distance (working distance WD) each were toggled between three distinct values. The input power was set to either 180, 1000 or 2000 W, and the WD to either 45, 62 or 78 mm. The pressure was varied by means of a throttle valve. At an unaltered Ar flow of 100 sccm, it took values of $1.6 \cdot 10^{-2}$, $9.3 \cdot 10^{-2}$ and $1.7 \cdot 10^{-1}$ mbar. The pressure was monitored by means of a MKS Baratron pressure gauge (uncertainty: 0.25%).

2.2 Characterization techniques

2.2.1 Electrochemical characterization

Results that are discussed in this work and have been acquired using cyclic voltammetry (CV) and electrochemical impedance spectroscopy (EIS) all have been gathered on macro-sized electrodes with a geometrical area of 0.5 cm^2. In some of the actual or intended applications of the developed films, such as in the Epi-Ret implant, the electrodes are micro-sized [31]. Measurements regarding differences between the behavior of macro- and micro-sized electrodes have been published [78], but will not be discussed within this work, which focusses primarily on material and process development and characterization. The same argument applies to measurements using pulsed current or voltage excitations rather than DC voltage excitation as in the case of CV measurements [79].

To determine the charge delivery characteristics of IrOx films, CV was performed on a EG&G 283 Potentiostat/Galvanostat in physiological saline solution (0.9% NaCl). A standard electrochemical three-electrode cell with an Ag/AgCl reference and a Pt counter electrode was used, the scan rate was held constant at 100 mV/s.

The anodic charge delivery capacity was calculated using

$$Q_a = \frac{1}{\upsilon} \int_{E_a}^{E_c} |i| dE, \tag{2.1}$$

with E as the electrode potential vs. Ag/AgCl, i the measured current density, υ the scan rate, and E_c and E_a as the cathodic and anodic potential limits, respectively.

In order to ensure comparability, Q_a was determined using similar potential limits E_c and E_a. In the case of metallic Ir samples, the limits were -0.9 and 1.1 V. Hydrogen and oxygen evolution reactions resulting in current peaks at high negative and positive voltages, respectively, were more clearly depicted for metallic Ir samples, and it was possible to estimate and subtract

their contributions. For IrOx samples, the limits usually were -1.2 to 1.3 V. In the occurrence of H_2 and O_2 gas evolution, the limits were reduced.

In order to evoke a higher electrochemical activity (electrochemical activation), IrOx thin films were repeatedly cycled within a range excluding H_2 and O_2 evolution [80]. For activation, the potential limits were tested for each sample and set to maximum values evading gas evolution reactions.

The uncertainties of cyclic voltammetry were evaluated by repeated measurements. Accuracy and repeatability depend on the state of sample and electrolyte, i. e. substrate defects, film thickness variations and local contaminations, as well as contacting. Since electrical contact was made directly with the specimens, which are of low conductivity, the CV data can be of distorted appearance. However, this does not influence data evaluation. The total uncertainties were in the range of 5% of the measured value.

Impedance measurements were performed in the same electrochemical cell. The disturbing sinusoidal signal had an amplitude of 10 mV from the open circuit potential, and its frequency was tuned from 100 kHz to 100 mHz.

Impedance measurement uncertainties were estimated by repeated tests on the same samples. As in the case of CV measurements, the results are dependent on sample and electrolyte conditions, and on contacting. The uncertainties were determined to be in the range of 9% of the measurement value, in comparison, the measurement uncertainty of the employed impedance analyzer (Solartron 1260) can be neglected.

2.2.2 Chemical and physical characterization

Time-of-flight secondary ion mass spectroscopy (ToF-SIMS) and x-ray photoelectron spectroscopy (XPS) measurements (XPS 5600, Physical Electronics) were carried out by the Central Division of Analytical Chemistry, Forschungszentrum Jülich GmbH. The latter were performed using monochromatic Al Kα radiation. Binding energies were referenced to the C 1s electron peak due to residual hydrocarbons on the sample surface, taken at 285.0 eV. The chemical bonding states and species concentrations were deduced from O 1s and Ir 4f$_{7/2}$ peaks. The data were fitted with Gaussian/Lorentzian functions. For XPS measurements on electrochemically activated thin films, the final applied potential was -0.3 V vs. Ag/AgCl.

ToF-SIMS investigations were performed using a TOF-SIMS IV (ION-TOF GmbH, Münster) equipped with a 209Bi ion source. Depth profiles were acquired in the negative secondary ion mode using 25 kV Bi$^+$ (pulsed, bunched) primary ions for analysis (100 μm x 100 μm) and 1 kV Cs$^+$ ions for sputter etching (300 μm x 300 μm).

Crystal structures of Ir and IrOx films were investigated by X-ray diffraction (XRD) using CuKα radiation. X-ray reflectometry (XRR) was performed by the I. Physikalische Institut, RWTH Aachen, using a Philips X'pert MRD system. In order to simplify the evaluation of film density, the measurements were fitted using a software tool (WinGixa). The density was determined from the position of the total reflection edge [81, 82].

Chapter 3

Reactive RF Sputtering onto Cold Substrates

This chapter outlines a systematic approach to reactive RF sputtering of IrOx onto cold substrates, and presents the general characteristics of IrOx sputtering. Generic curves, deposition rates, chemical composition and electrochemical behavior are discussed with respect to the optimization of coatings for stimulation electrodes, and the basic mechanisms determining electrode coating suitability are explained.

3.1   Generic curves and deposition rates

In order to characterize the reactive sputtering of IrOx, generic curves were recorded at different powers, throttle values and Ar flows [5]. Fig. 3.1 shows a schematic drawing of sputter chamber and gas flows.

The change in total pressure can be described as

$$\frac{dp}{dt} = \frac{1}{V}\left(\sum_i Q_i^{in} - Q_{t,w}^{ad} + Q_{t,w}^{des} - Q_s - p(t) \cdot v_p\right), \qquad (3.1)$$

where Q_i^{in} is the gas flow to the chamber through the mass flow controller i, $Q_{t,w}^{ad}$ the gas adsorbed at target and walls, $Q_{t,w}^{des}$ the gas emitted by target and walls, and Q_s the reactive gas gettered by the condensation of sputtered material on substrate and walls. V denotes the chamber volume and v_p the system pumping speed. In the stationary case, adsorption balances desorption [83]. Hence, under the assumption of a constant system pumping speed, the sum of the gas flows into the chamber before ignition of the plasma can be expressed as

DC/RF target electrode

substrate, chamber walls
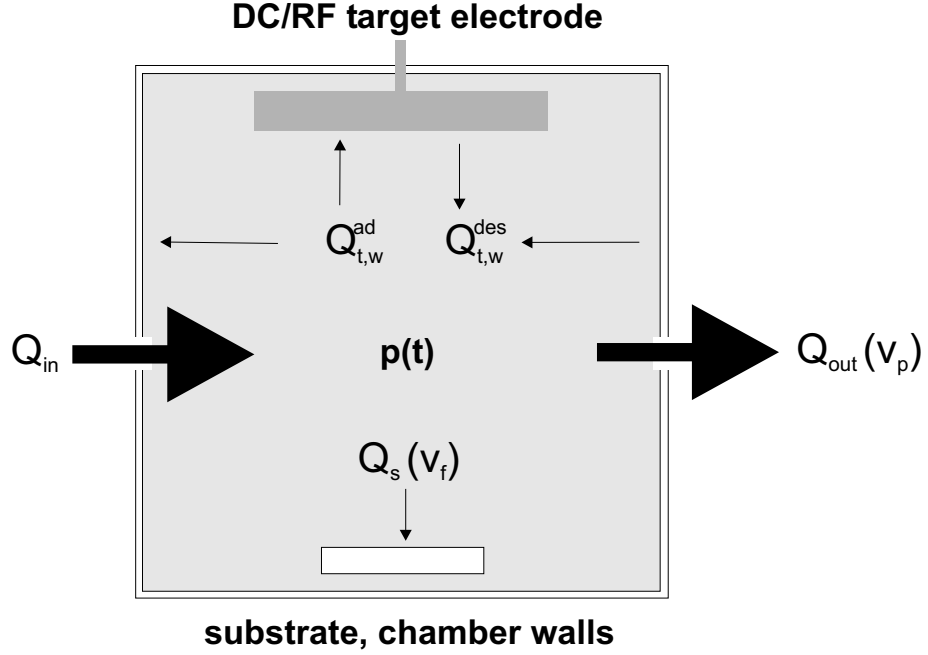
Figure 3.1: Gas flows Q and pumping speeds v in the sputter chamber. Q_{in}: Ar and O_2 supply; Q_{out}: gas flow to system pump with pumping speed v_p; $Q_{t,w}^{ad,des}$: gas components adsorbing and desorbing at target and walls; Q_s: getter flow of oxygen to the growing film with pumping speed v_f; p: pressure.

$$\sum_i Q_i^{in} = p_0 \cdot v_p, \tag{3.2}$$

and during sputtering as

$$\sum_i Q_i^{in} = p_{sp} \cdot (v_p + v_f), \tag{3.3}$$

respectively. v_f denotes the film pumping speed, meaning the rate at which the growing film getters reactive gas components. It can be deduced from the combination of equations 3.2 and 3.3:

$$v_f = \frac{v_p}{p_{sp}} \cdot (p_0 - p_{sp}). \tag{3.4}$$

v_p is calculated using equation 3.2. In the experiment, v_p, $Q(Ar)$ and the input power are held constant, whereas the oxygen gas flow (and thus the oxygen partial pressure) is increased. Using the above equations, v_f can then be calculated for all oxygen inputs.

Fig. 3.2 shows an exemplary measurement series performed at $Q(Ar) = 100$ sccm, $P = 180$ W and $v_p = 144$ l/s. It can be seen that the getter effect rises when increasing the oxygen gas supply and thus the oxygen partial pressure $p(O_2)$. At a certain point the film pumping speed reaches its maximum and declines.
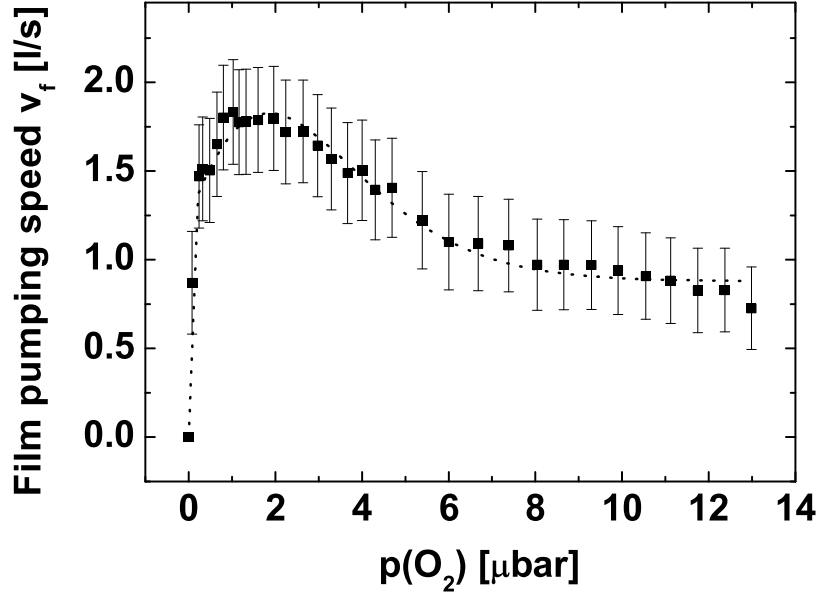
Figure 3.2: Film pumping speed for oxygen at a system pumping speed $v_p = 144$ l/s, an Ar supply of 100 sccm, and a RF forward power of 180 W. The uncertainties are determined by the pressure measurements.

A similar behavior has been reported for DC-powered deposition of IrOx films under heat supply [5]. The curve shape is best explained by the ratio of available Ir and oxygen. At low $p(O_2)$, the available oxygen is gettered by Ir atoms on the substrate, the supply of Ir particles from the target is greater than that of reactive oxygen. An increase in $p(O_2)$ balances oxygen and metal availability, until at even higher $p(O_2)$, the supply of Ir is not sufficient to consume the available oxygen. Reactive gas will start to adsorb at the target, which is known as target poisoning. The sputter yield of Ir decreases, leading to the generation of even less Ir condensation sites for oxygen consumption. The target poisoning is yet enhanced [84].

Based on the understanding of the general mechanisms, it is possible to modify the course of v_f. At a certain $Q(O_2)$, for example, an increase of v_p decreases $p(O_2)$ and expands the curve. Furthermore, the peak height and location can be changed by altering the rate at which Ir atoms are released from the target. As an example, Fig. 3.3 shows v_f over $p(O_2)$ recorded at different RF powers at otherwise unchanged conditions. A higher input power increases the release rate (deposition rate) of Ir and thus the available sites for oxygen consumption. As a result, the maximum film pumping speeds are shifted towards higher $p(O_2)$. The peak heights, i. e., the amount of oxygen gettered per time unit, increase with an increasing deposition rate of Ir. The described mechanisms were employed by Inoue et al. [3]. They produced stacked Ir/IrOx films at unchanged $p(O_2)$ by adjusting the release rate of Ir via the input power.
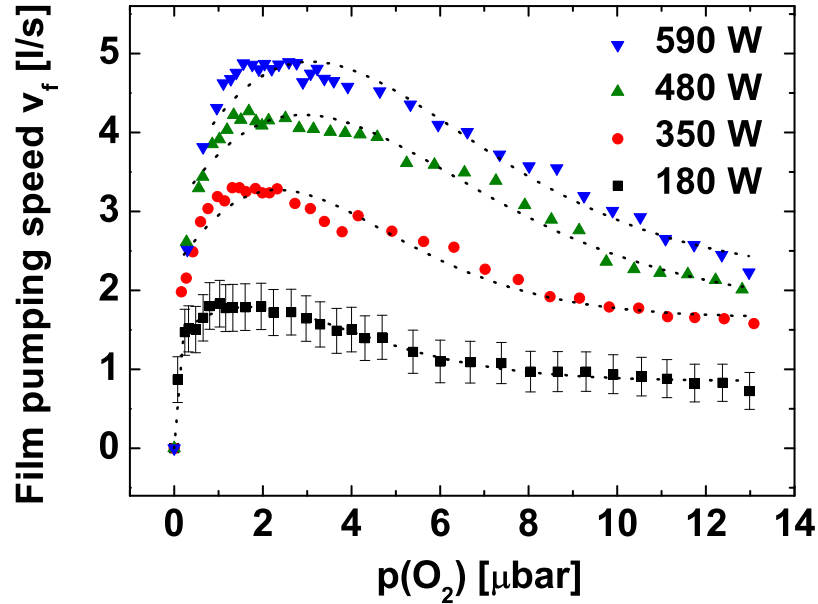
Figure 3.3: Film pumping speeds for oxygen at different RF forward powers. System pumping speed $v_p = 144$ l/s , $Q(Ar) = 100$ sccm. For the sake of clarity, error bars are shown for one data set only.

In the following, the process conditions shown in Fig. 3.2 are used as a lead for a series of depositions. As v_p was held constant, $p(O_2)$ and the

oxygen supply $Q(O_2)$ are interchangeable indicators. The latter will be the parameter drawn on in the following, since it represents a more concrete notion. It is important to note that in contrast to other publications [30], the combination of pumping speed and power was chosen such that the maximum getter effect was well resolved, and at the same time, its decline was also measurable.
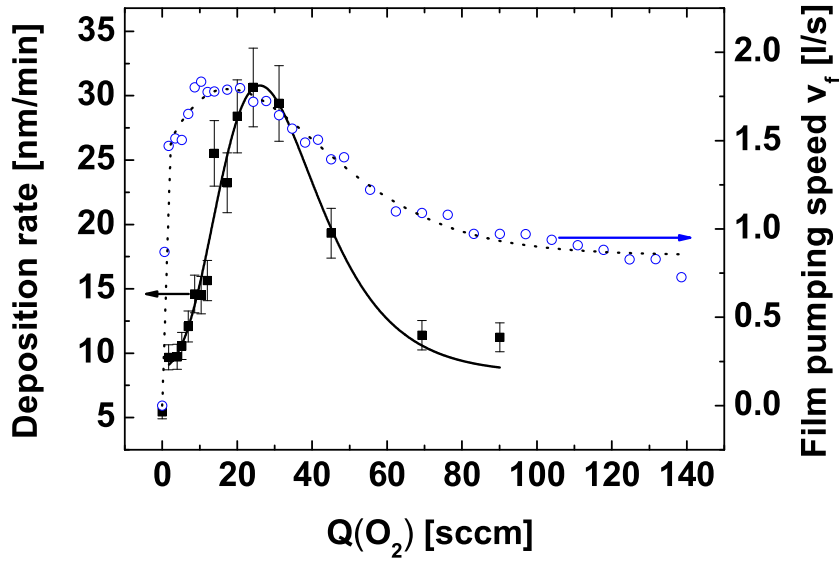
Figure 3.4: Deposition rate (square symbols) and film pumping speed as functions of oxygen flow to the sputter chamber. The uncertainties were determined by repeated processing and profilometer measurements and comparison with XRR measurements. $v_p = 144$ l/s, $Q(Ar) = 100$ sccm, $P_{RF,forward} = 180$ W.

The analysis of deposition rates can be regarded as a further approach to understanding the general behavior of the system. Fig. 3.4 shows the obtained IrOx deposition rates and v_f plotted over $Q(O_2)$.

As can be seen, the rate increases to a peak value and then declines. To start with, the incorporation of oxygen into the film leads to a volume expansion. This behavior is determined by the development of v_f over $Q(O_2)$. Accordingly, the highest deposition rate occurs at the right edge of the plateau marking $v_{f,max}$. The subsequent and concurrent decrease in deposition rate

and v_f follows from the decreased sputter yield in the poisoned target condition. Similar observations have been reported by Pinnow et al. and Horng et al. for heated DC sputtering of crystalline IrOx films [5, 61].

In Fig. 3.4, a factor of roughly 2.26 separates the deposition rate of metallic Ir from that of a film deposited at $Q(O_2) = 6.9$ sccm, at the beginning of the plateau of $v_{f,max}$. As the ratio of molar volumes $V_{IrO_2}/V_{Ir} = 2.26$, this suggests that stoichiometric IrO_2 is formed at $Q(O_2) = 6.9$ sccm [5].

It needs to be stated that in other reactively sputtered systems such as Ti-N_2, both generic curves and deposition rates are of slightly different appearance. One encounters a more pronounced drop in deposition rate as well as a sharp increase in reactive gas partial pressure in the transition zone from metallic to poisoned target [59]. Furthermore, on reversing the experiment, a hysteresis is encountered, which is not the case for Ir-O_2. The main reasons for the comparatively smooth transitions found here are the high chemical stability and low reactivity of Ir (physisorption rather than chemisorption on the target) [5].

3.2   Surface structures

Fig. 3.5 shows the surface topographies of three samples, with appearances typical for results obtained from reactive RF sputtering. At $Q(O_2) = 0$ sccm (Fig. 3.5a), the surface is characterized by small structures, the grainy appearance being characteristic for a columnar growth at low substrate temperatures (see section 6.2.1, [85]). Part b) of Fig. 3.5 shows a thin film deposited at $Q(O_2) = 6.9$ sccm, corresponding to the beginning of the plateau marking $v_{f,max}$ in Fig. 3.2. The topography now appears grainier and rougher, the structure size larger than in part a). Finally, upon further increasing the oxygen supply to $Q(O_2) = 24.2$ sccm, a different, platelet structure develops, which has been reported for DC sputtering of IrOx [1, 3]. In Fig. 3.2, this point corresponds to the end of the plateau of $v_{f,max}$. In this state, the material loses coherence and is mechanically instable, which continues to the highest oxygen inputs.[1]

The influence of oxygen on the film's morphology is twofold, and effectuates the growth of more voluminous and less densely packed coatings compared to the metal. Firstly, the unit cell of the oxidic compound IrO_2 as such is less dense than the metallic cell, by a factor of 2.26. Secondly, as Ir and reactive oxygen components react on the substrate to form oxidic compounds, the surface mobility of the arriving Ir adatom is greatly reduced [61, 86, 87].

---

[1]The mentioned mechanical instability occurs only in films of thickness greater than 100 nm.
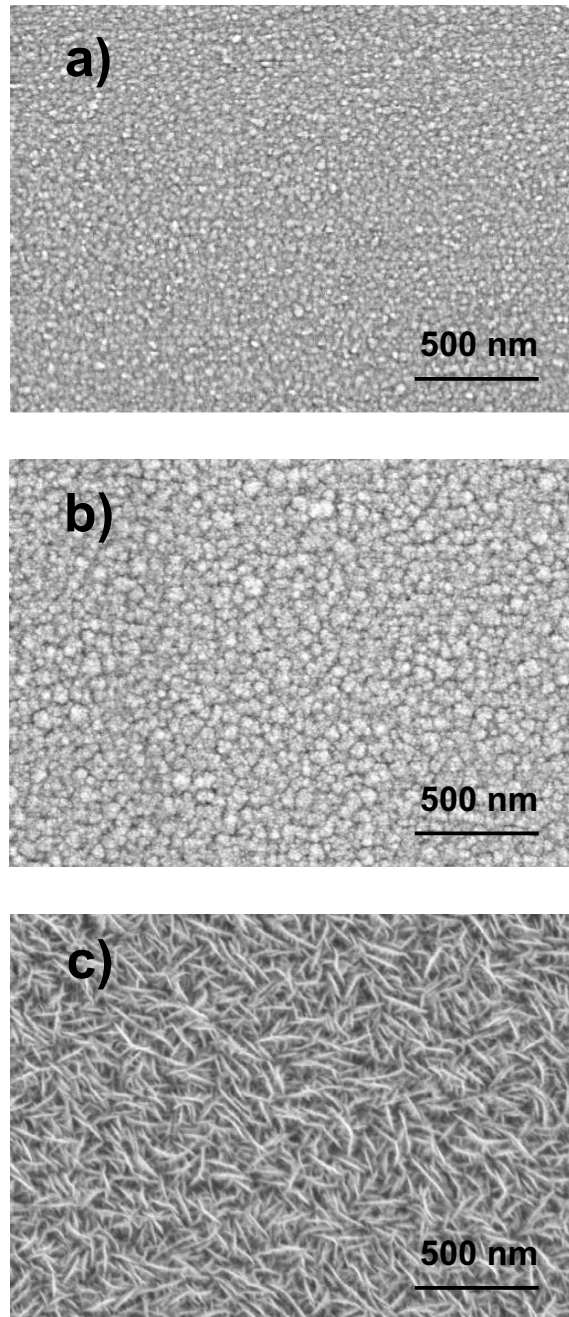
Figure 3.5: SEM surface images of samples sputtered at 180 W RF forward power and different oxygen supplies to the chamber. a) $Q(O_2) = 0$ sccm, b) $Q(O_2) = 6.9$ sccm, c) $Q(O_2) = 24.2$ sccm.

Species	E_b (Ir $4f_{7/2}$) [eV]	E_b (Ir $4f_{5/2}$) [eV]	Species	E_b (O 1s) [eV]
Ir	60.8	63.8	IrO_2	529.9
$IrO_2, Ir(OH)_{3,4}$	61.5	64.4	O_2, OH^-	531.4
Ir^{x+}, x>4	62.2	65.1	H_2O	533.0

Table 3.1: Binding energies E_b detected by XPS. Left: Ir binding energies, right: oxygen binding energies.

The ability to form a more tightly packed layer is diminished (see also sections 6.2.1 and 7.1). As a direct result, the grain size decreases to a few nm, and XRD can not detect crystallinity in the oxidic samples, as also mentioned by Kuzmin et al. [88]. Similar results were presented by Horng et al. [61] for IrOx films that were reactively DC-sputtered at elevated temperatures. With increasing oxygen content in the sputter chamber, film crystallinity decreased due to lower Ir surface mobility. The effect was amplified by the oxidation of the used Si substrates. Also for Ni oxides, equivalent results were published [87]. With an increasing $p(O_2)$, the grain sizes decreased.

3.3   Chemical composition of RF-sputtered films

XPS analysis is applied to compare film composition and bonding states of metallic to oxidic, and stable to powder-like films. Table 3.1 gives an overview of the species present in the samples, the detected binding energies were referenced to earlier publications [11,21,26,27,50,61,89,90]. As examples of XPS spectra, Fig. 3.6 shows Ir 4f peaks of two samples deposited at 0 (a) and 6.9 (b) sccm oxygen flow. The fits of contributions are included.

The chemical compositions of these and further RF-sputtered IrOx films are summarized in Table 3.2. Deposition at zero oxygen feed-in delivers a metallic sample. Small amounts of an oxygen-containing Ir species are detected, resulting from residual gas in the sputter chamber, as well as water and hydroxyl groups, adsorbed during storage. Already starting at a low oxygen input of 1.7 sccm, the Ir 4f peak shifts to higher binding energies, and, different from earlier reports regarding DC-sputtered IrOx [30], pure metal is no longer detected.

On all samples shown in Table 3.2, high concentrations of hydroxyl groups or excess oxygen are detected, as well as a high degree of adsorbed water or hydration. The oxidic samples contain Ir atoms of two different valences, the first one either in tetravalent form (IrO_2 or $Ir(OH)_4$), or in trivalent $Ir(OH)_3$. The analysis technique employed does not permit unambiguous distinction between the mentioned groups, which was also found by Jung et al [91]. In
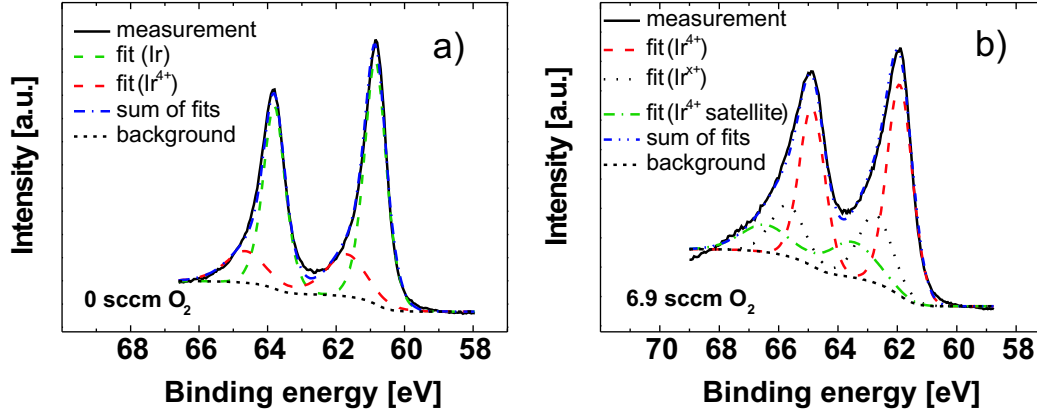
Figure 3.6: Exemplary XPS measurements and fits (Ir 4f) of RF-sputtered samples deposited at $Q(O_2) = 0$ (a) and 6.9 sccm (b). The binding energies used for fitting are listed in Table 3.1. Included are contributions of Ir^{4+} satellite peaks at $E_b(Ir^{4+}) + 1.3$ eV.

most instances, though not in all, $Ir(IrO_2)/O(IrO_2) = 0.5$, consistent with the lattice oxide stoichiometry. XPS is not able to clarify whether stoichiometric IrO_2 is formed preferably at $Q(O_2) = 6.9$ sccm, as the deposition rate analysis had suggested.

The second Ir valence Ir^{x+}, where x>4, can not unambiguously be affiliated with a certain chemical compound, as XPS analysis does not allow to distinguish between OH and $Ir(OH)_x$ in the O 1s region. The species has been shown to exist in IrOx formed by other methods, but not by reactive sputtering [27, 50, 56, 90, 92, 93]. It is not as commonly reported on as

$Q(O_2)$ [sccm]	Ir	IrO_2, $Ir(OH)_{3,4}$	Ir^{x+}, x > 4	O (IrO_2)	O (OH^-, O_2)	O (H_2O)	Ir^{4+}/Ir^{x+}
0	20.8	9.4	0	4	40.2	25.5	-
1.7	0	16.1	6.6	18.4	50.6	8.6	2.5
6.9	0	8.4	7.5	18.1	46.3	19.8	1.1
10.4	0	9.7	8.3	18.5	48.9	14.7	1.2
24.3	0	7.5	9.1	14.8	53.6	15	0.8
90.1	0	7.1	8.3	14.2	56	14.4	0.9
6.9*	28.9	25.7	0	20.1	14.7	10.7	-

Table 3.2: Composition [at. %] of RF-sputtered IrOx films deposited at different $Q(O_2)$. *: after two minutes Ar backsputtering.

$Ir^{3+,4+}$, which are well-known especially with regards to reduction/oxidation in electrolyte. The available literature does not unambiguously declare the instability of Ir^{x+}, x>4. Its formation might be a result of surface oxidation in air [50]. Nevertheless, on grounds of the available data, the main difference between the oxidic samples is the ratio of Ir^{4+}/Ir^{x+}.

Compounds containing Ir^{x+} are present in all oxidic samples, also in stable films (see Table 3.2). For $Q(O_2) = 6.9$ sccm, from Table 3.2, $Ir^{4+}/Ir^{x+} = 1.1$, meaning that the common compound IrO_2 prevails upon deposition in the metallic target mode. On the contrary, at the far side of the plateau of $v_{f,max}$ in Fig. 3.2 ($Q(O_2) = 24.2$ sccm), $Ir^{4+}/Ir^{x+} = 0.8$. Without being able to clarify the exact reason, the formation of powder-like films and the predominance of Ir^{x+} correlate with the deposition in the poisoned target mode.

The above discussed XPS data were acquired without a prior sputter etching of the samples. The last row of Table 3.2 contains exemplary XPS data of a sample after two minutes Ar sputter etching. All oxidic samples can be reduced to metallic films, which is known as preferential sputtering [26]. Ir^{x+} is first reduced to Ir^{3+} or Ir^{4+}. The early reduction supports the mentioned claims regarding Ir^{x+} being a product of surface oxidation [50]. Subsequently, reduction to Ir with excess molecular O_2 or attached hydroxyl groups takes place [61]. H_2O and O_2 or OH concentrations drop upon sputter etching, but still are detectable, meaning the signals are not solely associated with surface phenomena, but with species in the film volume.

A final conclusion regarding the origin of Ir^{x+} can not be drawn. In order to be able to clarify its nature, further investigations have to exclude surface oxidation after deposition, which can be achieved by in-situ methods.

3.4 Electrochemical properties of RF-sputtered films

Fig. 3.7 shows cyclovoltammetric data of three films deposited at $Q(O_2) = 0$, 6.9 and 24.2 sccm after activation with 50 cycles, surface structures of which had been shown in Fig. 3.5. An oxygen flow of 24.2 sccm is associated with $v_{f,max}$ and accordingly the highest deposition rate (see figure 3.4). $Q(O_2) = 6.9$ sccm stands for deposition at the beginning of the plateau of $v_{f,max}$.

All three curves comprise several current peaks. Charge exchange reactions in Ir, activated Ir and IrOx have been discussed by several authors, a number of different models and reaction paths were proposed [16, 30, 36, 47, 80, 93, 94]. The current peaks are caused by reversible redox reactions as well as by electrolysis at high positive and negative potentials. Peak locations
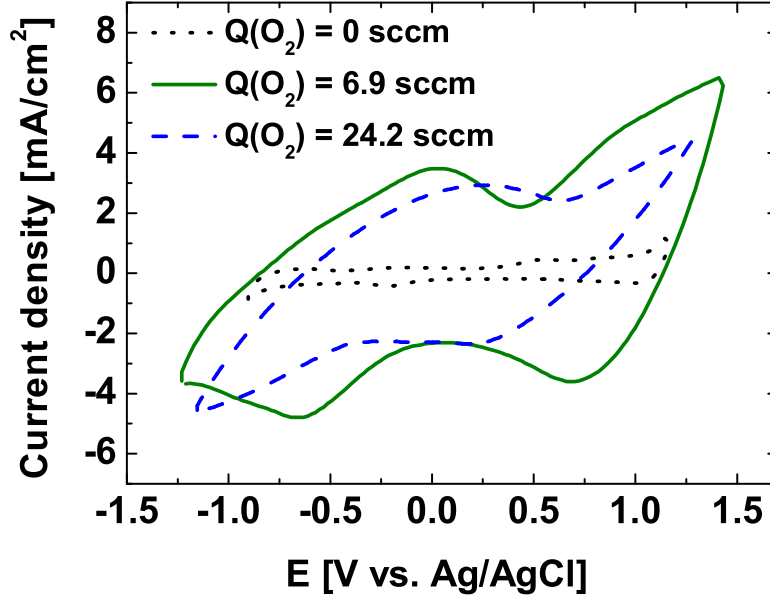
Figure 3.7: CV data of Ir(Ox) thin films deposited at different oxygen flows $Q(O_2)$. The films were activated with 50 cycles. See Fig. 3.5 for surface images of the as-deposited films.

and peak forms of the films under study are comparable, which indicates equivalent redox reactions, however, the film responses differ strongly in the current magnitude.[2]

Fig. 3.8a) shows the anodic charge delivery capacity Q_a evaluated from CV measurements on deposited films and the film pumping speed v_f as functions of oxygen supply during sputtering. Part b) of the same figure shows the double layer capacitance C_{dl} as extracted from Bode plots. Assuming a Randles cell as an equivalent circuit model, the electrode impedance is dominated by the double layer capacitance at lower frequencies. Under these premises, the capacitance C can be calculated from $|Z| = (\omega C)^{-1}$ at a frequency $\omega = 1s^{-1}$.

---

[2]The exact peak locations and forms in the CV diagram are determined by the existence of redox sites at different formal potentials [30]. However, it is not the focus of this work to investigate the detailed mechanisms of charge transfer.

The courses of double layer capacitance and charge delivery against $Q(O_2)$ and v_f are congruent. C_{dl} depends on the electroactive area available for charge transfer, and an increase in area will effectuate an increasing Q_a.

As both graphs illustrate, the electrochemical properties are strongly dependent on $Q(O_2)$ and thus v_f. At low $Q(O_2)$, C_{dl} and Q_a increase in value, just as steeply as does v_f. Note that $Q_{a,max} = 80$ mC/cm^2 and $C_{dl,max} = 6.5$ mF occur at the beginning of the plateau of $v_{f,max}$, at $Q(O_2) = 6.9$ sccm (Fig. 3.5 b). As the analysis of deposition rate had suggested, stoichiometric IrO$_2$ is formed at this point.

Hence, up to a point determining the onset of $v_{f,max}$, electrochemical activity increases with increasing getter flow to the layer. Still on the plateau of $v_{f,max}$, but at higher oxygen flows, the activity drops. This is accompanied by a transition from grainy to platelet topography, and by a loss of mechanical stability of the thin films upon target poisoning.

From the SEM images of Fig. 3.5, changes in surface topography and porosity are the main causes for increasing and decreasing electrochemical activity. Although the peak potentials shown in the CV curves of Fig. 3.7 are influenced by the oxygen supply to the sputter chamber, general changes in redox behavior do not occur.

This is corroborated by the chemical composition analysis. Compared to the deposition of metallic Ir, a reactively sputtered film is more easily permeable for water and ionic species, leading to a higher charge delivery. The different current magnitudes shown in the CV data are related to a difference in number of accessible reaction sites.

The interplay between oxygen and Ir availability on the substrate takes the decisive role for the formation of the most useful morphology (see section 3.2). At too low oxygen supplies, the layer is too densely packed. At a too high oxygen supply, a state in which also the target is poisoned, free surface energy is minimized by the formation of less electroactive platelets. At a balanced oxygen supply, corresponding to a target state shortly before poisoning, the arriving Ir adatom and oxygen particle quickly react on the substrate. The average diffusion length of an Ir adatom before reaction is low, resulting in a high defect density. This, in turn, is directly measurable as pores and available surface for redox reactions (see section 6.2.1).

Similar results were reported with respect to reactively sputtered Ni oxides [87]. With an increasing $p(O_2)$, crystalline order and grain sizes decreased. Consequently, the measured interfacial capacitance increased due to an increase in active surface area.
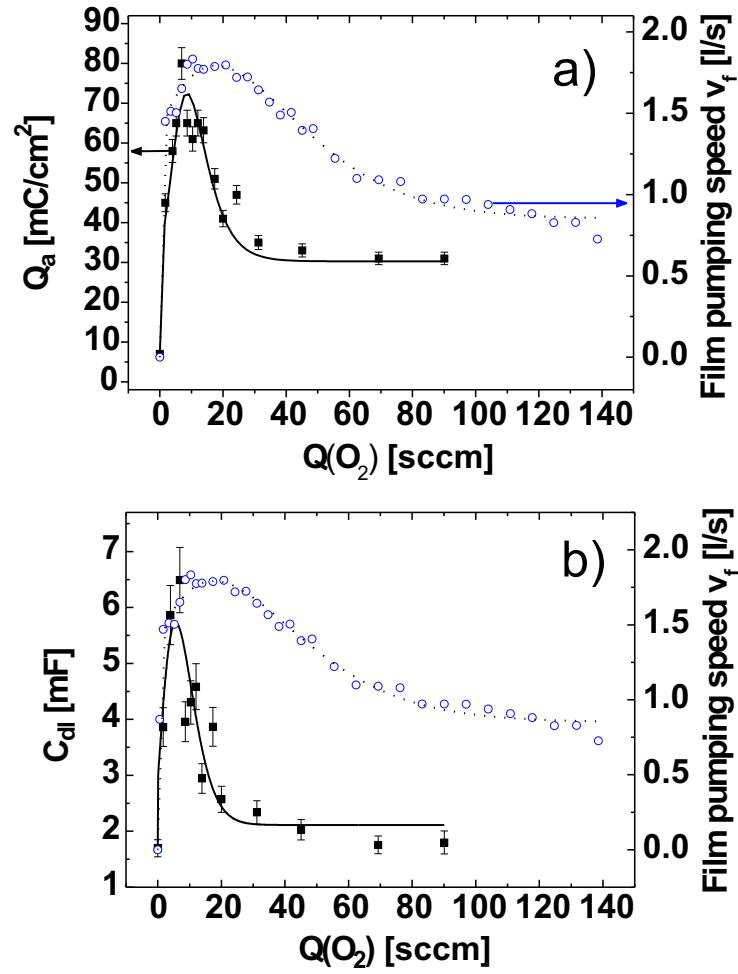
Figure 3.8: a) Anodic charge delivery capacity Q_a and film pumping speed v_f over oxygen supply $Q(O_2)$. b) Double layer capacitance C_{dl} and film pumping speed v_f over $Q(O_2)$. C_{dl} and Q_a evaluated after 100-fold activation cycling of the thin film. Uncertainties were determined by repeated measurements.

3.5   Summary

This chapter presented an approach to understanding the general behavior of the RF-sputtered IrOx system with respect to application as stimulation electrode coating.

The oxygen flow to the growing film was determined by an analytical approach. It was shown that deposition rate, surface structure and chemical composition are unambiguously tied to the development of v_f over $Q(O_2)$. In turn, these properties determined the electrochemical characteristics of thin IrOx films.

The peak values $v_{f,max}$ were levelled on a plateau, along which target poisoning occurred. At the beginning of the plateau, the electrochemically most active films were deposited, with a roughened surface structure. Still on the plateau, but at higher oxygen flows, mechanically instable thin films with a platelet surface structure and with limited electrochemical activity were deposited. At this point, the maximum deposition rate was reached.

Electrochemical activity was linked to available active sites and thus topography, as chemical composition and electrochemical data did not suggest general changes in redox behavior.

The relationship between deposition characteristics, chemistry and morphology is further investigated in the next chapter. Based on the general findings presented here, the focus is expanded to clarify the influences of plasma excitation (DC vs. RF sputtering), substrate temperature, and electrochemical activation.

Chapter 4

Plasma Excitation, Substrate Temperature, and Activation

Based on the findings described in the previous chapter, this chapter reports on the comparison of RF and DC sputtering of IrOx onto cold and heated substrates. XPS and ToF-SIMS, SEM and electrochemical techniques are employed to examine the influence that chemical composition, film morphology and activation of IrOx have on stimulation characteristics. It is clarified in how far plasma excitation and temperature alter oxygen integration into a growing film, and whether the range of deposition of stable films can be expanded. In terms of application, the chapter discusses the process conditions delivering the electrochemically most active coatings.

4.1   Comparison of deposition characteristics

As had been shown in the preceding chapter, the analysis of generic curves is the key to understanding most effects regarding the deposition and characteristics of IrOx films. In this respect, this chapter is opened with a brief section about similarities and differences between generic curves obtained by RF sputtering onto cold and heated substrates as well as cold DC sputtering.

Fig. 4.1 shows the oxygen flow to the growing films versus oxygen supply to the chamber. All curves were recorded at 180 W (forward power for RF) and a system pumping speed of 144 l/s. For all process conditions, the general curve shape is the same, and follows the pattern described in chapter 3.

Compared to DC-powered sputter deposition, RF sputtering yields a lower maximum oxygen integration rate, which also sets in at a slightly earlier stage. This effect is due to the combination of two factors: Firstly, RF deposition rates typically are lower, generating a lower flux of Ir reaction partners
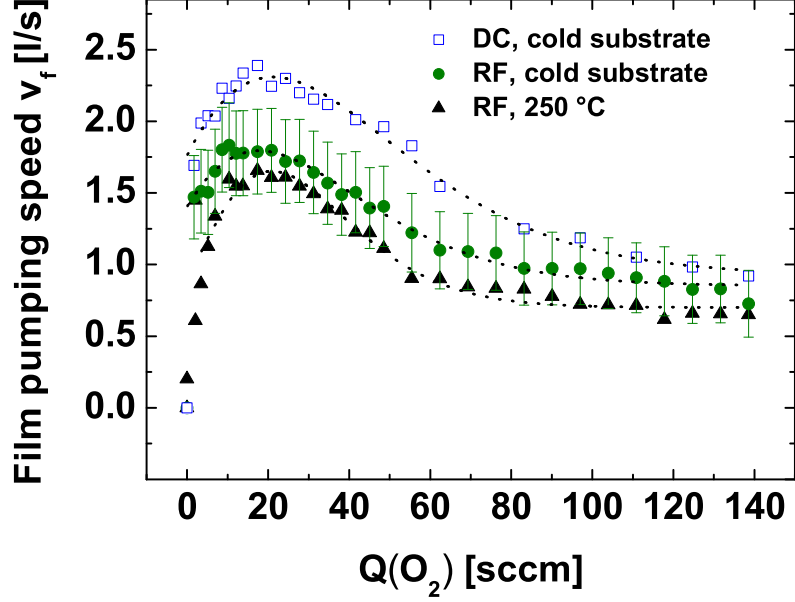
Figure 4.1: Rate of oxygen integration (film pumping speed v_f) into the growing film for RF and DC cold sputtering as well as RF warm sputtering, as a function of oxygen supply to the sputtering chamber $Q(O_2)$. All curves were recorded at 180 W (forward power for RF) and a system pumping speed of 144 l/s. For clarity, error bars are only shown for one data set.

(see below, [66, 67, 69, 71]). Secondly, the RF plasma is known to be denser than its DC counterpart [63, 72], which leads to a higher rate of oxygen dissociation [69]. Higher numbers of reactive O species and lower numbers of available Ir reaction partners lead to the observed earlier peak. A similar observation has been made by Martin and Rousselot for Ti-O and Cr-O [66]. Irrespective of measurement uncertainty, a heated substrate yields a slightly lower maximum integration rate, also with an earlier inset. Enhanced reactivity of Ir atoms on the heated substrate can serve as a tentative explanation. Furthermore, diffusion lengths of Ir species on the substrate are increased, i. e., the radius within which an oxide compound can be formed. This way, the probability of a reaction is enhanced.

Fig. 4.2 shows plan-view SEM images of samples deposited at the respective highest rate of oxygen integration of all three process conditions.

The films were sputtered at $Q(O_2) = 6.9$ sccm for both RF types and $Q(O_2) = 10.4$ sccm for DC. Fig. 4.2a) shows a sample deposited under RF excitation and onto a cold substrate. The surface is characterized by a grainy appearance and hillocks. The warm sputtered sample of Fig. 4.2b) appears comparably smooth and unvoided. As additional energy supply by heat enhances surface diffusion, adatoms can reorganize and form more tightly packed layers. Substantiating the observations, partial crystallinity detected by XRD develops only in these samples (data not shown). DC-sputtered samples (Fig. 4.2c) have the most open appearance. Voids are clearly visible on the surface between the growth columns, and cauliflower-type structures possessing self-similarity at higher resolutions can be seen only here.

The smoother features developed during RF sputtering can be explained by the plasma characteristics. As is known, magnetron confinement is less pronounced in RF plasmas [68], meaning that the discharge expands further from the target. As a result, the energetic flux of plasma species to the growing film is more expressed [64, 65, 68]. The additional energy input, similar to the case of heated sputtering, leads to enhanced surface remodelling by adatom diffusion.

For all sets of process conditions, the dependence of deposition rate on $Q(O_2)$ is as has been described for cold RF sputtering (see section 3.1). Metallic Ir is grown at rates of 4.2 (RF, warm), 5.4 (RF, cold) and 6.7 nm/s (DC, cold). These differences are due to a higher packing density as a result of heating and also express the typically lower deposition rates in RF sputtering.

The similarity of deposition characteristics between all process conditions extends to the formation of powder-like films. Exactly as had been detailed in the preceding chapter for cold RF sputtering, instable films are formed by cold DC and warm RF sputtering at sufficiently high $Q(O_2)$, starting along the plateau of $v_{f,max}$.

4.2   Chemical composition

Table 4.1 shows compositions of films processed under heat supply, with all remaining parameters unaltered with respect to cold sputtering. Referencing the entries to compositions of cold RF-sputtered films (Table 3.2 on page 27), warm sputtered IrOx contains all compounds found in the cold counterparts, and also in comparable concentrations.

The DC films analyzed by XPS are chosen referencing the location of points on the DC and RF oxygen integration curves of Fig. 4.1. At an oxygen supply of $Q(O_2) = 10.4$ sccm to the DC sputter process, the oxygen
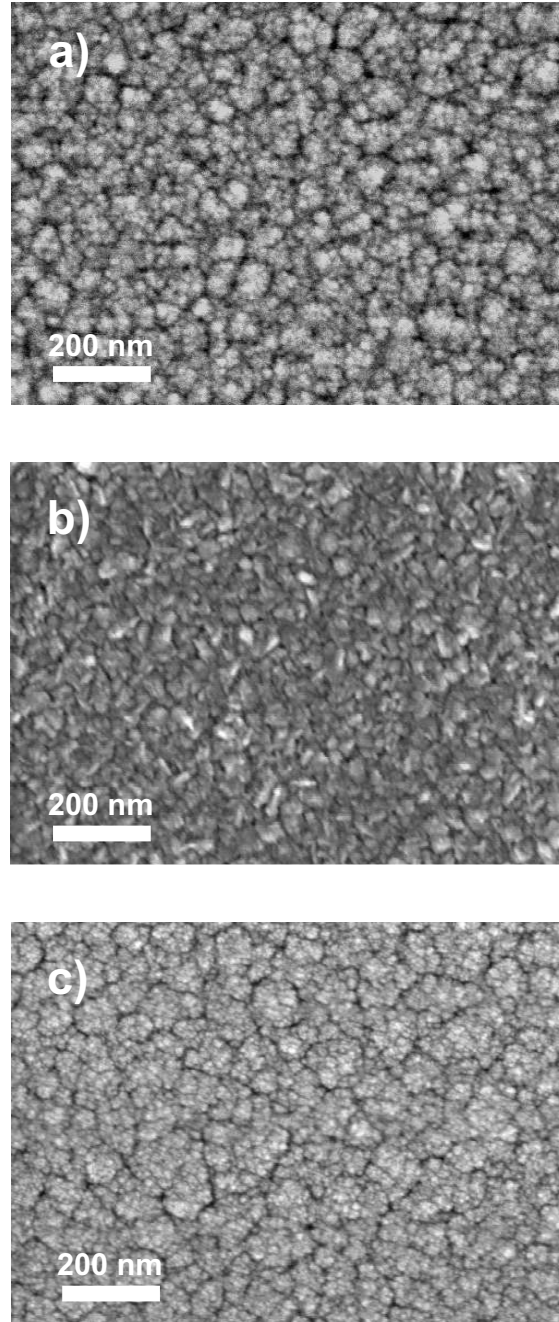
Figure 4.2: Surfaces of samples deposited by a) RF sputtering onto a cold substrate, b) heated RF sputtering and c) DC sputtering onto a cold substrate. Input power $P = 180$ W (forward power for RF). $Q(O_2)$=6.9 sccm for both RF samples, $Q(O_2)$=10.4 sccm for DC, corresponding to the respective highest rates of oxygen integration.

$Q(O_2)$ [sccm]	Ir	IrO_2, $Ir(OH)_{3,4}$	Ir^{x+}, x > 4	O (IrO_2)	O (OH^-, O_2)	O (H_2O)	Ir^{4+}/Ir^{x+}
6.9	0	10	8.8	17.7	51.3	12.2	1.1
24.3	0	8.9	10	15.6	53.9	11.6	0.9

Table 4.1: Composition [at. %] deduced from XPS measurements of warm RF-sputtered IrOx films deposited at different $Q(O_2)$. The compositions can be compared to those of films sputtered under equivalent conditions onto a cold substrate (Table 3.2 on page 27).

$Q(O_2)$ [sccm]	Ir	IrO_2, $Ir(OH)_{3,4}$	Ir^{x+}, x > 4	O (IrO_2)	O (OH^-, O_2)	O (H_2O)	Ir^{4+}/Ir^{x+}
10.4	0	13.5	9	20.8	46	11.1	1.5
45	0	8.8	9.5	17.6	54.9	9.2	0.9

Table 4.2: Composition [at. %] of cold DC-sputtered IrOx films deposited at different $Q(O_2)$. As to locations of points on the DC and RF oxygen integration curves of Fig. 4.1, $Q(O_2) = 10.4$ (45) sccm in the DC process corresponds to $Q(O_2) = 6.9$ (24.3) sccm for RF. The compositions can thus be compared to those of Table 4.1 and Table 3.2 on page 27.

integration rate into the film is just reaching its maximum level. This corresponds to $Q(O_2) = 6.9$ sccm for RF. At $Q(O_2)=45$ sccm for DC, the far side of the plateau has been reached (24.3 sccm for RF).

DC films contain all compounds found in RF-sputtered samples, as extracted into Table 4.2. The former show a higher concentration of Ir in oxidic or hydroxide form, the ratio Ir^{4+}/Ir^{x+} is increased. Also, the water concentration decreases, however, as a whole, the measured compositions do not undergo significant changes when varying the plasma excitation.

4.3   Electrochemical characterization

Fig. 4.3 comprises CV data of three samples sputtered at the respective highest rate of oxygen integration into the film for each deposition type (RF cold and warm at $Q(O_2) = 6.9$ sccm, DC cold at $Q(O_2) =10.4$ sccm), surfaces of which are shown in Fig. 4.2. As had been discussed in the preceding chapter, the films produced under maximum oxygen integration are electrochemically most active. The following sections focus on samples deposited under these conditions. The data shown in Fig. 4.3 were extracted without prior repeated potential cycling, meaning the surfaces are nearly as-deposited.
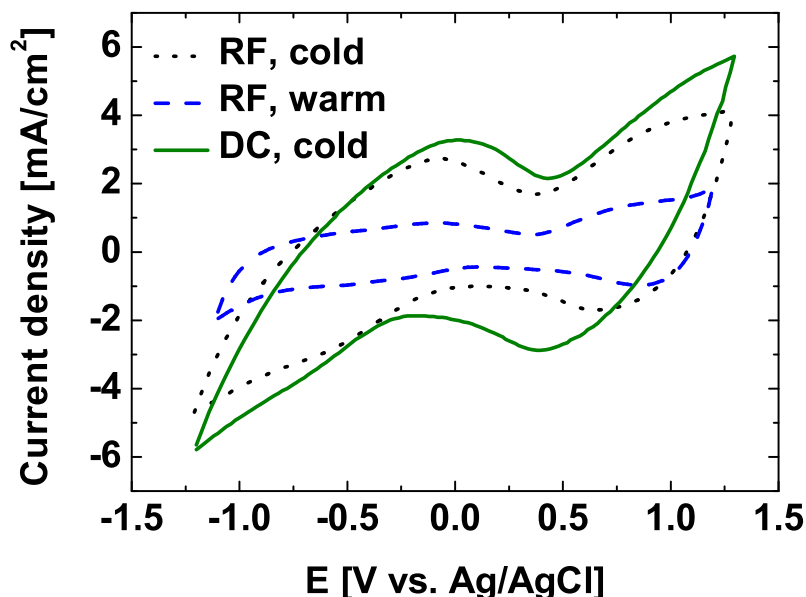
Figure 4.3: CV of as-deposited (non-activated) samples sputtered at the respective highest rate of oxygen integration for RF (cold/warm) and DC (cold) sputtering (see Fig. 4.2 for surface images).

Equivalent redox reactions are indicated by similar peak locations and forms. This is in line with XPS analysis which had shown that plasma conditions and substrate temperature independently yield chemically comparable films if deposited under equivalent oxygen flows. Nevertheless, the film responses differ in the magnitude of redox currents, which indicates a difference in number of accessible reaction sites on or within the film.

Cold- and DC-sputtered samples have the highest response to voltage excitation, whereas the films sputtered under heat supply are least active. The decreased electrochemical activity of warm-sputtered samples can be explained by tighter packing and fewer available reactive sites (see section 4.1). Ion insertion into the film and to reaction sites is limited. The denser film morphology is caused by the additional input of thermal energy to the substrate. In turn, a higher mobility of sputtered adatoms on the substrate is generated, allowing the reorganization of films towards lower defect densities. Similar observations have been made regarding the electrochromic properties

of IrOx which, after annealing and formation of a partially crystalline structure, showed a decreased ionic conductivity [14]. The slight differences in film composition seen in XPS can be assumed to play a minor role.

DC-sputtered samples show a slightly higher electrochemical activity than their cold RF-sputtered counterparts. This can be attributed to the rougher and more porous film structure. At this point, it remains to be answered whether the rougher surface deposited under DC plasmas is solely due to a smaller energy flux to the substrate (see discussion in section 4.1), or whether it also is influenced by the slightly altered concentrations of Ir oxides, hydroxides and water.

4.4 Morphology and chemistry of activated IrOx

SEM analysis, XPS measurements and SIMS depth profiling on activated samples were carried out in order to determine in how far activation leads to changes in chemical composition and morphology. A further relevant question is whether any of the investigated sputter parameters generate as-deposited thin films that are similar to activated ones, which would render the procedure of activation before application unnecessary.

Activation is generally understood as repeated potential cycling to higher electrochemical activity or charge delivery. The phenomenon has been investigated in detail with respect to metallic Ir. For these electrodes, it is widely accepted that upon potential cycling, ionic species advance into the Ir matrix and a hydrated oxy-hydroxide of non-compact nature is formed [16, 18, 30, 47, 93]. The evolving structure can be regarded as weakly cross-linked, the matrix being permeated with water and ionic species [47]. Not only metallic films, which grow anodic oxide layers, but also non-metallic films such as the ones described here can be activated. Contrary to research performed on metallic Ir, XPS investigations regarding the activation of non-metallic IrOx thin films are not available.

However, due to lack of data regarding the presence of surface intermediates, it will not be hypothesized on certain reaction paths. Instead, this section focuses on the influence that changes in chemical composition can have on morphology as well as electrochemical (macroscopically measurable) characteristics of a stimulation electrode coating. As an example for activation, Fig. 4.4 shows CV and impedance data of a cold RF-sputtered film prior to and after 100 potential cycles. The anodic charge delivery increases

from 48.5 to 80 mC/cm^2, the cut-off frequency drops by more than an order of magnitude.
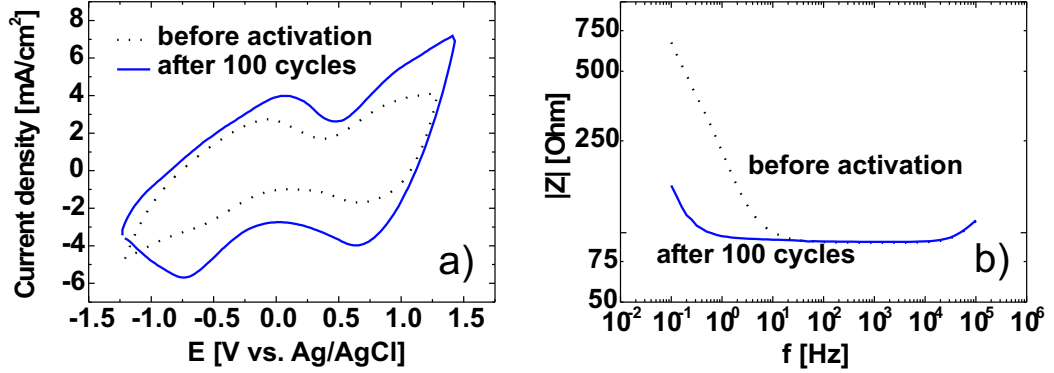
Figure 4.4: CV and impedance data of a cold RF-deposited sample ($Q(O_2) = $ 6.9 sccm) prior to and after activation (see also Fig. 4.2a).

Fig. 4.5 includes two fracture cross sections of the same IrOx sample, the top part showing the film in the as-deposited state, the bottom one the activated film. 2000-fold potential cycling not only alters the surface appearance, but also largely overrides the initial columnar growth morphology still seen in Fig. 4.5a). As an effect, the structural anisotropy developed during film growth is alleviated. ToF-SIMS and XPS were employed to describe these changes on a chemical scale.

Fig. 4.6 shows a fracture cross section and the corresponding ToF-SIMS depth profile of a partially activated sample deposited at $Q(O_2) = 6.9$ sccm (RF, cold substrate, 300 nm IrOx plus 50 nm Ti adhesion layer). In this case, the potential was cycled only for 150 times, leaving the lower part of the sample inactivated. During depth profiling the sample is eroded by primary ions, therefore measurement time corresponds to sampling depth. Sputtering was carried out until Ti adhesion layer and SiO$_2$ substrate were reached. The vertical dashed lines indicate the observed layered structure of the sample, consisting of activated IrOx, as-deposited IrOx, Ti and SiO$_2$. After about 250 s, the intensity of an Ir and OH containing compound (let Ir(OH)$_3$ serve as an example) decreases by a factor of roughly 30, whereas an Ir oxide compound (Ir$_2$O$_2$) as well as molecular O$_2$ are more or less constant. This indicates the border between activated and underlying non-activated part and therefore a transformation of structure and properties when crossing it. Other Ir oxide components mentioned in the course of preceding and
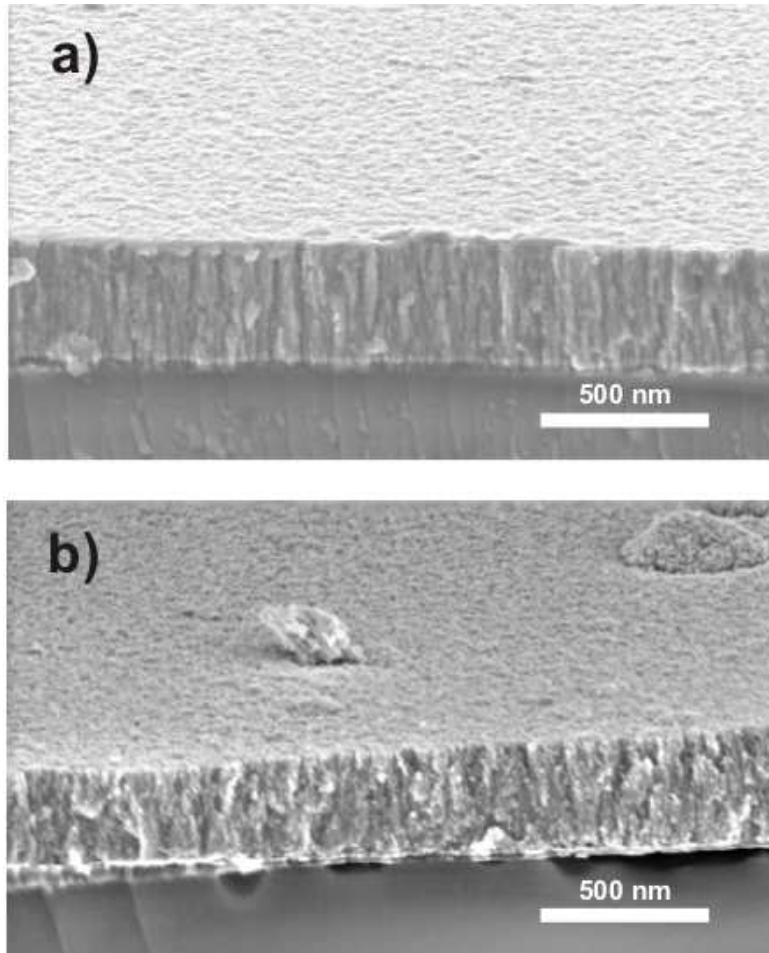
Figure 4.5: Sectional views of an IrOx thin film (DC, cold sputtering, $Q(O_2) = 10.4$ sccm) before (a) and after activation (b). The defect in the foreground of the activated surface is a residue from sample sectioning, the nodule in the background is the result of growth on substrate defects (see section 7.2).

following XPS discussions were not used for analysis due to saturation of counts.

As had been shown by Kötz et al. for anodic iridium oxide films, oxidation states detected by XPS depend on the final potential applied to the film before it is lifted from the electrolyte [27]. The application of different positive potentials (0.0 V, 0.9 V and 1.25 V vs. a saturated calomel electrode) resulted in an increasing shift of the O 1s signal to lower energies, accompanied by a broadening of the structure. The Ir 4f peaks, on the other hand, remained unaffected. Also in the present case, the final electrode potential being negative at -0.3 V vs. Ag/AgCl, the Ir 4f energies and structure persist. On the contrary, significant changes can be seen in the O 1s signals of Fig. 4.7, showing measurements on a sample (cold, RF, $Q(O_2) = 6.9$ sccm) before and after activation. Compared to the broad peak in the as-deposited state, which contains the three O compounds mentioned before, the signal has narrowed as a result of activation. It is now centered at 531.4 eV, the binding energy of OH^- and O_2.

The chemical compositions evaluated from XPS measurements of two films (cold substrate, RF plasma, different oxygen partial pressures during deposition) before and after repeated potential cycling are found in Table 4.3. As the samples were left to dry prior to XPS analysis, the water concentration does not increase upon activation. Activated samples have the highest concentration of hydroxyl groups or O_2 and the lowest concentrations of O in IrO_2 of all investigated samples. For increasing positive electrode potentials, as shown by the measurements of Kötz et al., the ratio of hydroxyls to oxides can be expected to decrease again.

In the samples discussed here, the concentrations of lattice oxide are in line with IrO_2 stoichiometry before activation, but strongly deviate in the activated state. Along with the high OH^- concentration, this proposes that Ir hydroxides such as $Ir(OH)_3$ or $Ir(OH)_4$ have been formed. The data in row three of Table 4.3 show that only about 1.65% (3.3%/2) of all detected species are Ir^{4+} bound in IrO_2. The remaining 4.55% (6.2%-1.65%) (Ir species in column 2) are part of $Ir(OH)_{3,4}$. This is in accordance with the above discussed SIMS depth profiling.

Furthermore, the data also confirms earlier postulations by Zerbino et al. [80] and Augustynski et al. [50], albeit proposed with respect to the activation of pure Ir metal to IrOx in dilute sulphuric acid. In aqueous solutions, IrO_2 can take the form of $Ir(OH)_4$, equivalent to $IrO_2 \cdot H_2O$. The formation of such a compound implies that the binding forces left on Ir species in relation to the metal-oxide lattice are practically cancelled out, leaving a film of hydrated oxy-hydroxides, easily permeable for ions from solution. This change in film nature even becomes visible (see Fig. 4.5). Thus, through
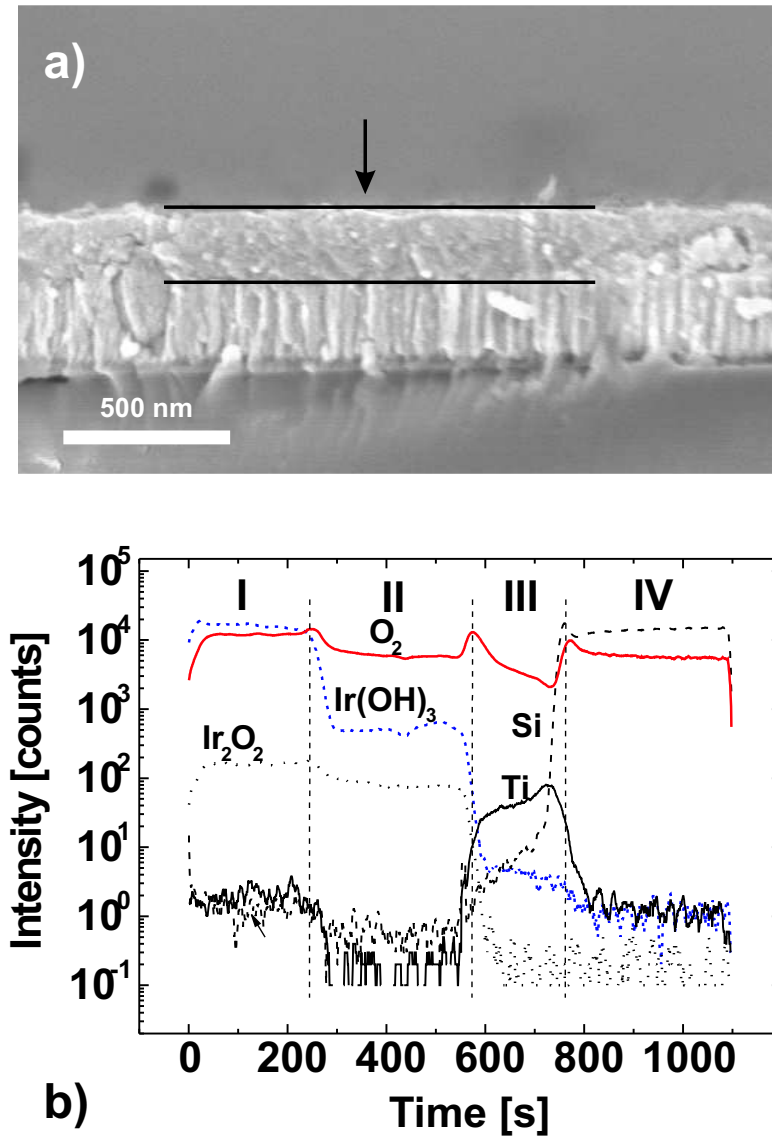
Figure 4.6: a) SEM cross section of a sample (RF, cold sputtering, $Q(O_2) =$ 6.9 sccm) fractured after partial activation. The electrolyte penetrates from the top as indicated by the arrow. The activated part is framed. b) ToF-SIMS depth profile of the same sample. The profile consists of four layers: I: activated IrOx, II: as-deposited IrOx, III: Ti adhesion layer, IV: SiO_2 substrate.
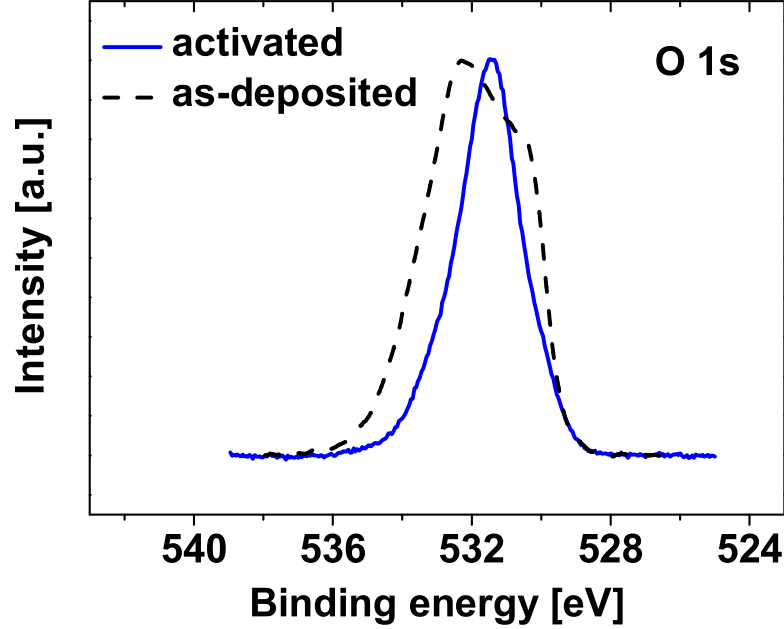
Figure 4.7: XPS O 1s peak of a cold RF-sputtered ($Q(O_2) = 6.9$ sccm) thin film before and after activation.

changes on the chemical scale, the film structure is largely altered, which is manifested in a higher electroactivity, caused by easier ion insertion.

As Table 4.3 also shows, $Ir^{4+}/Ir^{x+} < 1$ after activation. In the preceding chapter, a ratio of $Ir^{4+}/Ir^{x+} < 1$ was found solely in as-deposited samples of platelet morphology and mechanically instable, powder-like form. These films are the product of deposition with high oxygen feed to the sputter chamber (see Ir^{4+}/Ir^{x+} ratios in Table 3.2). However, although Ir^{4+}/Ir^{x+} is similar to as-deposited, instable films, activated samples do not resemble those described as instable, neither electrochemically, nor morphologically. It follows that Ir^{4+}/Ir^{x+} as such is not a general indicator for stability or electrochemical activity of an IrOx thin film.

The inspection of XPS data and the SEM image of Fig. 4.5 shows that none of the investigated as-deposited films (RF cold or warm, DC cold) compares chemically with the activated films. In particular, the high concentration of hydroxides as well as the strong deviation from IrO_2 stoichiometry can not

$Q(O_2)$ [sccm]	Ir	IrO_2, $Ir(OH)_{3,4}$	Ir^{x+}, $x > 4$	O (IrO_2)	O (OH^-, O_2)	O (H_2O)	Ir^{4+}/Ir^{x+}
6.9	0	8.4	7.5	18.1	46.3	19.8	1.1
10.4	0	9.7	8.3	18.5	48.9	14.7	1.2
6.9 (act.)	0	6.2	6.5	3.3	71.6	12.4	0.9
10.4 (act.)	0	6.5	7.9	6.8	65	13.9	0.8

Table 4.3: XPS-deduced compositions [at. %] of two cold RF-sputtered IrOx films before (first and second row) and after activation (third and fourth row).

be found in any of the non-activated films. From the data obtained, it can be stated that similar to the activation of metallic Ir (formation of anodic IrOx films or AIROF), the activation of IrOx results in chemical alteration. Activation of IrOx proceeds to transfer between iridium oxide and hydroxide species. Upon activation, the morphology is transformed, which enables more redox centers to be reached by ionic solution and then to partake in reactions. The resultant structure, again similar to AIROF, can be described as an oxy-hydroxide of non-compact nature.

A more open structure is beneficial in so far as allowing a higher initial charge delivery in a pre-activated state, and facilitating activation, because charge transfer as well as activation are based on ion insertion into the material. A favorable structure depends on plasma excitation, oxygen partial pressure and substrate temperature. In this respect, of the investigated process conditions, DC-sputtering onto cold substrates at optimized oxygen flow has proven most useful for stimulation electrode coatings.

4.5 Summary

It was shown that the location and magnitude of maximum oxygen integration rates into growing IrOx films is influenced by the type of plasma excitation, whereas substrate temperature exerts minor influence. DC deposition favored the development of rough and voided films. In RF sputtering, a more expressed flux of energetic species to the substrate lead to the growth of smoother deposits. Additional heat supply amplified surface reorganization to form tighter packed films, partial crystallinity developed. Cyclic voltammetry and XPS analysis of reactively sputtered IrOx thin films showed that plasma excitation (RF, DC) and substrate temperature (cooled, 250°C) do not exert major influence on chemical composition. The existing strong dif-

ferences in electrochemical activity thus had to be explained on grounds of different morphologies.

It was further shown that activation of IrOx by repeated potential cycling in electrolyte alters the film composition in transforming between iridium oxides and hydroxides. As a result, the typical column structure of the deposit transmuted to a non-compact matrix, which enabled easier ion insertion to redox centers for charge transfer reactions. These observations are similar to other authors' results related to the activation of Ir metal.

DC-powered deposition of IrOx onto cooled substrates was most favorable for stimulation electrode coatings. Here, the most porous structures were deposited, allowing for both highest initial charge transfer capacity and strongest activation.

Based on the findings presented in this chapter, the following chapters describe simulations and experiments focussing on the atomistic mechanisms that cause the differences in morphology.

Chapter 5

Simulation of Sputter Deposition

This chapter contains a description of the simulations of sputter deposition of metallic Ir, and literature overviews pertaining to the simulations. They allow comparisons between experimental data and theoretical predictions, and thus enable to draw conclusions regarding the understanding of the deposition process. Furthermore, they are valuable tools for deriving useful parameters in future experiments. The simulation results and the comparison to experiments are detailed in chapter 6.

In the first part, the model of transport of sputtered Ir atoms from target to substrate is described. A description of the model of Ir film growth on the substrate follows in the second part.

5.1 Monte Carlo simulation of gas phase transport

5.1.1 State of the art

The model of sputter transport detailed in the following section is based on previously published works on Monte Carlo (MC) simulations of a diversity of sputtered materials [95–102]. The transport simulations trace the path of single atoms from their ejection from the target through the gas phase. Upon collisions with Ar background gas atoms, the particle changes direction and loses a fraction of its energy. Once the particle hits either substrate or chamber walls, the calculation is turned to the next atom. The simulations deliver a set of atoms with an impact angle from the substrate normal, an impact energy and an impact location. Mainly by way of collisions, the

results are determined by the choice of target-substrate working distance, background gas pressure and initial energy (determined by the target bias voltage).

Coronell et al. [95] simulated the transport of sputtered atoms during Ti deposition. A variable hard-sphere (VHS) model was employed which accounts for the variation of collision cross section with kinetic energy of the Ti atom. The energy of Ar atoms was assumed to follow a Maxwell-Boltzmann distribution. Different deposition setups were compared for deposition rate, symmetry and step coverage, with good agreement between measured and computed deposition profiles.

Also for sputtering of Ti, Motohiro [99] compared a hard-sphere (HS) model (constant collision cross sections of Ti and Ar) to a VHS approach. The latter was based on a potential interaction model. Regarding film thickness profiles, little differences between HS and potential interaction model were found. In case the sputtered atoms had lost their kinetic energy due to multiple collisions (known as thermalization), the further diffusive and non-directional movement through the sputter chamber was modelled by a random walk.

Comparisons of HS and VHS approaches were also presented by Serikov et al. [97]. The VHS model was closer to experimental growth rates of Al films. The simulation gained precision by reemission of atoms which had been deposited back onto the target due to scattering and diffusion. Further improvements in quantitative comparison with experimental deposition rates were achieved by accounting for flow fields of gas in the chamber.

Nakano and Baba [100] treated high pressure sputtering as a combination of MC and diffusive approach. They obtained the position of thermalized particles in the sputter chamber from MC calculations, and solved the Poisson equation to model the further diffusive movement at $5 \cdot 10^{-2}$ mbar. Compared to random walk approaches, the results were equivalent, the calculation speed, however, was drastically improved. Similar investigations were performed by Smy et al. [102].

The transport of a variety of atoms with different binding energies and masses at pressures from $5 \cdot 10^{-3}$ to $5 \cdot 10^{-2}$ mbar was simulated by Turner et al. [101]. The fraction of particles arriving at the substrate increased with atom mass and binding energy. An increase in pressure decreased the average kinetic energy of heavy atoms incident on the substrate. For atoms lighter than Ar, the mean kinetic energy at arrival was constant, which was explained by an increase in the proportion of high-energy atoms reaching the substrate. Atoms of low energy were preferentially reflected towards the target or scattered to the chamber walls.

Nathan et al. [98] modelled sputtering on a facing target geometry for elemental and alloy targets. The atoms' impact angular distributions hardly changed from $1 \cdot 10^{-2}$ to $10 \cdot 10^{-2}$ mbar.

Also the energy flux to the substrate during magnetron sputtering can be simulated by means of MC methods. This was reported by Ekpe et al. [96] for Al and Cu deposition. The contributions of impacting atoms, reflected neutrals, ions and electrons were accounted for. As the model neglected the diffusive transport to the substrate, the modelled energy fluxes and deposition rates were lower than the measurement values at high pressures and target-substrate distances.

Models for transport of sputtered Ir atoms have not been presented in the literature. Based on the above reports, the following section presents a Monte Carlo approach designed to model the sputter transport of Ir in the deposition tool used for the experiments.

5.1.2 Simulation procedure: sputter transport

Assumptions

The simulation makes use of a number of assumptions simplifying the calculations. The erosion profile of the target employed in the experiments was recorded, and a distribution was fitted to the measurements. It is used to determine the probabilities for selection of an ejection coordinate on the target. The chamber geometry is simplified to a cylindrical shape with a radius of 25 cm.

Ions were assumed to impinge normal to the target. Their mean incident energy was taken as $E_{ion} = 0.733 \cdot V_t$, as shown by Goeckner et al. [103] for a typical magnetron plasma. The target voltage V_t is an experimental value. The ejection energies of Ir atoms obey the distribution derived by Thompson [104]. Their polar ejection angles follow a cosine distribution [105], and ejection angles and energies were assumed not correlated [98].

The concentration of sputtered atoms in the gas phase was assumed small compared to the Ar atom concentration. Accordingly, Ir-Ir collisions are neglected [95]. The movement of Ar atoms is disregarded, except when considering thermalized Ir atoms, and Ir-Ar collisions are solely elastic. Ar atoms are only accounted for as collision partners. A variable hard-sphere model is applied for the calculations of mean free paths and scattering events [99]. The minimum Ir particle energy corresponds to thermal energy. Thermalized particles were assumed monoenergetic, their non-directionalized movement is modelled by a random walk [100]. The time dependence of transport events is neglected, and reemission of atoms returning to the target is not accounted

for. If an atom has moved 30000 free paths without having reached either chamber wall or substrate, the calculation is turned to the next particle.

In the simulator, the parameters working distance, background gas pressure and target bias voltage are held variable and are fed via a graphical user interface.[1]

Simulation policies

Upon impact of a high-energy Ar ion, a collision cascade in the target leads to the ejection of particles. Their energies are distributed according to

$$f(E) = \frac{1 - \sqrt{\frac{E_b + E}{\Lambda E_{ion}}}}{E^2 (1 + E_b/E)^3} \tag{5.1}$$

for $E \leq \Lambda E_{ion}$ [95, 104]. The incident ion energy $E_{ion} = 0.733 \cdot V_t$ [103], where the target voltage V_t is an experimental value, and the binding energy $E_b = 5.8$ eV. ΛE_{ion} is defined as

$$\Lambda E_{ion} = \frac{4 M_i M_t}{(M_i + M_t)^2} E_{ion}, \tag{5.2}$$

with the Ar atomic weight $M_i = 39.948$ and the Ir atomic weight $M_t = 192.22$.

The Thompson distribution of equation 5.1 can be represented by the majorant function

$$f(E) = 2 \cdot (1 + E_b/\Lambda E_{ion})^2 \cdot \frac{E_b E}{(E_b + E)^3} \tag{5.3}$$

for $0 \leq E \leq \Lambda E_{ion}$, and $f(E) = 0$ otherwise [97]. In order to simplify the sampling of energies, the majorant function 5.3 can be represented by

$$E = \frac{E_b \cdot \Lambda E_{ion} \sqrt{U}}{E_b + \Lambda E_{ion}(1 - \sqrt{U})}, \tag{5.4}$$

where U is a random number in [0,1[[97].

The polar ejection angle θ is calculated by rejection method from

$$f(\theta) = \cos\theta \cdot (1 + \beta \cdot \cos^2\theta), \tag{5.5}$$

where $\beta = 0.488 \cdot \ln\left(\frac{M_t E_{ion}}{M_i E_b}\right) - 2.44$ [106, 107].

---

[1]Both transport as well as film growth simulation were written in Matlab.

The azimuthal ejection angle (the angle of velocity projection onto the x-y-target plane) is chosen randomly in $[0, 2\pi[$. The starting position of sputtered atoms is at z=0.

After ejection, the sputtered particle travels a certain distance until it either suffers from a collision with an Ar atom or strikes a geometrical boundary. The free path λ is determined by [96, 108]

$$f(\lambda) = 1/\lambda_m \cdot e^{-\lambda/\lambda_m}, \tag{5.6}$$

and via inversion to

$$\lambda = -\lambda_m \cdot \ln(r_\lambda), \tag{5.7}$$

where r_λ is a random number in $[0,1[$. The mean free path is calculated from

$$\lambda_m = \frac{kT}{r_{sg}^2 \pi \cdot p}, \tag{5.8}$$

with the pressure p, the Boltzmann constant k and the gas temperature $T = 500$ K. The collision cross section is calculated from $r_{sg}^2\pi$, where r_{sg} is the interatomic separation of Ar and Ir, deduced from the repulsive Born-Mayer potential between the atoms [109]:

$$r_{sg} = r_{Ar} + r_{Ir} \simeq -\frac{2}{b_{Ar} + b_{Ir}} \ln \frac{E}{\sqrt{A_{Ar}A_{Ir}}}, \tag{5.9}$$

where A_{Ir}, b_{Ir}, A_{Ar}, b_{Ar} are Born-Mayer parameters for the sputtered and background gas atoms, respectively.

The energy-dependent collision cross section $r_{sg}^2\pi$ is also used to calculate the effects of scattering of Ir by Ar atoms. The collision parameter $b = r_{sg} \cdot sqrt(r_{col})$, where r_{col} is a random number in $[0,1[$, determines whether the collision is central ($b = 0$) or glancing [99]. The scatter angle χ in the laboratory frame is calculated by

$$\chi = \arctan\left(\frac{M_i \cdot \sin(\pi - a)}{M_t + M_i \cdot \cos(\pi - a)}\right), \tag{5.10}$$

with $a = 2 \cdot \arcsin(b/r_{sg})$ [110]. The azimuthal scatter angle is chosen randomly [99]. The new direction in 3D space is established by a coordinate system transformation [98].

The energy loss rate δ is calculated by [99]

$$\delta = \frac{M_t^2 + M_i^2 - 2M_tM_i(1 - 2(b/r_{sg}))^2}{(M_i + M_t)^2}. \tag{5.11}$$

This procedure is repeated for each atom until either a geometric boundary is reached or, upon a number of collisions depending on initial energy and collision parameters, the atom is thermalized to an energy $kT = 0.0428$ eV. The further movement is not directionalized. This is modelled by a random walk [100], meaning equal probability for movement in all space directions, the scatter cross section being determined by the sum of thermalized atom radii. The mean free path is determined by equation 5.8, completed by a factor $\sqrt{(1 + M_t/M_i)}$ accounting for thermal motion of Ar atoms [99].

Usually, $5 \cdot 10^5$ particles were simulated per run in order to limit calculation time.

5.2 Monte Carlo simulation of film growth

5.2.1 State of the art

This section gives an overview about the understanding of processes that govern the development of microstructure during sputter deposition of single-element films. Both experiments and simulations are taken into account. Special attention is paid to conditions where the effects of thermally activated diffusion can be assumed negligible, as is the case in the experiments discussed in the following chapter. Substrate temperatures were measured for selected depositions, and were rarely increased by the process, with maximal temperatures around 85 °C. This results in homologous temperatures $T_{substrate}/T_{melt} \approx 0.1$. The mobility of an atom arriving on the substrate (known as the adatom) can be assumed to be determined primarily by kinetic energy-assisted effects.

The literature overview provides a basis for the understanding of the simulation of Ir film growth, the details of which are outlined in the next section. Using the transport simulations as input, i. e., incident atom energies and angles, Ir thin film growth is modelled in two dimensions. The morphology is evaluated as a function of pressure, working distance, and bias voltage (which results from the choice of input power). The structures are analyzed regarding film density, atom accessibility by ionic solution, and crystallographic orientation. The resulting configurations can be used to predict and explain the growth of experimentally realized deposits, which are evaluated with respect to their electrochemical performance. The results are presented in chapter 6.

Much experimental and theoretical research has been dedicated to understanding the evolution of microstructure during thin film deposition. Thornton found that the microstructure of different metallic coatings such as Cu,

Fe, Ti, Mo, Al or Ni can be varied between three different morphological zones by adjusting total sputter pressure, temperature and deposition geometry [85].

The understanding of the evolution of a zone I microstructure is of greatest importance for the films discussed within this work. This type of microstructure is characterized by a void-separated columnar growth and a rough surface appearance. Films of low density evolve [86]. Their growth has been understood as follows: Initial nuclei on the substrate grow to form islands (Volmer-Weber or Stranski-Krastanov mode), the islands expand and coalesce. Further deposition leads to grain coarsening and channel formation between the grains [111, 112]. Shadowing effects and a limited mobility of the incident atom lead to the growth of columns which are separated by open boundaries. Shadowing effects occur if atoms impinge at an angle and not orthogonal to the substrate. High points on the surface receive more material than low points, and hillocks and valleys develop. A low adatom mobility does not enable the compensation of shadowing effects. As diffusion is limited, the surface is scarcely reconstructed to minimize free surface energies [112–114]. Low adatom mobility is primarily caused by a low substrate temperature, but can be amplified by low kinetic energy of the adatoms.

Based on the structure zone model, several authors investigated other materials and sputter parameters, for instance target-substrate working distance [115], sputter angle [116], and deposition rate [117]. Working distance and sputter angle primarily influence the adatom's kinetic energy, and the expression of shadowing on the substrate. At high deposition rates (above 5-10 μm/min [117–119]), incident atoms can disturb thermally activated diffusion of prior deposited atoms.

The above investigations showed that the polar impact angles of adatoms, as well as their mobility on the surface, decisively influence film morphology and surface topography. In order to model the development of a certain microstructure, detailed information regarding the atomistic mechanisms is needed. Most published research on these mechanisms is of simulative/theoretical nature. Nevertheless, also a few experimental results have been reported.

Atomistic mechanisms of film growth

Using field ion microscopy, Morikawa et al. [120] observed directional migration of Cu deposited onto cooled W tips. In the absence of thermal activation, the biased diffusion was ascribed to kinetic momentum of the arriving atoms. This is illustrated in Fig. 5.1a). The energy of an arriving atom is not com-

pletely dissipated into the lattice. Some of the momentum is retained, and it can skid along the surface.

Several authors investigated biased diffusion by means of molecular dynamics (MD) simulations. The most comprehensive studies were performed by Zhou and Wadley on Cu deposition [121]. Depending on angle and energy, the adatom skipped over distances of more than 10 nm. For small energies, the biased skipping distance is negligible. At higher kinetic energy, and for incident angles greater than about 20° from the substrate normal, the distances increase with angle, and become maximal around 80°. At higher angles, surface attractions bend the adatom path sideways or backwards. The adatom takes its final position preferentially at ledges or terraces, as indicated in Fig. 5.1a). The authors fitted analytical expressions to the simulated data, which were later used as input for MC simulations of film growth [122–124].

Similar results were reported by Kools [125]. He used MD simulations of Cu deposition to investigate the effects of biased diffusion on shadowing. At low incident kinetic energy, shadowing was dominant due to low mobility of the adatoms, and rough and voided films developed. At higher incident energies between 3 and 20 eV, shadowing was largely suppressed, and defects were annihilated as the film grew.

Dodson [126] performed MD simulations of 10-100 eV Si deposition. Incident kinetic energies smaller than 25 eV caused only small surface diffusion paths. At grazing incidence and higher energies, biased diffusion was observed over dozens of unit cell lengths.

A combined MC and MD approach was used by Jacobsen et al. [127] to study the growth of several monolayers Ag and Pt. They report on energy-induced defect formation and annihilation, whereby the mobility of adatoms was in the range of a few interatomic distances. Short diffusion lengths were used to model rough surfaces developing during Al deposition (Hansen et al., [128]).

In summary, the above authors showed that biased diffusion lengths are dependent on kinetic energy and incident angle, as well as on the atomic roughness of the film. At small incident angles, the adatom surface diffusion is not biased, and the traversed paths decrease. This is illustrated in Fig. 5.1b). In these cases, most kinetic energy is absorbed by the lattice.

At sufficient energies, arriving adatoms can resputter the deposited film. This is illustrated in part c) of Fig. 5.1, where an incident atom causes a collision cascade in the film, which ejects a lattice atom of low coordination number. Again, comprehensive MD simulations were published by Zhou and Wadley [129]. It was shown that a 50 eV Cu adatom penetrates the surface and occupies a lattice site. Due to energy transfer, a collision cascade is initiated and an atom is ejected at 45° and an energy of 5 eV.
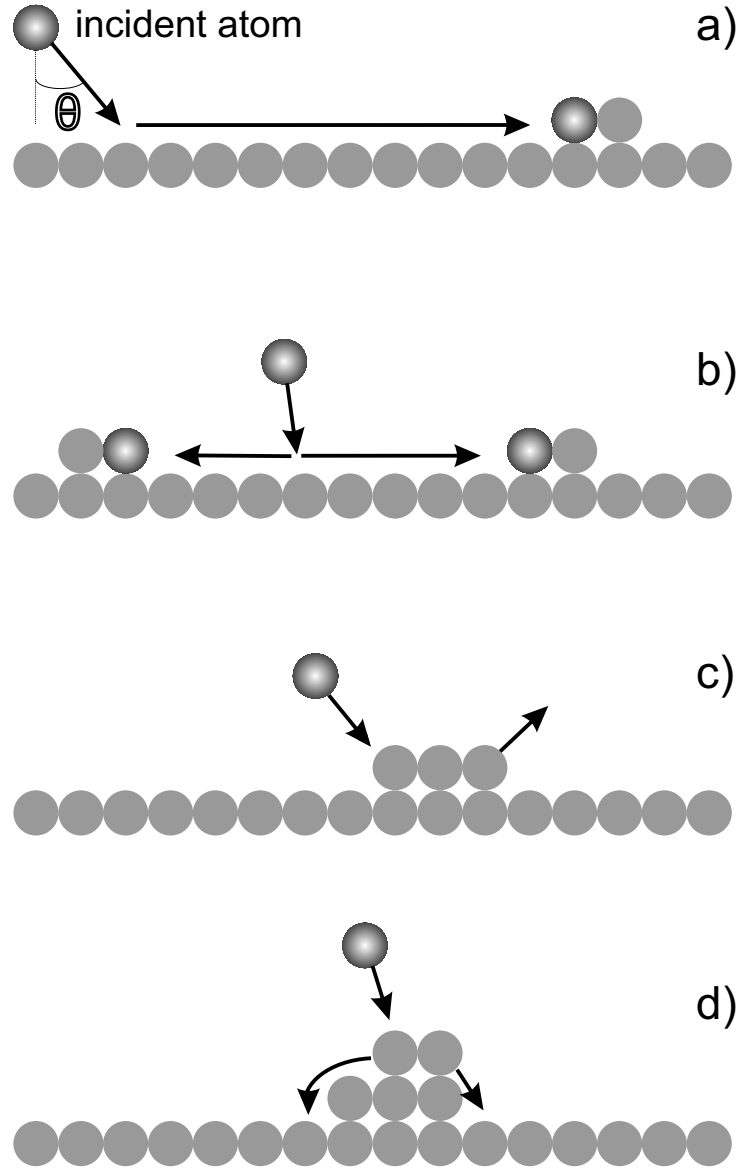
Figure 5.1: Schematics of interaction events between surface and adatom. The lighter colored atoms are part of the existing thin film. The arriving adatom is highlighted, as are possible positions after biased diffusion in a) and isotropic diffusion in b). c) illustrates a resputtering event of a previously deposited atom due to high-energy impact. d) shows lattice reorganization due to a thermal spike caused by the arriving adatom. Two film atoms are indicated to relax into positions of equal or higher coordination.

The resputter probability was analyzed as a function of energy and incident angle. The energy threshold for resputtering is determined by the binding energy of the material, a minimal energy of around 20 eV was required in the case of Cu [129]. The yield is maximal around 30-45° of incidence. This was also shown by Hamaguchi and Rossnagel [130] by way of continuum simulations of profile growth during ionized sputtering.

At higher incident angles, the resputter probability decreases. Instead, the adatom can be reflected from the surface, provided it has a sufficient kinetic energy [129].

Apart from the deposited elements, the growing film can also be reached by high-energy Ar neutrals that are reflected from the target, as well as by Ar ions [86,96,113,130]. Ar species can resputter the deposited material and induce a higher surface mobility.

Fig. 5.1d) describes the effects of a thermal spike. It results from the transient increase in effective temperature near the impact site due to the transfer of adatom energy to lattice vibrations. At an incident kinetic energy of zero, the thermal spike is caused by the latent heat of condensation. It corresponds to the potential difference between a free atom and an atom at a surface site. At an incident kinetic energy greater than zero, the thermal spike develops as a combination of latent heat of condensation and partial dissipation of kinetic energy. Based on well-validated data, Zhou and Wadley showed by MD simulation for Cu that 60-70% of the latent heat of condensation is transferred to additional kinetic energy of the impinging atom. The added velocity component is directed towards the capturing atom [121].

Even at zero initial kinetic energy, the latent heat release can cause a thermal spike up to an effective local temperature of 1000 K for 0.5 ps. Although no biased diffusion or resputtering can occur at these low incident energies, the heat results in additional surface mobility [129]. Already at kinetic energies of 3 eV, the spike can cause defect elimination in subsurface layers. Vacancy filling sets in, and neighboring atoms relax.

Similar results were achieved by Dodson [126] via MD simulations of 10-100 eV Si deposition. A localized transient energy spike was induced by adatom arrival which activated modifications of the atomic configuration. Also Gilmer and Roland [131] performed MD simulations of energetic Si deposition. They found that a higher incident energy was coupled to stronger ordering at constant substrate temperature. The release of latent heat as such did not cause the adatom to migrate further, but atomic rearrangement occurred due to local heating. In the absence of thermally assisted diffusion, it was the only cause of rearrangement. It was further shown that local heating is a function of the kinetic energy of the adatom. Experiments indicating epitaxial growth of Fe and Cu on Ag in the absence of thermally activated

diffusion were presented by Egelhoff and Jacob [132]. The latent heat of condensation was assumed as the source of adatom mobility. Contrarily, Jacobsen et al. [127] attributed atomic rearrangement, defect formation and annihilation to ballistic causes upon adatom impact.

Simulations of microstructure evolution

Different approaches have been employed for the modelling of film growth during sputter deposition. Continuum methods are used to calculate film growth profiles [133]. Topographies at different deposition stages can be depicted, but the approach is less suited for modelling the microstructural development including micro-voids and grain boundaries. This can be achieved using atomistic models.

MD methods trace lattice atom vibrations and calculate forces on atoms several times per vibration period, where the shortest lattice vibration periods are about 10^{-13} s. The methods allow the detailed description of single-atom behavior on surfaces. However, they are computationally intense and the calculation is limited to small system sizes [121, 122, 129].

Probability-based MC methods have proven most effective for the simulation of thin film morphology. The detailed interatomic forces are not evaluated and the movement of atoms is determined by a set of rules established beforehand. The greatest advantage of MC models is the inclusion of atomistic effects at short computation time. Disadvantages are the pre-selection of crystal lattices and atomistic events included into the simulation, and the general simplifications made regarding diffusion and atom rearrangement.

Most published models are concerned with the growth of films commonly used in the construction of interconnects on silicon, such as Al, Cu, W or Ta [113, 114, 134, 135]. The deposition over topographies is simulated frequently, and the films are characterized regarding density, crystallographic orientation, grain size distributions, and surface topography. Substrate temperature is most frequently modelled as the main influence on film microstructure. However, also the influence of incident adatom angles and deposition rate on film growth has been investigated [136, 137]. The evolution of film morphology in dependence of adatom energy has been modelled by Smy et al. for W deposition [138], Torre et al. [113] (Ta), Liu et al. [124] (Cu) and Yang et al. [122, 123] (Ni).

As mentioned in the preceding section, Zhou and Wadley [121, 129] performed MD simulations of Cu deposition, and described in detail the energy and angular dependence of reflection, resputtering, biased diffusion and thermal spike. The results were fitted to analytical expressions, which were then

used for MC simulations of Cu deposition [124] as well as for Ni deposition, the element neighbor of Cu [122, 123].

Yang et al. [122] used monoenergetic and cosine-distributed angular incidence of atoms to illustrate the influence of kinetic energy-assisted mechanisms on film morphology. The 2D simulated films were evaluated with respect to surface roughness and morphology. The surface roughness rapidly decreased with an increasing incident energy until a minimal roughness was reached. Furthermore, it was shown that effects due to arrival of energetic atoms become negligible at temperatures above $T_{substrate}/T_{melt} = 0.22$. Similar observations regarding the decrease in surface roughness and increase in packing density with increasing incident energy were reported by Liu et al. [124] on Cu deposition. They also showed that surface roughness can be influenced by drastic changes in deposition rate. Both publications did not include comparisons to experiments.

The model described in [122] was also employed to optimize the coating of trenches [123]. Smooth sidewall coatings were deposited at relatively high incident energies around 70 eV. This could be explained by the film redistribution due to biased diffusion, reflection and resputtering. The same effects also explained experimentally observed material accumulation in corners.

Smy et al. [138] incorporated biased diffusion into their MC simulator SIM-BAD, which enabled to explain experimentally observed lateral overgrowth of trenches and steps during W deposition. Incident atoms were allowed to skip across the surface before occupying a surface site. The skipping lengths were determined by the angle of incidence, the kinetic energy, and proportionality constants, which were matched to experimental results. The effects of resputtering or latent heat release were not included.

The 3D growth simulator ADEPT accounts for the effects of thermally activated diffusion and deposition rate on the microstructure of a sputtered film [118]. It was extended to model the influence of latent heat release, reflection, resputtering, biased diffusion, the diffusion of prior deposited surface atoms due to impact, and energetic bombardment by Ar atoms [113]. The energies of impinging Ta and Ar atoms were estimated and assumed monoenergetic. Good agreement between measured and modelled densities were only achieved if the energy of the incident Ta atoms was increased to 10 eV. Ar bombardment had only weak effects on film density.

As in the case of transport simulations, a model describing the growth of Ir thin films has not been reported on. Experimentally, the formation of islands and their coalescence during evaporation under ultra-high vacuum were observed by means of scanning tunneling microscopy [139]. On perfect Ir surfaces, single Ir atoms were shown to be highly mobile upon thermal activation [139, 140], and the formation of Ir stacking faults and preferential

hexagonal close-packed binding on surfaces have been observed [139, 141, 142]. Models of dimer and island formation during the initial stages of Ir evaporation were presented [139, 142].

Apart from these insights into the initial stages of Ir thin film growth, the evolution of Ir or IrOx thin film microstructure has not been investigated in detail. Furthermore, the influence of angular or energetic distributions of sputtered adatoms on stimulation electrode characteristics in general has not been clarified.

5.2.2 Simulation procedure: film growth

Assumptions

The simulation accounts for a number of fundamental film growth processes and mechanisms. It focusses on the major energy impact induced mechanisms contributing to microstructural evolution, i. e., kinetic energy-induced diffusion, latent heat and resputtering, which were described in Fig. 5.1.

It was assumed that these kinetic energy-induced mechanisms are in principle valid for deposition of Ir, however, detailed investigations were not available. Thus, the model interprets other authors' findings in a generalized manner for the deposition of Ir (see section 5.2.1 for a literature overview).

Substrate temperatures were measured for selected depositions, and were only rarely elevated (maximally 85 °C), equivalent to homologous temperatures $T_{substrate}/T_{melt} \approx 0.1$. At these homologous temperatures, thermally activated diffusion does occur on the surface, but the effects can be assumed of much lower importance compared to those of kinetically induced atom rearrangement [85, 112].

Knock-on diffusion, i. e., the biased diffusion of a surface atom due to transfer of kinetic energy of a newly arriving atom, is not accounted for. Ar implantation into the film as well as film bombardment by Ar are disregarded. Furthermore, the simulation does not account for reflection of incident Ir atoms.

Deposition time and thus deposition rate was not included. The deposition rates of processes discussed in chapter 6 are around and mainly below 0.1 μm/min. It can be assumed that atomic diffusion events are completed before arrival of the next atom [117–119]. This implies that the film characteristics are unaffected by the small changes in deposition rate between experimental settings.

The simulation models a polycrystalline columnar growth, backed by XRD and SEM data. The crystal structure was assumed purely face-centered cubic (fcc). The substrate was represented by defect-free monolayers of the same

θ_{local}(50eV) [°]	$P_{\{111\}}$	$P_{\{220\}}$	E_{ad}(40°) [eV]	$P_{\{111\}}$	$P_{\{220\}}$
$30 \leq \theta < 50$	0.3	0.55	$20 \leq E_{ad} < 50$	0.15	0.35
$10 \leq \theta < 30$ & $50 \leq \theta \leq 60$	0.15	0.15	≥ 50	0.35	0.6

Table 5.1: Resputter probabilities P on different faces for different local angles at an adatom incident energy E_{ad}=50 eV and probabilities P for different E_{ad} at 40°. Adapted from [129, 130].

structure. XRD data did not reveal an influence of substrate or adhesion layer on crystallographic orientation.

Simulation policies

Modelling of crystallographic structure All atoms are positioned on lattice sites. Interstitials are not allowed, contrary to other lattice defects such as vacancies and grain boundaries. Crystallographic orientation was included as a parameter in order to account for texture development caused by adatom energy characteristics [112, 118]. Notably, orientation is only represented by different energetic framesets for diffusion and resputtering, an alteration of the representation as such (interatomic distances and lattice sites in the unit cell) is not necessary for the purposes described here. Of the three detected orientations (see section 6.4.1), the {111} and {220} families dominate orientation and compete for texture, and thus are the only lattice planes considered. Atom exchange between grains is not specifically modelled.

Modelling of resputtering Resputtering of Ir by an Ir adatom is modelled following the simulations of Zhou and Wadley [129], and Hamaguchi and Rossnagel [130]. Resputtering can occur if the Ir adatom energy is higher than 20 eV and the local angle lies between 10° and 60°. The resputter probability is calculated and, if greater than a random number, resputtering proceeds. The probabilities for resputtering on different crystal orientations at different local angles and an incident energy E_{ad}=50 eV can be found in Table 5.1 [129, 130]. It also includes resputter probabilities for different E_{ad} at 40°. At other combinations of energies and angles, the probabilities are calculated by $P(E, \theta) = P(E, 40°) \cdot P(50\text{eV}, \theta)/P(50\text{eV}, 40°)$, where $P(50\text{eV}, 40°) = P_{max}$. The reduced bond energies of atoms in grain boundaries are not explicitly considered [119, 134].

To mimic the energy transfer and collision cascade within the material upon high-energy impact, a region defined by three atomic distances from

the impact point is searched for the atom of lowest coordination number. This atom, with the lowest bond strength to the crystal, is then ejected and deleted from the simulation [129].

Resputtering by energetic Ar was shown to have little effect on a film composed of heavy atoms (Ta in the report of Dalla Torre [113]), and thus was omitted.

Modelling of kinetic energy-induced diffusion Diffusion is modelled by accounting for the system attempt to reduce surface and interfacial energies [112–114]. Consequently, a diffusion event has to effectuate an increase in coordination number of the atom [113, 118]. The neighborhood of an atom is searched for empty sites within a diffusion length; the place of highest coordination is then occupied [143]. In general, this site exchange proceeds on the surface, however, also sub-surface vacancies may be filled [126, 127].

The diffusion lengths are short in order to account for the high defect density providing edges and vacancies that inhibit further movement. The maximum possible diffusion lengths are calculated adapting literature data on adatom surface diffusion [121, 125–128] and are matched to the experimental results.

For near-normal incidence, it was assumed that parts of the kinetic energy available at impact can be used by the atom for migration. Surface diffusion proceeds in an isotropic manner, with relatively localized atomic movement (see Fig. 5.1b). The covered paths are potentially longer if the diffusion is of biased type [121, 126]. This is the case for incident angles greater than 20°, measured from the substrate normal (see Fig. 5.1a).

Table 5.2 shows the maximum diffusion lengths L_{max} in interatomic distances d on {111}. They are determined both by the kinetic energy of the incident atoms as well as their incident local angle. For the smallest energies, $L_{max} = 1$, equivalent to relaxation to a nearest neighbor site.

For diffusion on {220} faces, and if the incident atom has a kinetic energy greater than 1 eV, the lengths are scaled with the ratio of activation energies for thermal diffusion, $E_{m,111}/E_{m,220} = 0.36$ [141, 144]. Diffusion lengths on {220} can become too small due to scaling. In these cases, an eventual bias is removed from the diffusion and an isotropic diffusion length of 3 is substituted.

The bond strength of adatoms to the substrate can be assumed smaller than that of Ir-Ir, and the diffusion length is doubled, which leads to the clustering and island formation usually observed during metal film growth [134].

E_{ad} [eV] θ_{local} [°]	kT	$kT < E_{ad} \leq 20$	> 20
< 20	$L_{max}^{+} = 1$	$L_{max}^{+} = 0.94 \cdot E_{ad} + 2$	$L_{max}^{+} = 20$
$20 \leq \theta < 50$	$L_{max}^{+} = 1$	$L_{max}^{*} = 0.94 \cdot E_{ad} + 6$	$L_{max}^{*} = 24$
$50 \leq \theta < 75$	$L_{max}^{+} = 1$	$L_{max}^{*} = 0.94 \cdot E_{ad} + 8$	$L_{max}^{*} = 26$
≥ 75	$L_{max}^{+} = 1$	$L_{max}^{*} = 0.94 \cdot E_{ad} + 10$	$L_{max}^{*} = 28$

Table 5.2: Matrix determining the maximum diffusion lengths L_{max} [interatomic distances d] of Ir on Ir {111}. L_{max} depends on incident energy E_{ad} and local incident angle θ_{local}. $^{+}$: isotropic diffusion, *: biased diffusion. kT: thermalized atom with E_{ad}=0.0428 eV. For diffusion on {220}, the lengths are scaled with the ratio of activation energies for thermal migration. Adapted from [121, 125–128].

For all diffusion events considered in this simulation, the atom is allowed to perform multiple jumps within one event, which is a convenient way of representing complex diffusion or exchange mechanisms [127]. Furthermore, atoms are allowed to pass through sites of zero coordination [118, 119].

Modelling of latent heat release and thermal spike   Upon adatom impact, a search radius is defined within which lattice reorganization can occur. The radius depends on the kinetic energy of the incident atom, but is small as shown for Cu [121] and Si [126, 131]. The thermal spike is modelled by picking the atom of lowest coordination within this radius and moving it to an empty site of highest coordination, thus reducing interfacial energy in the system. Furthermore, dependent on kinetic energy, more than one reorganization event is allowed. Table 5.3 shows the search radii and event repetitions as a function of adatom kinetic energy. Atoms that undergo biased diffusion (i. e., that arrive at angles greater than 20°) dissipate less energy into the lattice. This is accounted for by reducing the search radius upon off-axis impact.

The effects of thermal spike and latent heat release are independent of lattice orientation. Although the latent heat contribution (i. e., binding energy) differs, the distributed energy per surface atom is the same in the impact area. On a surface of high binding energy, the adatom has a higher number of nearest neighbors – an adatom on {220} has a coordination of five, and the deposited energy is distributed on more atoms, whereas an adatom on the low-binding-energy {111} has a coordination of three.

E_{ad} [eV]	R [d]	*Iterations*
$kT < E_{ad} \leq 1$	2	1
$1 < E_{ad} \leq 10$	2^*, 3	2
> 10	2^*, 3	3

Table 5.3: Search radii R [interatomic distances d from the impact point] for lattice reorganization due to thermal spike as a function of adatom energy. *Iterations* describes the maximum number of site exchanges due to one impact. *: for incident angles greater than 20°. Adapted from [121, 126, 131].

Simulation procedure

- After the definition of a substrate, single particles are inserted into the simulation. Their x-starting point is random along the substrate width, their initial height corresponds to the maximum height of the existing film. The angle with respect to the substrate normal is retrieved from the corresponding transport simulation, as well as the kinetic energy.

- The new atom travels along a straight path according to its incident angle. Along this path, a search range is defined spanning a width of two atomic diameters. The film atom capturing the incoming one is the closest atom within the search box.

- The new particle can leave the simulated area on one side without being captured. It reenters the simulation on the opposite side (periodic boundaries) until a capturing atom is found or 100 paths are completed, in case of which it is removed.

- The incident atom is assigned the crystallographic orientation of the atom it first makes contact with. In case the atom hits the bare substrate, it is first allowed to complete diffusion events. Afterwards, it takes the orientation of its nearest neighbor. In case no nearest neighbor is found, the orientation is chosen randomly.

- The local normal needed for biased diffusion and resputtering is calculated based on the locations of nearest neighbors.

- Resputtering is considered if the adatom incident energy is higher than 20 eV and the local angle lies between 10° and 60°.

- The preliminary lattice position of the new atom relative to the capturing atom is determined geometrically.

- It is decided whether surface diffusion proceeds in a biased or isotropic manner, the maximum diffusion length is defined according to local angle and energy. The radius for execution of reorganization initiated by thermal spike as well as the number of events are scaled with the incident energy.

- The maximum diffusion length is scaled according to lattice orientation, and isotropic or biased diffusion are carried out.

- The lattice reorganization due to thermal spike is calculated.

- A new atom is inserted.

The choice of substrate width (usually 200 atoms) allows comparison with fracture cross section SEM images as well as electrochemical, XRR and XRD measurements. 200 atoms correspond to roughly 76 nm in an Ir single crystal, the unit cell height being 3.839 Å.

As to the definition of density, several options have been presented in the literature. In general, it is defined as the ratio of occupied over total number of sites in the layer. In this work, the total number of sites is defined by multiplying substrate width and an average film thickness. The latter is calculated by dividing the substrate into five equal-sized sections and averaging over the maximum heights within these sections.

Chapter 6

Design of Ir Thin Films

Chapters 3 and 4 had shown that a more porous morphology enables an easier insertion of ions from the electrolyte into the coating. This chapter discusses the atomistic effects that determine the microstructure of metallic Ir thin films. Their understanding can be used to further foster the development of open surfaces. The influence of pressure, working distance and input power on the films' microstructure is detailed, focussing on conditions leading to low adatom kinetic energy.

The first part of the chapter details simulations regarding the gas phase transport of sputtered atoms to the substrate (see section 5.1.2 for simulation policies). Film growth on the substrate is simulated and discussed in the second part (see sections 5.2.1 and 5.2.2 for theory and simulation details). The third and fourth parts detail experimental results and the comparison to simulation outputs. Finally, in the next chapter, the findings on Ir atom transport and film growth are combined with those of the previous chapters on reactively sputtered films.

6.1 Transport of sputtered Ir atoms

6.1.1 Verification of the transport model

Simulations regarding the transport of sputtered atoms are best verified by comparing simulated spatial distributions of incident particles to experimental film thickness profiles. As an example, Fig. 6.1 shows measurements and simulations of film thickness distributions across a wafer processed at 180 W, a WD of 85 mm and $4.7 \cdot 10^{-2}$ mbar. The comparison shows that film thickness profiles, being a direct result of transport properties, are well predicted by the simulations.

The simulations do not account for substrate plate rotation. In order to be able to compare measurements and simulations, the substrate was held stationary during deposition. However, due to a faulty process tool setting, it was not aligned with the target center. Instead, looking from above, the substrate center was positioned to the left and lower than the target center. Hence, the typical magnetron deposition profile is shifted.

The profile of Fig. 6.1a) shows the thickness orthogonal to the wafer flat, which, in the sputter chamber, corresponds to measurements on a line running along the target edge. The absolute film thickness variations are low compared to Fig. 6.1b). Here, the measurements were taken on a line running towards the target center. A monotonic increase of values results.[1]
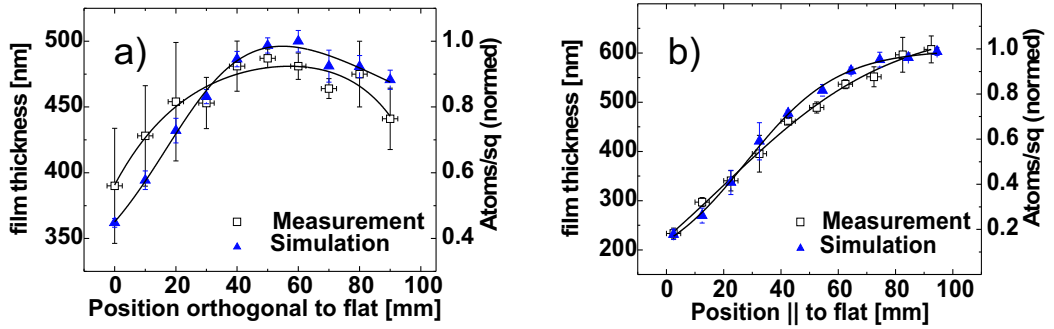
Figure 6.1: Measurements (square symbols) and simulations (triangles) of film thickness distributions across a wafer. a) Thickness at positions orthogonal to the flat. b) Thickness at positions parallel to the flat. As explained in the text, the wafer was not centered below the target.

Fig. 6.1 also includes the uncertainties of incident location evaluated by repetitive simulations. As to atom energetics and impact angles, the deviation between repetitions is less than 1%.

The model was further validated by cross-referencing to results calculated at the Institute for Surface Technology, RWTH Aachen University [145].

6.1.2   Energy and angular distributions of incident atoms

Distribution of incident angles

Fig. 6.2 illustrates the influence of increasing pressure on the sputtered atoms' impinging angles θ, measured from the substrate normal. Part a) of Fig. 6.2

---

[1]In order to minimize film thickness variations, all experiments were performed with a rotating substrate plate (see section 2.1).

p [mbar]	$\theta_{m,total}$	θ_m, kT$< E <$10 eV	θ_m, $E >$10 eV	θ_m, $E=$kT	$\theta(P_{max})$
$1.6 \cdot 10^{-2}$	31.3	33	28.1	(*)	13.2
$9.3 \cdot 10^{-2}$	28.9	28.5	23.4	29.4	20.4
$1.7 \cdot 10^{-1}$	28.9	26.5	(*)	29.4	8.8

Table 6.1: Average impact angles θ_m [°] within certain energy bands and most probable angle $\theta(P_{max})$ [°] of incident particles as shown in Fig. 6.2. (*): insignificant contribution.

shows simulation results computed for p=$1.6 \cdot 10^{-2}$ mbar, b) includes results for p=$9.3 \cdot 10^{-2}$ mbar, and c) for p=$1.7 \cdot 10^{-1}$ mbar. The remaining parameters WD=45 mm and bias voltage V_b=385 V were constant.

All three graphs include the normalized distributions of the total angle as well as angular distributions of atoms at different energies. Their mean values are extracted into Table 6.1.

The angular distribution of Fig. 6.2a), at a pressure typical for magnetron sputtering, is composed of two contributions. The first one includes all atoms of energy higher than 10 eV. Its most probable angle is 12.4°, the mean and median angle are 28.1° and 25.1°, respectively. For an atom ejected at 20 eV, at a pressure of $1.6 \cdot 10^{-2}$ mbar, the mean free path is 3.6 cm, in the order of WD. If emitted at a small angle, the particle will likely reach the substrate experiencing less than three collisions (the median of collisions is 2 for this group of atoms). Because the mean free path is smaller than the WD, the arriving atoms' angular distribution deviates from the initial ejection cosine distribution.

If the atom is ejected at a relatively high angle, but within the same high-energy region, its probability of reaching the substrate without scattering is lower. Also, if the atom's initial energy is lower, it is preferentially scattered, as the mean free path becomes shorter. Hence, the second contribution to Fig. 6.2, comprising non-thermalized atoms of energies lower than 10 eV, is centered to the right and peaks at 19°, the mean (median) angle being 33° (30.5°). On average, those particles that arrive at larger angles have suffered more collisions, correlating with their lower energy, as has been found by other authors [101, 146]. This is further underlined by Figs. 6.2b) and c), where the mean incident angle of the medium-energy contributions are greater than those of the respective high-energy bands (Table 6.1).

Nevertheless, also atoms within the medium- or high-energy bands can impinge on the substrate at larger angles (see Fig. 6.2a). These contributions become smaller as the pressure is increased. As the number of collisions increases, the atoms emitted at large angles lose energy and are removed
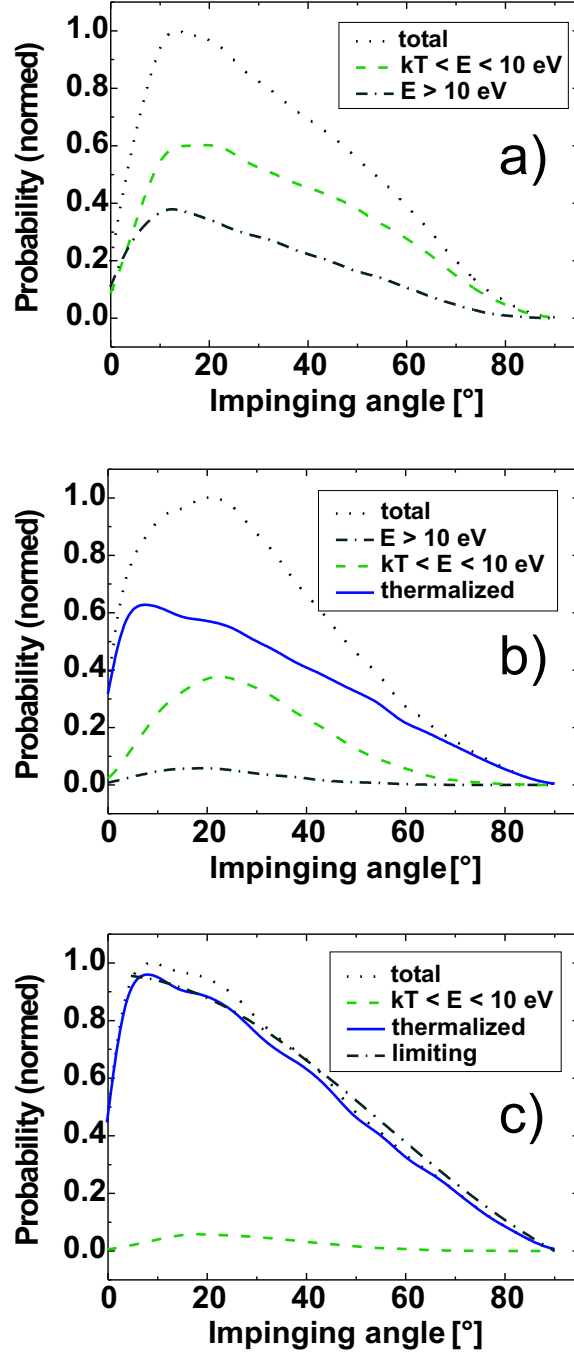
Figure 6.2: Simulated incident angular distributions of atoms sputtered at WD=45 mm and V_b=385 V. The pressure increases from p=1.6 · 10^{-2} (a) over 9.3 · 10^{-2} (b) to 1.7 · 10^{-1} mbar(c). Included are angular distributions of atoms arriving in different energy bands.

from their medium- or high-energy band. Thus, at higher pressures, only medium- or high-energy atoms of small angles reach the substrate (compare these contributions in Figs. 6.2a) and b). The mean incident angles within the medium- and high-energy bands decrease upon an increase in pressure (Table 6.1).

Already for a pressure of $9.3 \cdot 10^{-2}$ mbar (Fig. 6.2b), the contribution of thermalized atoms, i. e. those diffusing towards the substrate, overweighs those of medium and high energies. Accordingly, the mean and median angle of the total distribution shift to smaller values ($28.9°$ and $26.2°$, respectively), which is greatly influenced by the mean (median) angle of $29.4°$ ($26.1°$) of the thermalized atoms.

Finally, at the highest pressure (Fig. 6.2c), the thermalized contribution determines the overall curve shape. Roughly 95% of all incident atoms have lost their initial kinetic energy and diffuse to the substrate. According to Smy et al. [102], the angular distributions of thermalized atoms can be described by $f(\theta) = cos\theta + 3/4 \cdot s \cdot cos^2\theta$. Assuming a unity sticking coefficient s, the limiting distribution is plotted in Fig. 6.2c), and matches the simulated angles.

The average incident angles, summed over all contributions, do not change considerably (see Table 6.1). Upon an increase in pressure by more than an order of magnitude from $1.6 \cdot 10^{-2}$ over $9.3 \cdot 10^{-2}$ to $1.73 \cdot 10^{-1}$ mbar, the average angle decreases only from $31.3°$ to $28.9°$. Similar results have been reported for facing-target sputtering at comparable pressures by Nathan et al. [98].

The main differences in angular distributions are evident between high and medium energy adatoms, where, on average, a larger incident angle correlates with a lower energy of the particle.

From the above, one can presume a minor influence of the changes in angular distribution on the microstructure of sputtered films. As the angles are broadly distributed in all cases, geometrical shadowing will occur for all conditions. Equivalent results have been reported by Turner et al. and Myers et al. [101, 146]. Taking the angular influence alone, the growth of underdense material will be initiated for all investigated conditions. However, the particle energies can act both in a supportive and obstructive manner regarding the development of a columnar, open material.

Adatom energy distribution

Fig. 6.3 shows the mean adatom energy as a function of $p \cdot WD$. The pressure-distance product is plausible to refer to, as pressure and WD, by way of determining the number of collisions, have the same effects on particle trans-

port. The overall curve shape is similar to earlier reports; at low $p \cdot WD$, a significant fraction of atoms retains its emission energies, at a high pressure-distance product, most atoms have low energies [96, 101, 108]. The exact curve shape, however, differs between the authors, it mainly depends on the initial energies and the mass ratio of sputtered to inert gas atoms, which influences the energy loss per collision [101].

Fig. 6.3 includes the total mean energy as well as the mean energies of particles arriving at angles larger or smaller than 30°. Corroborating the results of the previous section, the average atom arriving at smaller angles has a higher energy than its counterpart arriving at larger angles. The differences are greatest around $p \cdot WD = 1$ mbar $\cdot$ mm (logarithmic scale in Fig. 6.3). At the lowest $p \cdot WD$, an atom with ejection angle greater than 30° either does not reach the substrate and thus is removed from the simulation, or undergoes only a small number of collisions, which does not result in severe energy loss. This leads to the small energetic difference between the two angular groups. On the far side of the graph, the mean energy is determined by the thermalized atoms (see Fig. 6.2c), and differences between high- and low-angular adatoms can no longer be seen.

The influence of altered bias voltage is not included in the graph. All experimental sets were run at three input powers, resulting in different bias voltages for simulation. The bias voltages used for the simulations shown in Fig. 6.3 and following are the lowest values available for each set of conditions. Increasing the bias voltage from 320 to 400 and 430 V, at $p \cdot WD = 4.1$ mbar $\cdot$ mm, the mean ejection energy increases from 22.2 over 23.9 to 24.3 eV. As a result, the mean free path is elongated, which decreases the average number of collisions (see equations 5.4 and 5.8). In effect, the mean incident energy rises from 1.6 to 2.2 and 2.3 eV.

Fig. 6.4 shows the fraction of particles arriving in the thermalized state as well as the deposition efficiency (numbers of arrived over released particles), again as a function of $p \cdot WD$. The data points lie on a single curve [108].

The fraction of thermalized particles already reaches 66% at $p \cdot WD = 4.1$ mbar $\cdot$ mm. From $p \cdot WD = 7.2$ mbar $\cdot$ mm onwards, more than 90% of adatoms are thermalized, and the mean energies of the distributions are determined by thermalization. At the highest $p \cdot WD = 13.5$ mbar $\cdot$ mm, the median number of free paths travelled is higher than 2000 and more than 99% of the particles are thermalized, which is in line with findings on sputtering of W [101].

Deposition efficiency develops inversely to thermalization. With a 99% diffusive particle transport, modelled by a random walk of equal directional probability, only slightly more than a fifth of atoms reaches the substrate. Clearly, the exact numbers are dependent on the simulation protocol. Here,
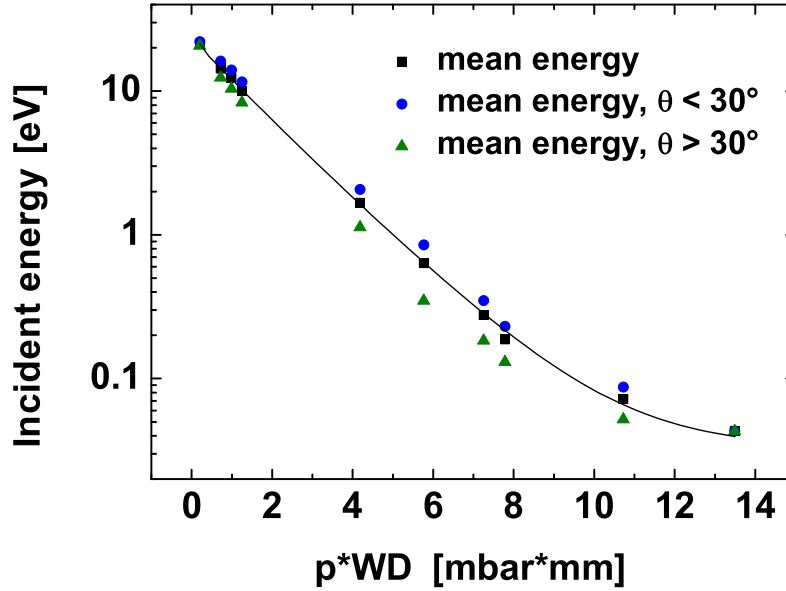
Figure 6.3: Simulated mean incident energies as a function of $p \cdot WD$. The energies are divided into categories depending on the atom's incident angle.

the calculations were turned to the next particle if more than 30000 free paths were travelled without reaching the substrate. However, the use of even higher numbers of free paths did not cause different results.

Compared to the experiments, the number of arrived particles tends to be overestimated. In the simulation, the substrate radius was set to 25 cm, in the experiment, it was 5 cm. However, the substrate holder rotates in the experiment, and deposition occurs onto several substrates, which at least partially compensates for the larger simulated substrate.

As has been shown, the energy distributions of adatoms and their corresponding angular distributions can be altered by tuning the deposition parameters pressure, WD, and power (bias voltage). The effects of altered adatom energies on film growth are presented in the following section, where the discussed transport simulations are input to the simulation of film growth. Furthermore, by adjusting the material parameters, the developed sputter transport simulation can be applied to model the deposition of other elements.
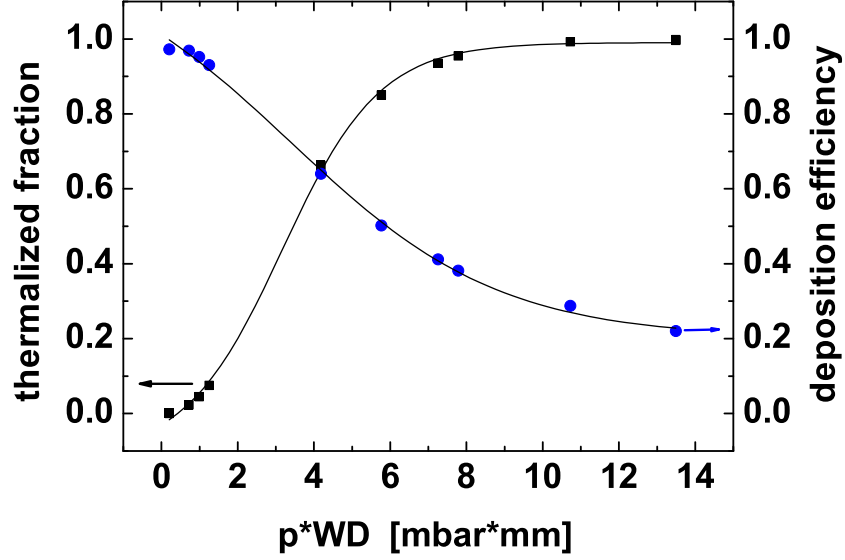
Figure 6.4: Fraction of thermalized atoms diffusing to the substrate and deposition efficiency (arrived over released particles) vs. $p \cdot WD$.

6.2   Simulated Ir film growth

6.2.1   Effects of simulated mechanisms on film growth

Fig. 6.5 illustrates the effects of simulated mechanisms on the growth of Ir thin films. From a) to d), contributing mechanisms described in section 5.2.2 are sequentially added. The simulated morphologies correspond to a 2D view of the cross section of a sample. For each of the simulations, 16000 atoms were deposited onto a substrate 200 atoms wide. Furthermore, for each added mechanism, three simulations are shown corresponding to three different sputter parameter sets.

   The left column corresponds to deposition at $p \cdot WD = 1.2$ mbar $\cdot$ mm at an input power of 180 W, in which case a bias voltage of 385 V develops. The mean impact energy of Ir atoms inserted into the simulation was 10.2 eV (atom transport from target to substrate described in sections 5.1.2 and 6.1.2). The middle column simulates deposition at $p \cdot WD = 4.2$ mbar $\cdot$ mm (P=1000 W, mean incident energy 1.9 eV), and the right column shows deposition at $p \cdot WD = 13.5$ mbar $\cdot$ mm (P=180 W). In this case, more than

E_{inc}=10.2 eV $\qquad$ E_{inc}=1.9 eV $\qquad$ E_{inc}=kT

a) Nearest neighbor relaxation (ρ=0.45)

20 nm

b) Above plus latent heat and thermal spike

c) All above plus diffusion

d) All above plus resputtering

ρ=0.93 $\qquad$ ρ=0.61 $\qquad$ ρ=0.48
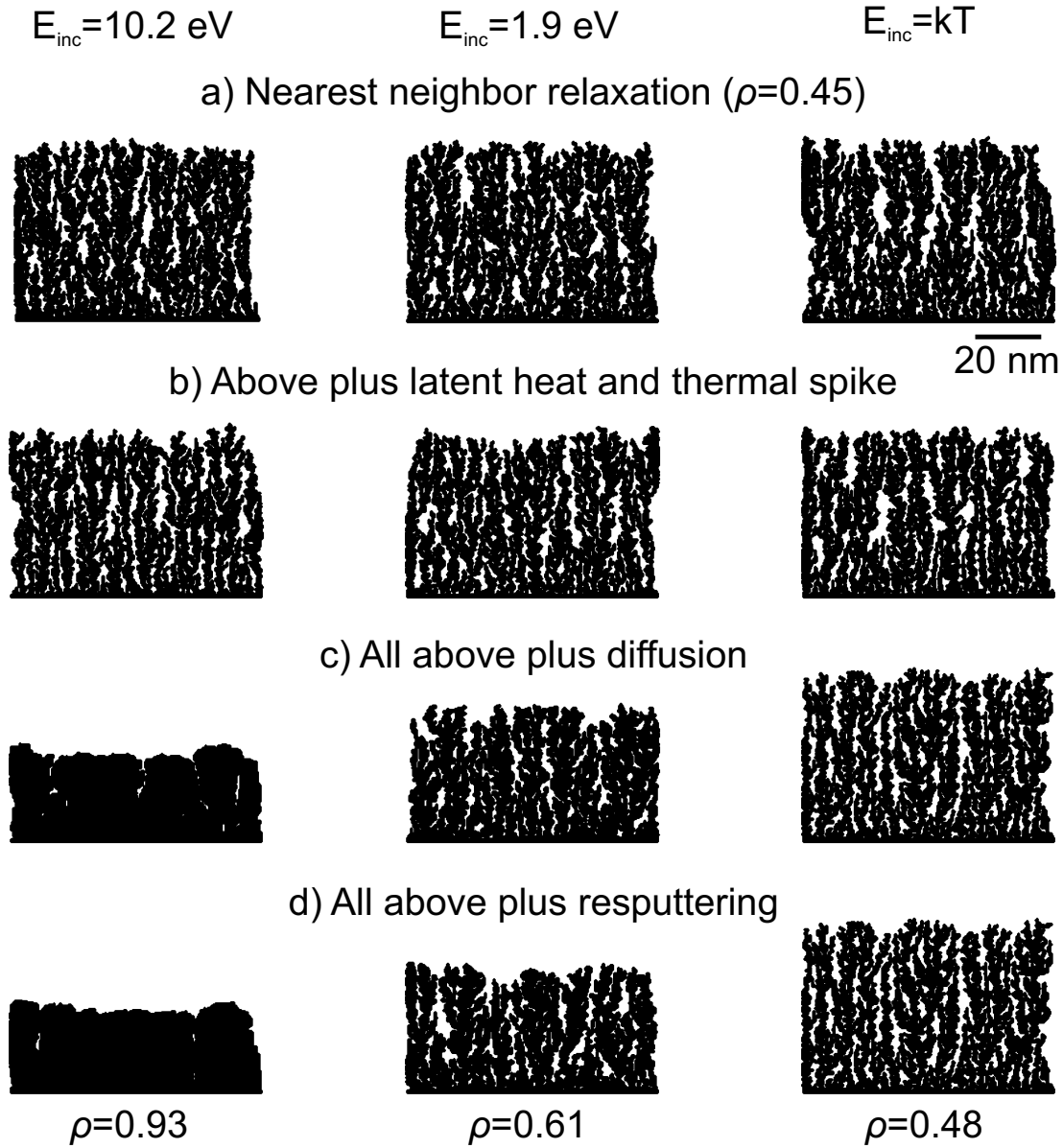
Figure 6.5: Illustration of effects of simulated mechanisms on the growth of Ir thin films. The simulated morphologies correspond to a 2D view of the cross section of a sample. Atoms are represented by discs of size 6 pt. From a) to d), contributing mechanisms are sequentially added. The left hand side simulates deposition at $p \cdot WD = 1.2$ mbar $\cdot$ mm and P=180 W. The middle part corresponds to deposition at $p \cdot WD = 4.2$ mbar $\cdot$ mm and P=1000 W, the right hand side to $p \cdot WD = 13.5$ mbar $\cdot$ mm at P=180 W. The resulting mean incident energies are shown above each column. A scale bar corresponding to 20 nm length is inserted on the top right, as well as initial and final relative densities ρ for all conditions.

99% of incident particles have lost their kinetic energy and diffuse to the substrate. The mean incident energy corresponds to thermal energy kT.

The mean incident angle of deposition lies between 29° and 30° for all conditions (see section 6.1.2 for a discussion of incident atom energies and angles). A scale bar corresponding to 20 nm length is found on the top right of Fig. 6.5, as well as initial and final relative densities ρ for all conditions (see section 5.2.2 for definition of density).

In part a) of Fig. 6.5, an arriving atom is allowed to relax into a nearest-neighbor position. This simulation scheme is independent of energy, and thus, the morphology is the same for all conditions. A fibrous, very rough and porous structure develops, with the relative density ρ=0.45. Certain columns statistically capture angularly distributed flux, and shadow their neighbors. These are subsequently overgrown. This behavior is more often observed close to the substrate, but obviously occurs also at increasing film thickness.

Part b) of Fig. 6.5 adds the effects of thermal spikes resulting from latent heat release and partial dissipation of kinetic energy. In all cases, the relative density increases, however, the effects are rather small. At the highest mean incident energy (left hand side of Fig. 6.5), ρ=0.49, for the other conditions, ρ=0.48. The density increase is accompanied by a decrease in film thickness, at a constant number of deposited particles.

Clearly, kinetic energy-induced diffusion is the most important factor in determining film structure and density. This was also shown by Yang et al. [122] for the low-temperature deposition of Ni. The effects of added diffusion are shown in part c) of Fig. 6.5. At the highest mean incident energies (left hand side), the relative density jumps from 0.49 to 0.91. Averaging over both biased and isotropic diffusion events as well as over diffusion lengths on {111} and {220} crystals, the mean available search length for a site of highest coordination is 12 atom distances from the initial lattice site. Nevertheless, the resulting film structure is still columnar, the columns are broad and separated by open boundaries.

At a mean incident energy of 1.9 eV (middle part), kinetically induced diffusion increases ρ from 0.48 to 0.6. The column widths increase, and the intra- as well as inter-column porosity decreases. Here, the averaged available search length for a new lattice site of the adatom is computed to 4 interatomic distances.

Contrarily, the configurations shown on the right are not affected by diffusion. As more than 99% of all incident particles are thermalized, the simulation only allows relaxation to nearest neighbors, and further diffusion events are seldom executed.

The same argumentation applies to part d) of Fig. 6.5, where resputtering is added to the simulation. Plainly, no resputter event occurs for the low-energy case shown on the right hand side, and thus, the atomic configurations as well as densities are hardly changed from b) to d).

In the case of medium incident energy (middle part), less than 60 resputter events are conducted in 16000 atoms, and the relative density only increases minimally from $\rho=0.6$ to $\rho=0.61$. For high-energy conditions such as shown on the far left, more than 300 resputter events occur, which again increase the relative density from 0.91 to 0.93, however, a fully dense and smooth structure does not develop.

In the final configurations, a higher mean incident energy of adatoms results in higher densities. This is accompanied by a decrease in film thickness, and a broadening of the columns.

Film densities for a number of simulated films are extracted into Fig. 6.6. They are shown as a function of the mean energy of incident particles E_{inc} inserted into the simulation of film growth. Again, the angular and energetic characteristics of the incident atoms are modelled by the transport simulation described in sections 5.1.2 and 6.1.2. E_{inc} is the kinetic energy calculated from the average of all particles taken from a transport simulation and inserted into a simulation of film growth.

Fig. 6.6 includes 20 simulation results. These correspond to films that were actually deposited and are described in the following section. The total number of process conditions within this experimental series was 27, corresponding to the combinations of three DC powers (180, 1000, 2000 W), Ar pressures ($1.6 \cdot 10^{-2}$, $9.3 \cdot 10^{-2}$ and $1.7 \cdot 10^{-1}$ mbar), and working distances (78, 62, 45 mm). However, under high-energy incident conditions such as for low pressure, or high power and small working distance, some films were compressively stressed, peeled off and thus could not be evaluated. Hence, some films are not included in the discussions of experimental results to follow, and their simulated results are omitted from Fig. 6.6.

In any case, one needs to bear in mind that the mean energies E_{inc} displayed in Fig. 6.6 are equivalent to the condensed results of transport simulations of different combinations of bias voltages and pressure-distance products.

Most evaluated mean incident energies are smaller than 1 eV, with some conditions even delivering E_{inc} roughly equal to thermalization ($kT = 0.0428$ eV, see the right column of Fig. 6.5). Under these conditions, the calculated relative densities are smaller than and around 0.5. Only for $E_{inc} > 1$ eV does ρ reach 0.6 and, at the highest energies, values around 0.93 are calculated.

Most of the above discussed effects of included mechanisms are in line with observations made by Yang et al. [122] on nickel deposition, which was
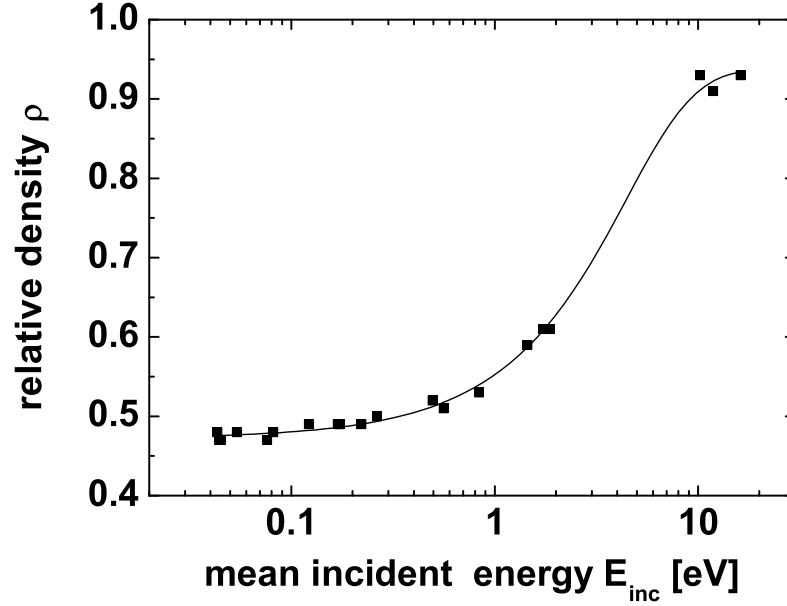
Figure 6.6: Simulated film densities as a function of mean incident atom energies E_{inc} in the simulation. The kinetic energies and impact angles are functions of process conditions and are calculated by the transport model described in sections 5.1.2 and 6.1.2. All displayed simulation results correspond to films that were actually deposited and are described in the following section.

modelled as a function of substrate temperature and kinetic energy of the incident atoms. The authors describe the progressive inclusion of kinetic energy-assisted effects into a deposition model, similar to the above. The general structures of the films modelled at low temperature resemble those described here, with increasing column widths and densities as result of progressively included effects. The final achieved densities are higher in [122], owing to the higher incident energies and additional thermally activated diffusion.

Film densities similar to the ones described here were also reported by Dalla Torre et al. for models of Ta deposition [113]. The densities found for the 0 eV-energy case are slightly higher than what is reported on here, whereas at 10 eV, the densities are congruent. For the low-energy case, the

differences are based on the exclusion of thermally activated diffusion from the model presented here, which is included in [113].

6.2.2 Verification of the model

The simulated film densities were verified by XRR measurements of Ir thin films deposited to thicknesses comparable to the simulated ones (XRR data not shown). At process conditions corresponding to those simulated in the bottom left corner of Fig. 6.5, the film density extracted from the data was 98.5% of the Ir bulk density (uncertainty: 7%). This is in agreement with the density of 93% calculated from the modelled film structure.

XRR measurements on a sample processed under the conditions simulated on the right of Fig. 6.5 delivered a film density of 51% of Ir bulk. Also here, the simulated density of 48% well matches the measurement and is slightly lower. However, it needs to be mentioned that the evaluation of XRR data proved difficult for the underdense film, and an uncertainty of about 20% remained. The differences between measured and simulated densities can be explained by the negligence of thermally activated surface diffusion in the model. Additionally, the lengths of kinetically induced diffusion had to be assumed (see section 6.5 for a discussion of the model).

The similarity to SEM surface images of deposited samples is a further verification of the simulation results. The films shown in Fig. 6.7 are 50-60 nm in thickness. Although slightly thicker than the simulated ones of Fig. 6.5, a comparison is possible. An assessment of cross sections equivalent to the simulated configurations was not possible due to the comparably low SEM resolution. However, the top ends of the modelled cross sections correspond to the surface depicted in the SEM images.

Fig. 6.7a) shows the deposited equivalent to the simulation shown in the left column of Fig. 6.5, a deposition at $p \cdot WD = 1.2$ mbar $\cdot$ mm and $P = 180$ W. The surface is very smooth, and the tops of individual growth columns are hardly resolved. This corresponds to the simulated configuration inset into the image (note the different length scales). There, the top of the simulated cross section forms a largely closed surface, and the individual columns (less than 20 nm in diameter) only slightly protrude.

Fig. 6.7b) shows the surface of an Ir film deposited at $p \cdot WD = 4.2$ mbar $\cdot$ mm and $P{=}1000$ W, and its simulated cross section. The deposited film is characterized by small cusps, which form the tops of the individual growth columns. Between these, small grooves can form due to shadowing effects and the rather low surface mobility. The average column diameter at the surface is 8-10 nm. This is well predicted by the simulation, which shows individual columns of small separation with equivalent widths.
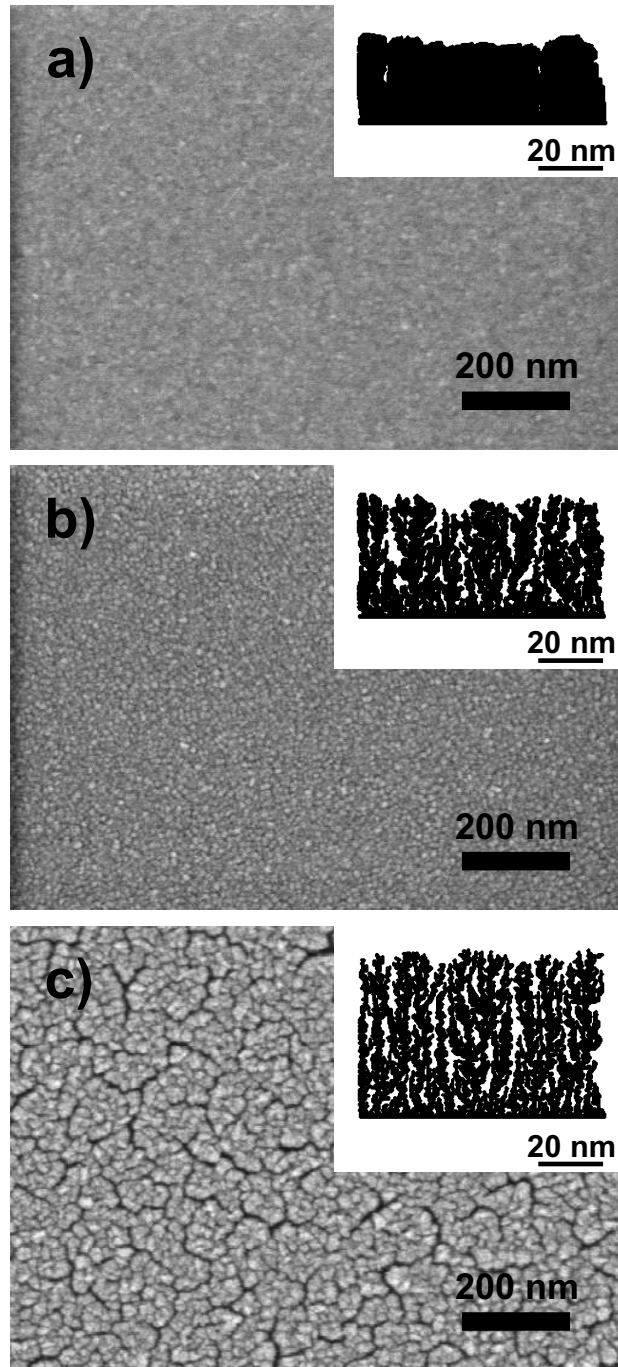
Figure 6.7: SEM surface images of Ir thin films deposited according to the simulated conditions shown in Fig. 6.5. a): deposition at $p \cdot WD = 1.2$ mbar $\cdot$ mm and $P = 180$ W, b): $p \cdot WD = 4.2$ mbar $\cdot$ mm and P=1000 W, c): $p \cdot WD = 13.5$ mbar $\cdot$ mm and P=180 W. Insets show the simulated cross sectional views (note the difference in length scaling).

Finally, part c) of Fig. 6.7 shows a surface SEM image of a film processed at $p \cdot WD = 13.5$ mbar $\cdot$ mm and P=180 W. The surface is strongly structured, caused by shadowing and extremely low adatom mobility. Large grooves separate big growth columns from each other, their diameter being greater than 100 nm. The big columns are composed of smaller columns of diameters around 15 nm, which are again separated by grooves. The latter mentioned smaller columns are depicted in the simulated inset. Both column width and separation correspond to the simulated configuration.

6.3 Electrochemical properties of Ir films

6.3.1 Experimental results: electrochemical activity

This section details the electrochemical characteristics of Ir thin films with different morphologies, realized by altering the three process parameters pressure, power, and working distance. As an example, Fig. 6.8 shows fracture cross section SEM views and CV measurements of two samples deposited at 1000 W DC input power, $WD = 45$ mm and $p = 1.7 \cdot 10^{-1}$ mbar (a), and $p = 1.6 \cdot 10^{-2}$ mbar (b). All SEM images and CV data discussed within this chapter relate to non-activated samples.

For both process conditions, columnar microstructures develop (see section 5.2.1). The columns are separated by large voids in part a) of Fig. 6.8, which shows the sample deposited at high pressure. The underdense structure is caused by shadowing, which can not be compensated for by diffusion due to low adatom mobility, and represents a typical zone I microstructure [85]. A rough surface develops. In part b) of Fig. 6.8, the columns are denser and the inter-columnar spacing is smaller. Due to a higher incident energy, a higher adatom mobility is provided for which can compensate shadowing and enables densification. Here, the columns are topped by smooth caps. One might argue whether the film represents a transition zone deposit, characterized by less open boundaries, or whether it still can be considered a zone I structure.

The film configuration influences the number of surface atoms available for charge injection during electrochemical experiments. This is illustrated by the CV data reproduced in Fig. 6.8. At an unaltered chemical composition, and not influenced by the effects of activation into the films, an increased specific surface increases the injected charge. The sample deposited at higher pressure delivers more than 30-fold higher current densities. As the comparison of model and experiment will show, the increase is directly determined by film atoms that are parts of free surfaces.
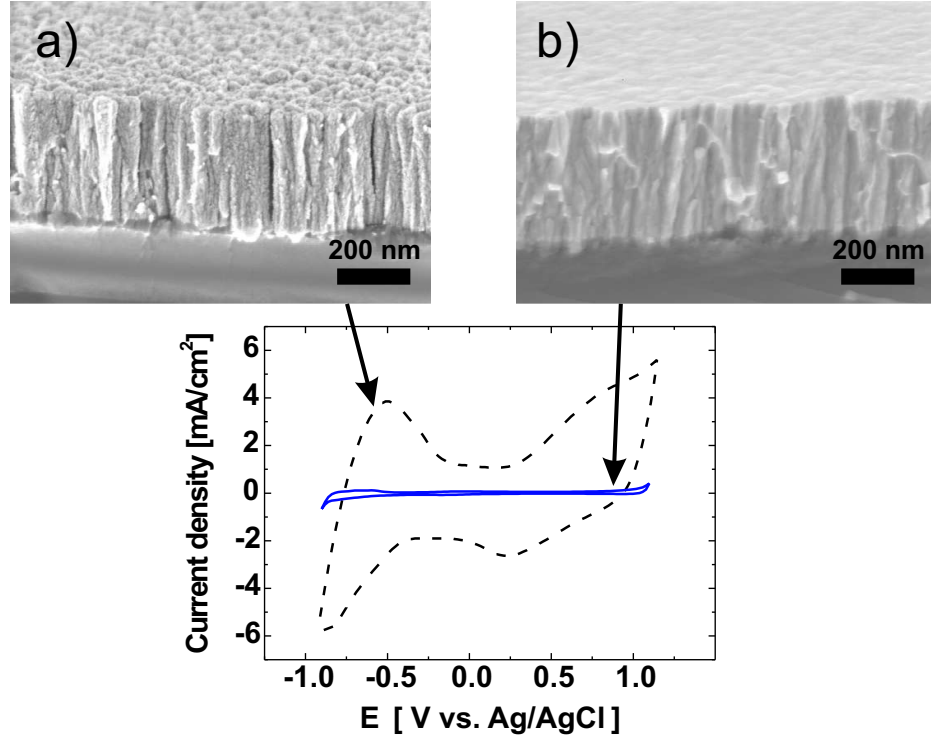
Figure 6.8: SEM fracture cross sections of Ir thin films deposited at $P = 1000$ W DC, $WD = 45$ mm and a) $p = 1.7 \cdot 10^{-1}$ mbar, b) $p = 1.6 \cdot 10^{-2}$ mbar. Bottom: cyclic voltammograms of the two films, not activated by repeated potential cycling.

The above demonstrates that the control of growth kinetics by the choice of deposition parameters (in this case, only sputter pressure) has direct and measurable influence on Ir thin film electrode characteristics. The principle can be expanded to all sputter parameters considered in this section. Fig. 6.9 shows the anodic charge delivery Q_a of 20 films as a function of $p \cdot WD$ and bias voltage V_b. Again, V_b develops as a function of input power, and is chosen as the axis parameter to allow comparison with the simulation.[2]

For Fig. 6.9, Q_a is extracted without prior repeated potential cycling. This way, the influence of activation on film characteristics is excluded, and the delivered charge can be assumed to be solely determined by the atoms that are directly accessible for the electrolyte. This not only includes redox centers on the film surface, but explicitly also those within channels that

---

[2]In the following, the discussed electrochemical data is limited to CV results. Impedance measurements are congruent, but do not allow to draw further conclusions.
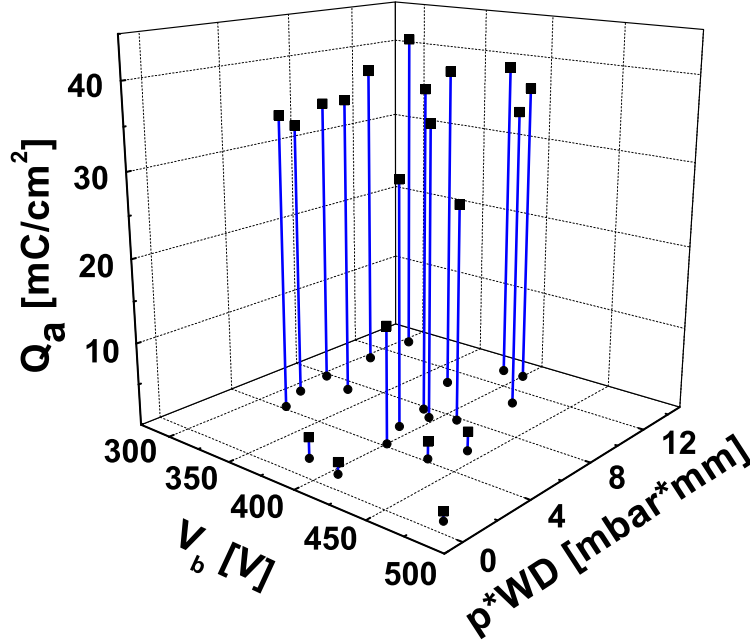
Figure 6.9: Anodic charge delivery Q_a (extracted without prior potential cycling) as a function of the deposition process parameters $p \cdot WD$ and bias voltage V_b. The latter is a function of input power. Anchor lines and projection points illustrate the parameter combination of V_b and $p \cdot WD$.

are connected with the surface. A comparison with simulated films is then possible (see the following section). Furthermore, as detailed in section 2.2.1, the contribution of gas evolution to electrode current (see Fig. 6.8 for an example of gas evolution peaks at high negative potentials) is subtracted when calculating the anodic charge delivery Q_a. Additionally, all films were deposited to thicknesses around 350 nm in order to ensure comparability (see section 7.2 for notes on the influence of film thickness).

The general trends and dependencies are straightforward to develop from Fig. 6.9. An increasing pressure-distance product and a decreasing bias voltage lead to less energetic adatom conditions, which results in higher specific surfaces and more electroactive films. Consequently, the highest charge delivery of 41 mC/cm² develops at 305 V and 13.5 mbar · mm. On the opposite

end of the parameter set (corresponding to the front corner of the graph), at 480 V and 0.7 mbar $\cdot$ mm, 1.1 mC/cm^2 are measured.

Fig. 6.9 also underlines that similar results can be achieved by a number of different parameter combinations. On 11 films, Q_a amounts to between 30 and 40 mC/cm^2, which is a respectable value. These values are reached either by combinations of high $p \cdot WD$ and medium V_b (e. g. 10.7 mbar $\cdot$ mm, 370 V) or medium $p \cdot WD$ and low V_b (5.7 mbar $\cdot$ mm, 310 V).

Furthermore, Fig. 6.9 stresses the importance of single input parameters. For example, at bias voltages around 400 V, the increase of $p \cdot WD$ alone effectuates an increase in Q_a from 1.4 to 37 mC/cm^2. Congruently, a decrease in bias voltage (via input power) at $p \cdot WD = 4.2$ mbar $\cdot$ mm results in an increase in charge delivery from 2 to 35 mC/cm^2.

Compared to results achieved during the reactive sputtering of IrOx (chapters 3 and 4), the highest anodic charge deliveries measured on metallic Ir within this section are roughly half as high those measured at optimized reactive gas flow. The combined effects of optimized incident energetic conditions and reactive sputtering are presented in section 7.1.

The interpretation of Fig. 6.9 can be further simplified by making use of transport simulations. They allow to condense the process parameters $p \cdot WD$ and V_b into one single input, the mean incident energy E_{inc}. The results are shown in the next section, together with a comparison of experiment and simulation.

6.3.2   Comparison of model and experiment: electro-chemical activity

Fig. 6.10 shows the measured anodic charge delivery capacity Q_a as a function of the simulated mean incident energy of adatoms E_{inc}. Q_a was described as a function of V_b and $p \cdot WD$ in the preceding section. Here, these parameters are combined into a single parameter E_{inc}, an output of transport simulations.

As an essential result, the development of measured Q_a over simulated E_{inc} follows a clear trend. As discussed in the preceding sections, a higher incident adatom energy leads to higher surface mobility. Shadowing effects can be compensated by diffusion, and the growing film is densified. In the measurement, this results in a smaller number of film atoms contributing to charge transfer across the electrode-electrolyte boundary.

At this point, the importance of distributed angular incidence needs to be pointed out. Although the highest charge deliveries are reached on films deposited at low-energy conditions, thermal evaporation of Ir would not deliver comparable films. Commonly, evaporation proceeds under ultra-high vac-
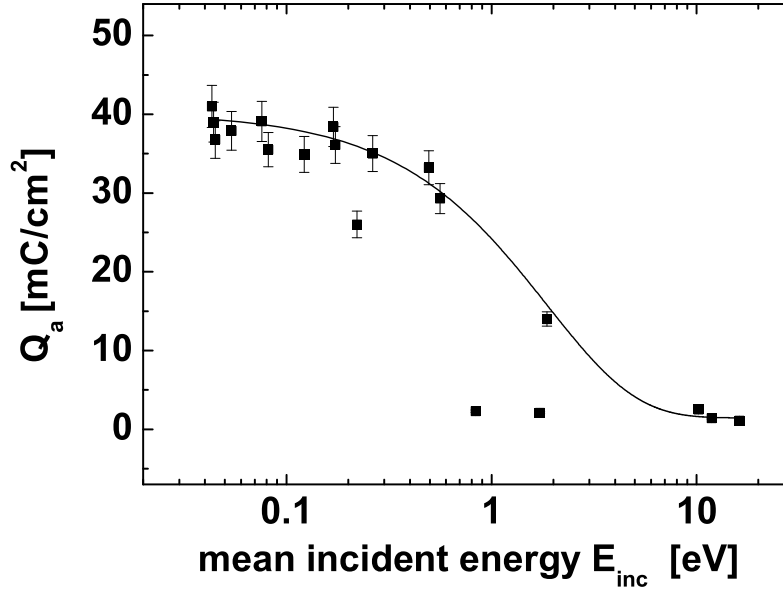
Figure 6.10: Measured anodic charge delivery capacity Q_a (extracted without prior potential cycling) as a function of the average kinetic energy of adatoms inserted into the respective simulation. The characteristics of atoms inserted into the growth model are output of the transport simulations described in sections 5.1.2 and 6.1. The process conditions for simulations and experiments correspond to those shown in Fig. 6.9.

uum, resulting in line-of-sight incidence. Under these conditions, shadowing effects are ruled out. Furthermore, thermal evaporation does not allow the reactive deposition of IrOx, as shown in chapters 3, 4 and 7.

Fig. 6.10 contains three distinct outliers. In these cases, the measured anodic charge delivery is lower than the expected value indicated by the data fit. All three films were deposited at the highest input power of 2000 W and medium $p \cdot WD$. At lower $p \cdot WD$, as mentioned before, the films could not be evaluated due to high compressive stresses and peeling. At higher $p \cdot WD$, the films deposited at 2000 W agree with the fit.

A possible explanation for the disagreement between fit and the three data points is the negligence of plasma particle flux in the approach at hand. E_{inc} only represents the energy input by the deposited Ir particles as such.

However, at a high power, the plasma expands further from the target, and the substrate can be reached by both high-energy reflected Ar neutrals as well as by medium-energy Ar ions. They can cause atom rearrangement directly by way of impact or indirectly through an increasing substrate temperature [86]. The additional energy input results in further film densification [112]. The low target-substrate distances used in the three experiments in question (45, 45, and 62 mm) underline this supposition.

As has been discussed, Fig. 6.10 includes measurement results as a function of transport simulation output. In the following, the view is expanded to the evaluation of simulated film growth with respect to electrochemical activity. The comparison of experimental film data and modelled film morphology is based on the following prerequisites:

- All pores and voids visible in simulated 2D cross sections are connected to the surface via channels (see figs. 6.5 and 6.7).

- The accessibility by the electrolyte and the availability for charge transfer reactions of a single atom depend on its location relative to surrounding atoms within the film.

The latter is illustrated in Fig. 6.11, which shows an exemplary close-up of a simulated cross section showing all theoretically possible configurations. The digits 1 to 8 are the numbers of near neighbors of the labelled atom. It is assumed that upon application of electrolyte from the top, and application of voltage to the film, an atom of position label $P = 8$ does not contribute to electrochemical currents. It cannot be reached by the electrolyte. This mimics the experimental CV measurements, which are evaluated within the first potential cycles. The procedure ensures that the measured current is contributed only by the top layer of atoms, and precludes the effects of activation and current contribution of deeper parts of the film (see section 4.4).

On the contrary, all other labelled atoms of Fig. 6.11 can contribute to electrochemical currents, however, geometric reasoning precludes the assumption of equal accessibility by the electrolyte. Thus, the immediate environment is taken into account. The parameter A_t is introduced to express if and how easily an atom is accessible and available for charge transfer. It is computed by $A_t = |P - 8|$, where P is the position label shown in Fig. 6.11. For a whole film, $A_{t,m}$ represents the mean availability and accessibility of the film atoms for charge transfer reactions, $A_{t,m} = \frac{\sum_{i=1}^{N} A_{t,i}}{N}$, where N is the number of atoms in the film.

All depositions discussed in Fig. 6.10 were simulated, and $A_{t,m}$ was calculated according to the procedure described above. The results are shown in

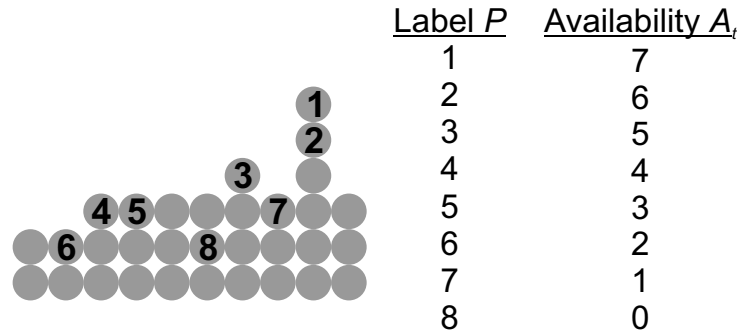| Label P	Availability A_t
1	7
2	6
3	5
4	4
5	3
6	2
7	1
8	0

Figure 6.11: Exemplary atomic configuration illustrating the calculation of the contribution of an atom to electrochemical currents. The digits 1 to 8 denote the number of atoms within the immediate neighborhood of the labelled atom. All theoretically possible arrangements are shown. An atom of position label $P = 8$ is assumed to have zero contribution to electrochemical currents upon voltage application. It cannot be reached by the electrolyte, which is applied from the top (bearing in mind that the corresponding CV measurements were evaluated within the first cycles, not allowing the electrolyte to oxidize deeper layers of Ir.) In general terms, the parameter A_t expresses if and how easily an atom is accessible and available for charge transfer. It is computed by $A_t = |P - 8|$, where P is the position label. This is shown in the accompanying table.

Fig. 6.12 as a function of mean incident atom energy (round symbols). Furthermore, the experimentally retrieved charge deliveries Q_a from Fig. 6.10 are included (square symbols). The three outliers discussed in the preceding are excluded.

The graph can be read as follows. Under certain deposition conditions, and thus a certain mean incident energy, the model predicts an average atomic configuration. For example, at low mean incident energies, $A_{t,m}$ is close to 2. Referring to Fig. 6.11, this corresponds to an average positional configuration P of roughly 6. Hence, in these films, only 6 of 8 available near-neighbor sites are occupied. In turn, the measured electrochemical activity of the film Q_a is high.

With increasing incident energy, $A_{t,m}$ slowly decreases, conformal with increasingly tight packing and higher average positional configurations P. As a result, the measured electrochemical activity also decreases. Notably, the decrease is almost congruent. At the highest incident energies, $A_{t,m} < 0.2$, corresponding to an average positional configuration close to the maximum of 8. The average film atom is surrounded by neighbors, the films are densely
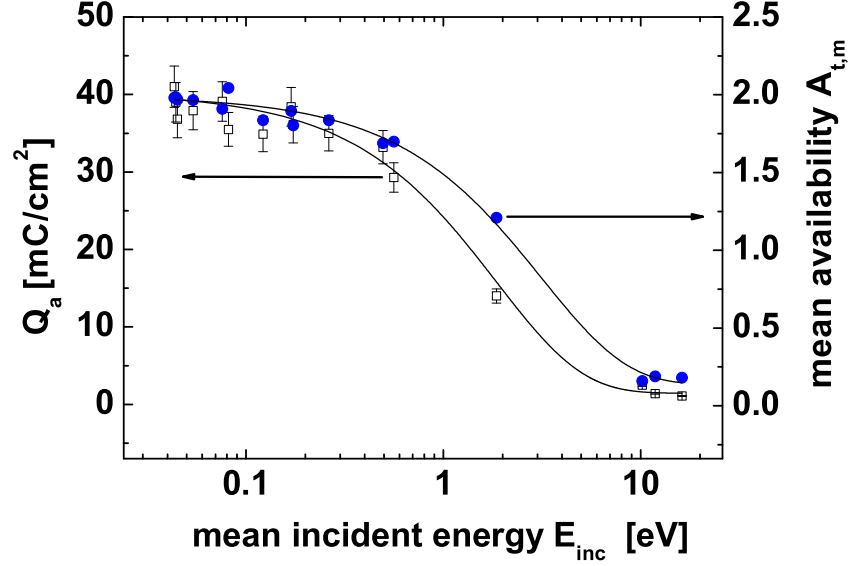
Figure 6.12: Measured anodic charge delivery capacity Q_a (extracted without prior potential cycling) as function of simulated mean incident energy of adatoms (square symbols, see also Fig. 6.10). Round symbols: mean availability and accessibility of simulated film atoms for charge transfer reactions (refer to Fig. 6.11 for calculation procedure).

packed. Only the final deposited layer, i. e., the surface atoms in their very sense, contribute to electrochemical response. As a result, the anodic charge delivery Q_a reaches its minimum. Simulated cross sections and SEM surface and cross-sectional views of corresponding films were shown in figs. 6.8b) and 6.7a).

Comparing the curve shapes, the simulation and its evaluation well describe the dependence of electrochemical activity on adatom energy. The quantitative deviations between measurement and simulation are based on several uncertainties. Note that the proposed evaluation by itself strongly simplifies the complex diffusion and charge exchange mechanisms between an electrode and an electrolyte. Further uncertainty is added by the deviations between simulated and experimental film growth (see section 6.2.2). In any case, in its simplicity, the evaluation of simulated 2D cross sections underlines the importance of open surfaces for electrode performance.

Generally speaking, the film growth model returns a statement regarding an average atomic configuration, which scales well with electrochemical measurements in 3D reality. The model explains the differences in anodically delivered charge Q_a of the deposited films on grounds of accessibility of film atoms. Model output and measurement are alike functions of mean kinetic energy of incident atoms. The simulation allows to predict the electrochemical behavior of a deposited film by scaling with the results shown above.

6.4 Crystallographic orientation of Ir films

6.4.1 Experimental results: texture

A number of authors have described the influence of adatom and bombarding ion energies on texture of (reactively) sputtered films (mainly transition metal nitrides, [112, 118, 135, 147, 148], and references therein). Comparable investigations for Ir are not available. This section introduces and discusses the effects of incident atom energy on preferred crystallographic orientation of Ir thin films. The results are strongly tied to those regarding the electrochemical activity of Ir films discussed in the foregoing.

The investigated Ir thin films are polycrystalline, and three major crystallographic orientations are found, the {111}, {220}, and {200} families. However, only the peak intensity ratios of {111} and {220} are affected notably by the choice of parameter conditions. Hence, the following discussion focusses on these, as does the simulation, which only considers the two orientations.[3]

The evaluation of experimental data is limited to the calculation of peak intensity ratios. By comparison with the peak intensity ratio of an untextured powder sample, qualitative conclusions regarding the preferred orientation of the samples can be drawn.

The preferred orientation of sputtered Ir samples is a strong function of sputter parameters. This is illustrated in Fig. 6.13, showing two sets of detected intensities as function of x-ray incidence angle 2θ. Data set a) is from a sample sputtered at $WD = 78$ mm, $P = 180$ W, and $p = 1.6 \cdot 10^{-2}$ mbar, corresponding to a simulated mean incident energy E_{inc} of 10.2 eV. Data set b) is retrieved from a sample processed at $WD = 78$ mm, $P = 1000$ W, and $p = 9.3 \cdot 10^{-2}$ mbar ($E_{inc} = 0.2$ eV). The maximum peak heights were normed to the same value, the detected crystal planes are indicated.

---

[3]The thin Ti adhesion layer deposited prior to Ir was not found to have an influence on crystallographic orientation.
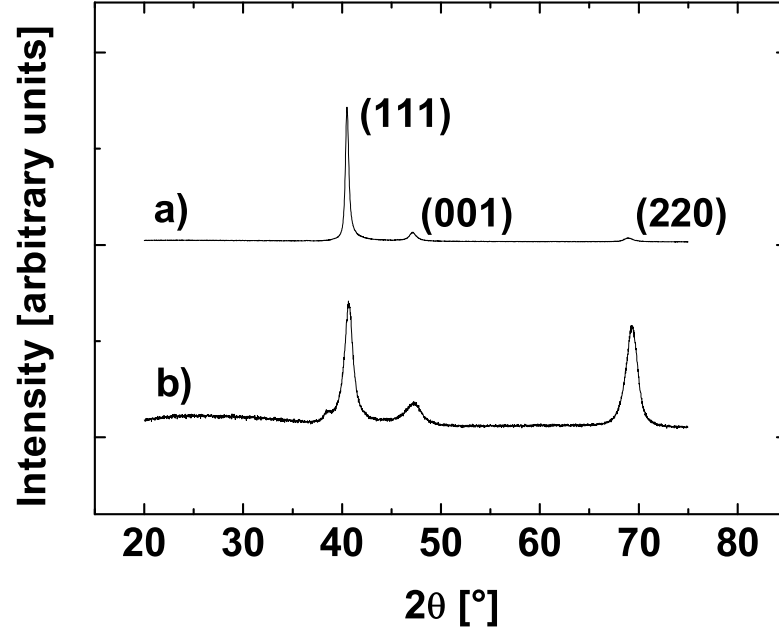
Figure 6.13: XRD data of Ir films sputtered under different conditions. a): $WD = 78$ mm, $P = 180$ W, $p = 1.6 \cdot 10^{-2}$ mbar. b): $WD = 78$ mm, $P = 1000$ W, and $p = 9.3 \cdot 10^{-2}$ mbar. The detected crystal planes are indicated.

Both investigated samples comprise equivalent crystal planes, however, the relative size of the peaks has changed. For data set a), the intensity ratio $R_I = I_{111}/I_{220} = 38$. The corresponding peak intensity ratio of an untextured powder sample is 4.38, which implies a strong {111} texture of the thin film.[4] For Fig. 6.13b), the measured ratio is 1.2, meaning a {220}-preferred orientation.

Just as in the case of electrochemical activities, these differences can only be explained on grounds of differences in incident atom energies [112, 118, 135, 148].

The potential energy of an adatom depends on the crystallographic orientation it is placed onto. Correspondingly, the barrier for diffusion increases or decreases. On a high-energy face such as {111}, the adatoms are likely

_____

[4]Inorganic Crystal Structure Database, ICSD.

to diffuse quickly to a cluster edge, and expand the cluster in a lateral way. On faces of lower adatom potential energy, such as {220} for Ir, diffusion is limited and hence, growth proceeds in the vertical direction. Because of their developing height advantage and the resulting shadowing, they intercept more particle flux, which results in even faster growth.

At extremely low adatom mobilities, and under angular incidence, {220} grains can overgrow {111} faces. Under these conditions, columns preserve the random orientation of initial nuclei [112]. This will be further illustrated in the following section, presenting simulations of texture development.

With increasing adatom mobility, adatoms on {111} can diffuse even farther. They stick preferentially at edges of clusters, resulting in larger islands. The increased mobility also enhances adatom diffusion on and away from {220} faces. This implies that compared to the low-diffusivity case, {220} grains are more likely to loose material in the region of grain boundaries. This explains the tendency towards stronger {111} texture at higher incident energies.

Further thin films representing a variety of process conditions discussed in the preceding section were evaluated by means of XRD. Following the procedure shown and verified in the preceding section, the ratios of peak intensities can be presented as a function of simulated mean incident energies for the evaluated process conditions. Fig. 6.14 shows the intensity ratio $R_I = I_{111}/I_{220}$ as a function of E_{inc}. Included is a horizontal line representing $R_I = 4.38$ for untextured powder samples.

The graph can be read as follows. Data points below the horizontal line indicate preferred {220} orientation of the thin films. This is the case for all samples deposited by processes delivering low incident atom energies, although the textures are not strongly developed. Only four of the evaluated thin films exhibit more or less developed {111} texture, exclusively at higher incident energies of adatoms. This is explained by the available theory discussed above.

The two outliers at $E_{inc} = 0.8$ and 1.7 eV in Fig. 6.14 are measurements on two of the three thin films discussed as outliers in Fig. 6.10. There, the fit predicted a higher charge delivery capacity. Here, a lower R_I is expected. The behavior is fully in line with the explanation presented earlier. The high input power and small target-substrate distance used in processing the two films lead to enhanced energetic bombardment by plasma species. The films thus receive a higher energy flux than predicted by merely accounting for the adatoms' incident energies, as done in Fig. 6.14. The additional energy supply leads to a higher diffusivity and further rearrangement of atoms, favoring both {111} orientation as well as densification.
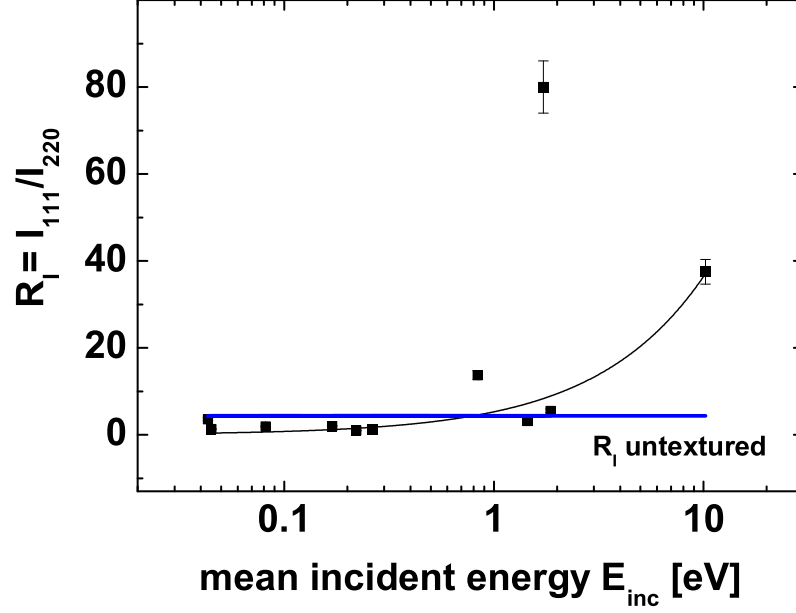
Figure 6.14: Measured intensity ratio $R_I = I_{111}/I_{220}$ of Ir thin films as a function of simulated mean incident energy in the deposition process. The horizontal line indicates $R_I = 4.38$ for untextured powder samples.

The general development of R_I over adatom energy inversely correlates with the development of the electrochemical activity. A lower adatom mobility favors growth of {220} grains, at the expense of {111} orientation. {220} grains tend to grow higher and are responsible for stronger shadowing, leading to the development of rough, voided and underdense films, which again is supported by low adatom mobility. As a result, in these cases, specific surface and accordingly the electrochemical activity increase.

The results are in line with simulations regarding the texture-dependent density of Al and the resistance towards interconnect material diffusion [135]. Films of {111} orientation were shown to have higher densities than those oriented with low-mobility planes, where large voids span the whole film thickness. On {111}-oriented films, a higher diffusivity of adatoms and thus stronger lateral spreading develop a denser film with fewer channels.

6.4.2 Comparison of model and experiment: texture

As to the simulated texture development, the trends developed experimentally are well predicted. Two exemplary configurations are shown in Fig. 6.15. Part a) shows growth upon low-mobility incidence (mean kinetic energy close to thermalization), part b) simulated growth at a mean incident energy of 10.2 eV. {111}-oriented crystals are shown in black, {220} in grey, and the substrate in darker grey.
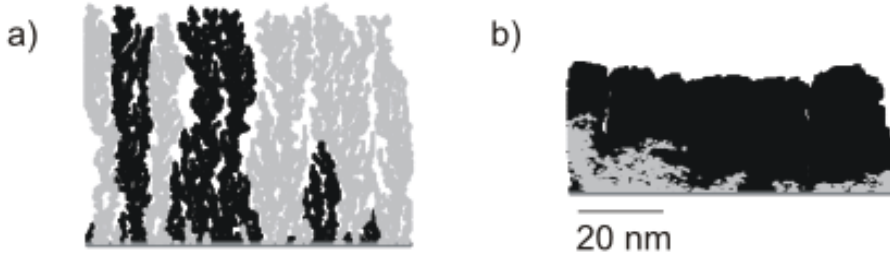
Figure 6.15: Simulated film configurations evaluated for crystallographic texture. a) incidence at a mean energy $E_{inc} = 0.2$ eV, b) $E_{inc} = 10.2$ eV. {111}-oriented crystals are shown in black, {220} in grey, and the substrate in darker grey.

In Fig. 6.15a), the random nature of simulated texture development at low incident energies becomes apparent. The average diffusivity being negligible, the atoms are assigned random orientations on the substrate. From there, the columns expand rather vertically than laterally, and columns will overgrow their neighbors. This occurs in a random manner, and is independent of orientation (recall that atoms are assigned the orientation of the crystal they impinge onto). Because exchange between columns is nearly impossible due to small diffusion lengths, the growth proceeds within one type of orientation.

In Fig. 6.15b), longer diffusion paths cause a strong overweight of {111}-oriented grains. In this case, and again randomly, {220} seeds overweigh directly on the substrate. However, the few initial {111} islands expand faster laterally and eventually overgrow the {220} grains. On the very surface, the film is completely {111}-oriented. Longer diffusion paths also make atom exchange between orientations possible (seen as grey dots in the black {111} grain).

Comparison between measurement and simulation is only possible in a qualitative way. The theoretical intensities of diffraction at lattice planes are not only determined by the number of oriented grains. Other factors include

polarization and absorption at the lattice planes in question. Hence, texture is related to the number of atoms within one orientation, but not determined by it. In this respect, the comparison is based on measured $R_I = I_{111}/I_{220}$ and simulated $R_N = N_{111}/N_{220}$. R_N represents the ratio of numbers of atoms N within the orientations.

Fig. 6.16 includes both measured R_I as well as simulated R_N as a function of simulated mean incident energy. The two outliers described in Fig. 6.14 are omitted.
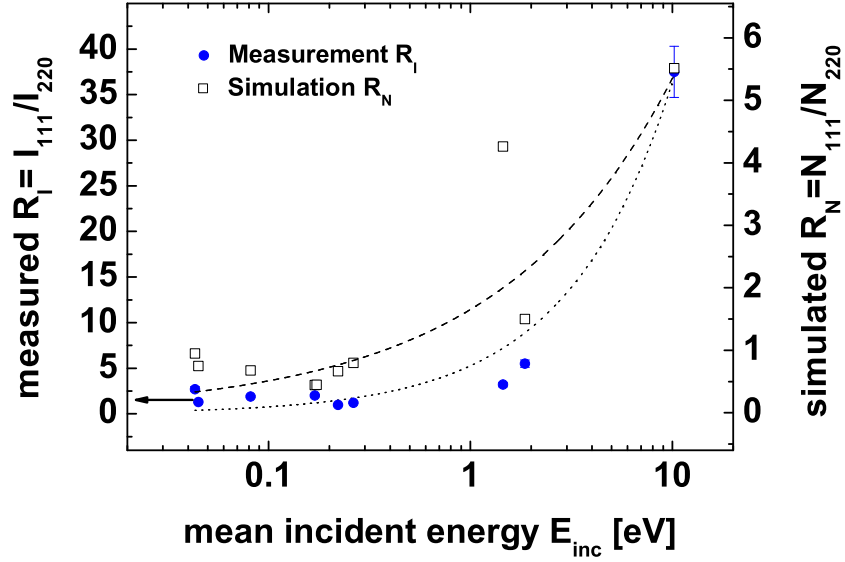
Figure 6.16: Measured peak intensity ratio $R_I = I_{111}/I_{220}$ (round symbols and dotted fit) and simulated orientation ratio $R_N = N_{111}/N_{220}$ (square, open symbols and dashed fit) as a function of simulated mean incident energy in the deposition process.

The interpretation of simulated orientations is limited due to the above discussed reasons. However, it becomes clear that the measured trends are well predicted.

At the low-energy end of the scale, both experimental and simulated ratios are not greatly affected by incident energy. The development of texture in the simulation is random, as shown in Fig. 6.15a). R_N equals 1 for a sufficiently wide substrate and a large number of simulated atoms.

Increasing the energy, average diffusion lengths on the two considered orientations slowly start to differ. Recalling the simulation policies of section 5.2.2, the maximum diffusion lengths on {220} are shorter than those on {111}. For $E_{inc} = 10.2$ eV, the average diffusion length on {111} is roughly twice as high as on {220}. As illustrated in Fig. 6.15b), this leads to a higher $R_N = N_{111}/N_{220}$.

Hence, in total, the simulation can qualitatively reproduce and predict the general development of texture. The model can gain precision using a wider substrate and a higher number of simulated atoms.

6.5   Comments on the film growth model

The presented simulator models and predicts the evolution of Ir thin film microstructure in dependence of adatom energy and angular distributions. It is one of only a few published approaches modelling the effects of kinetic energy of incident atoms on the structure of a sputtered film [113,122,124,138]. Compared to the works of Yang et al. and Liu et al. [122–124], the presented approach is more simplified. Their works were based on MD calculations that delivered analytical expressions describing in detail the included effects such as resputtering or biased diffusion. Thermally activated diffusion and deposition rate effects were included as further parameters in the simulations. However, the works did not compare simulations to experimental data, and no analysis of texture development was presented. Similarly, the simulations of Torre et al. [113] contained more detail regarding atomistic effects activated by kinetic energy and temperature. Again, few detail on comparison to experiment was presented, apart from film density evaluations. Smy et al. [138] only incorporated biased diffusion effects, and disregarded resputtering or latent heat release. Nevertheless, the approach allowed to explain morphological features seen in SEM images.

The presented simulation shows that incident kinetic energy and shadowing effects alone are of enormous importance for the evolution of Ir film microstructure, and explanations for the underlying mechanisms were given. Although based on simple assumptions, the 2D model is able to predict and explain film properties such as film density and morphology (Fig. 6.7). Furthermore, electrochemical data can be approximated from the modelled configurations, although evaluated in a simple manner (Fig. 6.12). Also the development of crystallographic orientation is concurrent with the measured trends, as shown in Fig. 6.16.

The simulation well describes and predicts the results for the parameter sets discussed within this chapter, and can also be applied to simulate deposition over topographies.

As to its limits, in its current stage, the influence of thermally activated diffusion on film growth is not included. Furthermore, as time is disregarded in the simulation, the effects of very high deposition rates on microstructure can not be modelled (above 5-10 μm/min [117–119]). However, the model can be extended to address the above points.

Regarding the energy flux to the substrate, the results and predicted trends were shown valid over a wide range of mean incident kinetic energies of the adatoms (around 12 eV to thermalization). However, the model does not account for effects of energetic plasma particles bombarding the substrate. This, as the results showed, can become important at high sputter powers and small target-substrate distances, and sputtering at lower pressures, but also for RF sputtering.

The modelled densities are lower than their measured counterparts. Apart from the above described effects of energetic plasma particle flux to the substrate [113], this can be explained by the negligence of thermally activated surface diffusion, which does occur at the experimental substrate temperatures. Furthermore, the extent of kinetically induced diffusion had to be assumed. Tentatively, diffusion on {111}-faces at low energies is underestimated; at $E_{inc} < 1$ eV, the model does not differentiate between crystallographic orientations, and diffusion is limited to a move to nearest-neighbor sites. Contrarily, the kinetic energy-induced isotropic diffusion may be overestimated for large incident energies.

6.6   Summary

It was shown for the first time that energy and angular distributions of incident atoms decisively influence the microstructure of sputtered metallic Ir thin films. Distinct morphologies were generated by altering the process parameters power (bias voltage), pressure and target-substrate-distance.

Monte Carlo simulations of the transport of sputtered Ir particles through the gas phase showed that the average incident angles measured from the substrate normal do not change considerably upon alteration of process parameters. Geometrical shadowing during growth occurred for all investigated conditions, with great importance for the development of open structures.

The average atom arriving at smaller angles had a higher energy than its counterpart arriving at larger angles. At pressure-distance products around 1 mbar·mm, the mean incident energies were greater than 10 eV. At the

highest pressure-distance product investigated ($p \cdot WD = 13.5$ mbar $\cdot$ mm), more than 99% of the particles were thermalized.

The calculated adatom energies and angles were used as input for a model of film growth. The presented 2D model is the first of its kind developed for Ir. It is one of only a few explaining and predicting film evolution on the atomic scale as a function of the kinetic energy of adatoms. Of the mechanisms included in the model, kinetic energy-induced diffusion was the most important factor in determining film characteristics. The simulated densities and structures were in line with XRR measurements and SEM images of deposited thin films. Furthermore, also the evaluation of electrochemical activity and development of crystallographic orientation scaled well with measurements in 3D reality.

As to electrochemical activity of Ir thin films, an increasing pressure-distance product and a decreasing bias voltage lead to less energetic adatom conditions, which resulted in higher specific surfaces and more electroactive films. Choosing the appropriate sets of parameters, the anodically delivered charge was increased by a factor of roughly 37, merely determined by film morphology.

The film growth model explained the increase in anodically delivered charge on grounds of accessibility of film atoms by electrolyte. The measurements and model outputs, which can be regarded as an indicator of average site occupation in a film, were alike functions of mean adatom energy.

Most evaluated films were weakly {220}-oriented. With an increasing incident energy and thus surface mobility of the adatoms, texture changed to {111} orientation.

The development of preferred {111} orientation over adatom kinetic energy inversely correlated with the development of electrochemical activity. Films containing considerable {220} contribution were rougher, with lower densities and stronger void formation. In these cases, specific surface and accordingly the electrochemical activity increased.

The experimentally observed trends were predicted qualitatively by the simulated development of crystallographic orientation. At low incident energies, the development of texture in the simulation was random. At an increased incident energy of adatoms, the average diffusion lengths on {111} crystals increased, and {111} crystals overgrew {220} grains.

Chapter 7

Increased Electrochemical Activity

This chapter presents approaches to further increase the electrochemical activity of Ir and IrOx thin films, based on the experiments and simulations presented in the foregoing chapters. The first section details the combination of effects of low Ir adatom mobility and those of reactive sputtering. The second section illustrates the enhancement of shadowing effects in order to create higher specific surfaces.

7.1 Combination of low mobility and reactive sputtering

In this section, a metal process delivering low adatom mobility is combined with reactive gas flow to the sputter chamber. Similar investigations were performed in chapters 3 and 4, however, the starting metal processes were not optimized for shadowing and low adatom mobility. The corresponding transport simulations showed that the mean incident kinetic energies were around 6-7 eV. Consequently, they delivered smooth and electrochemically rather inactive thin films (Q_a=7 mC/cm² after 100 cycles of activation in chapter 3). Upon inclusion of optimized reactive gas flow, the anodically delivered charge increased by factors of more than 11 (Fig. 3.8 on page 31).

This section discusses whether the addition of oxygen to an optimized metal process brings about similar increases in electrochemical activity, or whether a limit in charge delivery has been reached.

The starting set of process parameters for metal deposition was chosen as 1000 W DC, $WD = 78$ mm and $p = 9.3 \cdot 10^{-2}$ mbar. The anodic charge delivery Q_a of the deposited Ir sample was measured to 35 mC/cm² before ac-

tivation. In the corresponding simulations of sputter transport, the adatoms arrive at a mean incident energy of 0.2 eV. As to simulated film growth, the average search length for a new lattice site during diffusion calculates to 2.4 interatomic distances.

The reactive sputtering is optimized according to the procedure described in chapters 3 and 4. Oxygen integration, deposition rate, and electrochemical activity as functions of oxygen supply follow the patterns discussed earlier, and are not shown here. The following discussion focusses on samples deposited at high oxygen integration, and the comparison to their metallic counterparts.

Fig. 7.1 shows the surface SEM images of a reactively sputtered sample (a) and its metallic counterpart (b). The CV measurements after 100-fold potential cycling are included. The IrOx film shown in Fig. 7.1a) was sput-

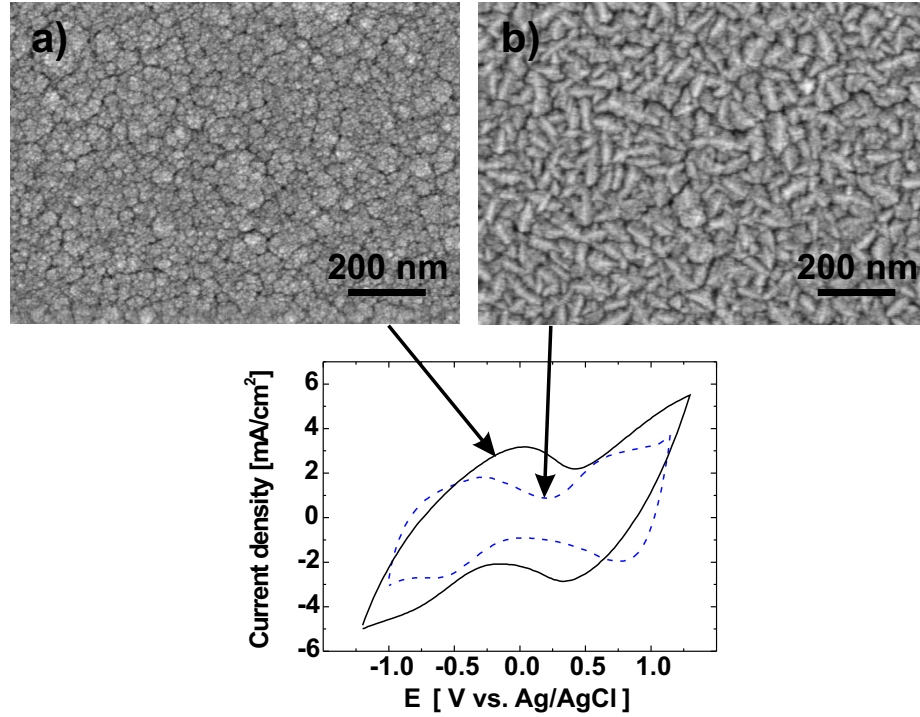Figure 7.1: Surface SEM images of two as-deposited samples processed at 1000 W DC, $WD = 78$ mm and $p = 9.3 \cdot 10^{-2}$ mbar, a) with, b) without reactive gas component during sputtering. CV measurements on samples after 100-fold activation are shown below.

tered at $Q(O_2) = 34.7$ sccm, delivering the highest oxygen integration into the film, and the highest electrochemical activity. The surface is composed

of void-separated tops of growth columns. Furthermore, the surface is rough and underdense. The distinct tops of growth columns are also visible on the metallic sample shown in part b), however, the structures are more elongated. The regrowth of small columnar structures on top of the bigger ones, the self-similarity, is not as evident for the metallic sample as for the oxidic sample, and the surface appears denser. However, in total, the combination of low incident energy and chemical reactions does not bring about a new type of surface appearance.

The corresponding CV curves of metallic and optimized oxidic samples are shown in the lower part of Fig. 7.1. At equivalent voltage excitation, the current response of the oxidic film is stronger than that of the metallic film. The anodic charge delivery after 100-fold activation increases by a factor of 1.6 from 45 to 72 mC/cm^2.

The increase in charge delivery is related to higher numbers of available centers for redox reactions. As mentioned in chapter 3, the presence of reactive oxygen species alters surface diffusion on the growing film. The average diffusion length of arriving adatoms decreases during reactive sputtering compared to the case of metal sputtering, as the Ir adatom can be oxidized [86, 87]. Also the resulting compound is of low mobility, and further diffusion is quenched. Due to repeated renucleation, crystallite sizes of only few nanometers develop [88, 149]. This is corroborated by the lack of XRD-detectable crystallinity in the reactively sputtered films.

The unordered growth results in high defect densities, which causes the development of high specific surfaces. With added oxygen, the surface shows more evidence of self-repetition in structures than the metallic counterpart, which is a result of less diffusion and more frequent renucleation.

Besides smaller surface mobility during sputter deposition, reactive sputtering also causes the growth of IrO$_2$ unit cells, with a lower density than Ir. It is plausible that the lower density enables easier ion insertion into the material. However, this effect remains a matter of speculation at this stage, and the contribution of the two effects to the increase in available reaction sites can not be quantified.

The delivered charge increases only slightly due to addition of oxygen to the low-mobility metal sputter process. The added oxygen does not have dramatic effects on surface mobility, because it is already low for the basic metal process. The eventual effects resulting from easier ion insertion into low-density IrO$_2$ cells additionally increase the charge delivery.

Contrarily, if a metal process is used that provides a higher initial surface mobility, the addition of oxygen to the process drastically decreases diffusivity. This explains the strong increase in electrochemical activity seen in chapter 3.

A comparison to the results achieved in chapters 3 and 4 shows that the optimized oxidic films deliver roughly the same charge, independent of the underlying metal process.[1] Additionally, the comparison of SEM surface images shows similar topographies (Figs. 7.1a) and 4.2c) on page 36). In both cases, self-similar structures with low densities and high roughness develop.

The similarity underlines the strong potential of optimized oxygen supply regarding a reduction of surface mobility. It is not significant whether the incident kinetic energies of Ir adatoms are low (0.2 eV) or in the medium energy range (6-7 eV). The optimization of oxygen supply leads to minimal surface mobility, which causes repeated renucleation and the growth of high-surface films.

As a further essential result, making use of the wide range of parameters and tools discussed in the preceding chapters, the charge delivery of Ir and/or IrOx thin films is limited to the values shown in chapters 3 and 4 (Q_a around 80-90 mC/cm^2), and can be considered optimized. The optimization is based on shadowing, the smallest possible surface mobility and the use of low-density IrO$_2$ material. Additionally, the films are activated with up to 100 potential cycles in electrolyte. A further strong increase in specific surface is only possible by enhancing the effects of shadowing during growth, as shown in the next section.

7.2   Film thickness increase

Shadowing induces open column boundaries because high points receive more off-angular coating flux, and subsequent overgrowth of smaller columns leads to formation of channels and pores. At low adatom mobilities, these effects can not be compensated for, and an underdense material develops.

Based on the use of low-mobility conditions, shadowing effects can be enhanced by making use of substrate irregularities.[2] Single substrate defects such as contaminations lead to preferred nucleation and growth of nodules [150], the same is true for a rough substrate [151]. Furthermore, oblique deposition, i. e., the forced off-axis incidence of coating material, has been demonstrated to enhance shadowing [152].

As a further option, this section presents enhanced shadowing by film thickness increase [153]. Several publications showed that the surface roughness r of coatings follows a power-law dependence on sputter time t, $r \propto t^\beta$,

---

[1]The slightly lower values of Q_a reported here compared to the earlier chapters are explained by a smaller number of evaluated thin films.

[2]Again, thermal evaporation of Ir would provide low-mobility conditions, however, the deposition in ultra-high vacuum rules out shadowing effects.

where β is a constant [154–157]. Thus, concerning the subsequent enhanced shadowing, a roughened surface of a thick film is equivalent to the introduction of rough substrates.

Using the same process parameters for low mobility as in the previous section (1000 W DC, $WD = 78$ mm and $p = 9.3 \cdot 10^{-2}$ mbar), the film thickness is increased from 330 to 600, 1000, 1500 and 3000 nm by increasing the sputter time. The films are not sputtered reactively in order to reduce the complexity during deposition, however, the following results are equally valid for sputtered IrOx.

The resulting anodic charge delivery capacities Q_a determined after 100 activation cycles are shown in Fig. 7.2 as a function of film thickness. The
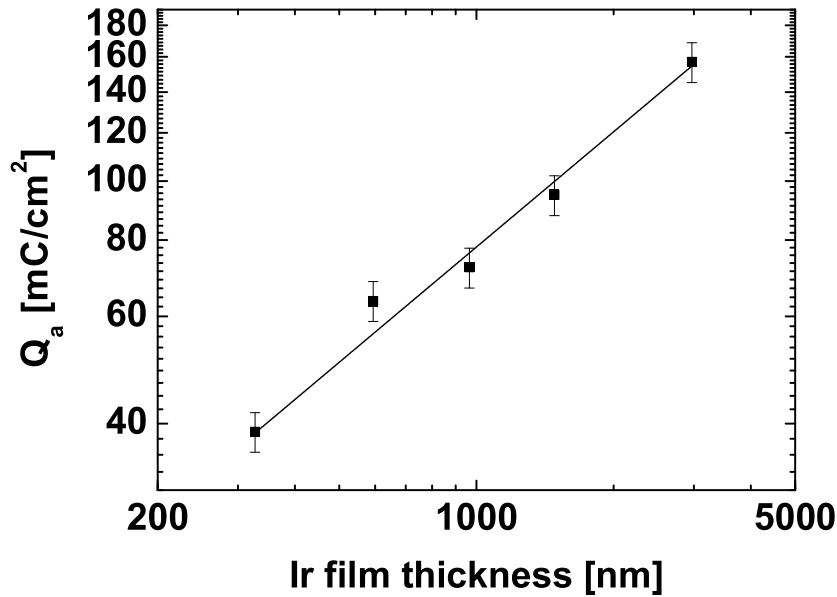
Figure 7.2: Anodic charge delivery capacities Q_a of Ir films after 100-fold activation cycling. Films are deposited to different thicknesses under equivalent conditions (1000 W DC, $WD = 78$ mm and $p = 9.3 \cdot 10^{-2}$ mbar).

thickest film, at almost 3000 nm, delivers a charge of 157 mC/cm², which is an increase by a factor of 4 from the lowest value. Furthermore, the delivered charges are considerably higher than the literature values shown in section 1.2.3. The included fit is a power law, with a power exponent of 0.6. A

further film thickness increase is likely to also further increase the charge delivery.

The reason for increased electrochemical activity can again be considered geometrical and is based on the availability of specific surface for charge transfer reactions. As has been detailed, the greater film thickness increases roughness and thus promotes further shadowing, which can not be compensated for by adatom diffusion due to the choice of process parameters. As demonstrated in section 6.3.2, open boundaries develop, which are accessible for the electrolyte.

As an illustration, Fig. 7.3a) shows a surface SEM image of the thickest sample. Fig. 7.3b) shows the top part of a fracture cross section of the same sample.

The earlier discussed self-similarity is even more apparent here. Similar to earlier reports on thick sputtered Ir coatings, a nodular, cauliflower-type surface develops [32]. As Fig. 7.3a) shows, big columns with diameters greater than 400 nm are separated by large voids of up to 20 nm width. On these columns, smaller columns protrude, which are again separated by voids. Fig. 7.3b) shows that each of the fractured big columns is composed of smaller units. Furthermore, the cross sectional view illustrates the roughness which both causes and results from shadowing. The clearly visible self-similar scaling supports an easy accessibility of Ir by an electrolyte.

7.3   Summary

Starting from low-mobility process conditions for Ir deposition, the addition of optimized reactive gas flow delivered IrOx thin films of higher electrochemical activity. The differences were based on an increased surface for charge transfer reactions. It developed due to decreased surface mobility of species during sputtering and, possibly, the lower density of IrO_2 cells. The contribution of both mechanisms to the increase in available surface could not be quantified. However, based on evaluation of SEM, XRD and the modelled diffusion lengths for the metal process, the results implied almost negligible surface mobility of Ir adatoms or compounds.

IrOx films deposited at optimal oxygen supply but differing kinetic energies of Ir adatoms (0.2 vs. 6-7 eV) were similar in structure and electrochemical activity. This allowed to conclude that optimal oxygen supply minimizes surface mobility also if the incident Ir atoms are of medium energy.

The anodic charge delivery of Ir and/or IrOx thin films (300-400 nm thick) reaches a limit of Q_a around 80-90 mC/cm^2 in the given measurement conditions. It is determined by the use of shadowing effects, optimization of
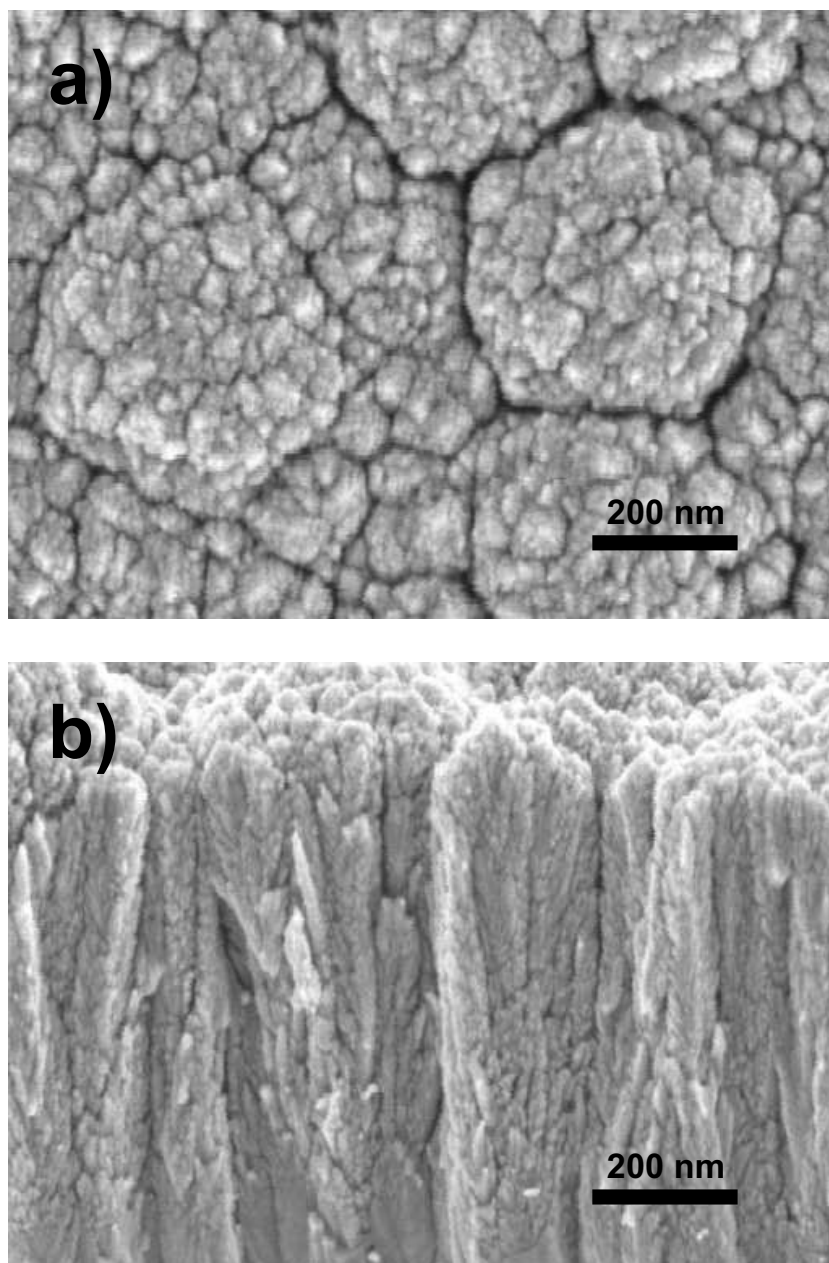
Figure 7.3: a) Surface SEM image of an Ir film deposited to 3000 nm thickness under low-mobility conditions. b) Top part of a fracture cross section of the same sample.

low-mobility conditions and deposition of low-density IrO_2 unit cells. Additionally, the films were activated electrochemically.

The specific surface was further increased by enhancing the effects of shadowing during growth. Film thickness increase was used as an example to illustrate the effects of stronger shadowing. The thickest Ir film, at almost 3000 nm, delivered an anodic charge of 157 mC/cm^2 after 100-fold potential cycling. The results are equally valid for reactive deposition of IrOx.

The reason for increased electrochemical activity was again based on the availability of specific surface for charge transfer reactions. Using low-mobility conditions, the greater film thickness increased the roughness and thus promoted further shadowing and the growth of open surfaces. Nodular, cauliflower-type surfaces developed, which allowed an easy accessibility of Ir by an electrolyte.

Chapter 8

Conclusions

8.1 Summary

The goal of this work was to determine the process parameters and underlying effects that allow to sputter deposit Ir and IrOx coatings of high electrochemical activity. Experiments and simulations were used to explain the interrelations between sputter parameters and film growth, the resulting microstructure and its electrochemical performance. In order to deposit a highly active coating, the sputter process has to provide for a strong expression of shadowing effects, minimal mobility of the sputtered atoms on the surface, and the deposition of low-density IrO_2 unit cells. Their combination ensures the deposition of a voided and underdense film supporting the accessibility of Ir reaction sites by an electrolyte. Subsequent activation of the deposited film by repeated potential cycling in electrolyte further improves the accessibility of redox centers.

A comprehensive investigation of RF-powered reactive sputtering showed that the process and film characteristics are unambiguously tied to the rate of oxygen integration v_f into the growing film. This was shown for the first time. v_f is proportional to the difference of oxygen partial pressures before and after ignition of the plasma, and was developed as a function of the oxygen supply $Q(O_2)$. $v_{f,max}$ took the shape of a plateau, along which target poisoning occurred. At the beginning of the plateau, the electrochemically most active films were deposited, with columnar morphologies. At its end, the highest deposition rate was measured, and the morphology changed to a platelet structure.

The composition and electrochemical analysis of films deposited at different oxygen supplies did not suggest general differences in redox behavior. Independent of oxygen supply during sputtering, equivalent redox reactions

were initiated in the film when subject to cyclic voltammetry in saline solution. The existing differences in the magnitudes of redox currents were linked to available active sites and accordingly, the film topography.

The RF-powered reactive sputter deposition was compared to DC reactive deposition under otherwise equivalent sputter conditions. Furthermore, the influence of additional substrate heating to 250 °C during RF sputtering was investigated. The dependencies of film and process characteristics on the rate of oxygen integration v_f into the growing film were similar for all conditions.

DC deposition onto cooled substrates favored the development of rough and voided films. Compared to these, RF sputtering delivered tighter packed deposits. During RF sputtering, the plasma expands further from the target than during DC deposition. This leads to a higher flux of energetic plasma species (Ar neutrals and ions) from the plasma region to the substrate. The additional energy input amplifies surface atom mobility, which effectuates tighter packing. A heated substrate further amplified atom mobility and reorganization. Partial crystallinity developed, and the films were even tighter packed. As chemical composition and electrochemical analysis showed, plasma excitation mode (RF, DC) and substrate temperature (room temperature, 250 °C) did not exert major influence on chemical composition. However, the magnitudes of electrochemical current responses to voltage excitation in electrolyte were largely different. Again, the existing strong differences in electrochemical activity had to be explained on grounds of the openness of film morphologies.

The reason for increased electrochemical activity of IrOx films due to repeated potential cycling (activation) was investigated by chemical and morphology analysis and depth profiling. It was shown that activation transforms between iridium oxides and hydroxides. The transformation implies that the binding forces on Ir species in relation to the metal-oxide lattice practically vanish. As a result, the columnar structure of deposited IrOx films transmuted to a non-compact matrix, which enabled easier ion insertion to redox centers. The results are similar to other authors' findings related to the activation of metallic Ir.

As all results showed, film microstructure determines the electrochemical activity. A comprehensive set of experiments was developed in order to further investigate the influence of microstructure on the characteristics of charge delivery to an electrolyte. Within this series of experiments, the angular and energy distributions of Ir adatoms were modified. It represented the first attempt to clarify the relations between the evolution of microstructure during film growth and the electrochemical characteristics of the deposited film. The influences of oxygen during sputtering and of activation during electrochemical characterization were eliminated. Two simulators were de-

veloped describing both the transport of sputtered atoms from target to substrate as well as film growth.

The incident angles of sputtered atoms and their kinetic energies were modelled using a Monte Carlo approach. The incident angles were distributed for all investigated conditions. The mean incident energies ranged from around 12 eV to thermal energy.

The 2D Monte Carlo model of film growth explains and predicts Ir microstructure evolution as a function of adatom angular and kinetic energy distributions. It is the first model describing the evolution of Ir thin film microstructure, and one of the few focussing on the influence of adatom kinetic energy on film structure. The model was verified by density measurements and the evaluation of microstructures.

Supported by the models, the experiments illustrated that energy and angular distributions of incident atoms decisively influence the microstructure of metallic Ir thin films deposited onto cold substrates. Distinct morphologies were generated by altering the process parameters DC power, pressure and target-substrate distance.

All films were characterized by a columnar growth, however, the formation of voids between the columns and the expression of surface roughness were dependent on the deposition conditions. The least dense films evolved from conditions of lowest adatom mobility and strong shadowing. The latter was shown to occur for all investigated conditions. At higher mobilities, the diffusion of adatoms partially compensated the shadowing effects, and denser films evolved.

In the investigated parameter sets, the adatom surface mobilities were determined mainly by their incident kinetic energies. At low incident kinetic energies and thus low adatom mobilities, films of high specific surface and high electrochemical activity were deposited. The evaluation of cyclic voltammograms showed that compared to densely packed films, the anodically delivered charge was increased by a factor of roughly 37. The increase was solely determined by film morphology.

The film growth model explained the differences in measured delivered charge on grounds of accessibility of film atoms by electrolyte. The measurements and model outputs were congruent and alike functions of mean adatom kinetic energy.

Most Ir films evaluated for crystallographic orientation were weakly {220}-oriented. The orientation preference transformed to {111} with increasing incident energy. This was explained by a stronger lateral spreading of {111} grains due to higher adatom mobility. Higher diffusivity lead to overgrowth of other orientations, and material loss of these. The development of {111} texture over adatom energy inversely correlated with the development of

electrochemical activity. Films containing stronger {220} contribution were rougher, with lower densities and stronger void formation, which increases the specific surface. The experimentally observed development of crystallographic orientation was predicted qualitatively by the simulation.

Finally, a process providing low adatom mobility for deposition of metallic Ir was combined with the optimized reactive sputtering approach. This process ensured the combination of low-mobility adatom conditions, high shadowing and the use of low-density oxide unit cells, added to subsequent electrochemical activation. The results showed that the electrochemically delivered charge of Ir and/or IrOx thin films reaches a limit around 80-90 mC/cm^2 in the given measurement conditions.

Equivalent charge deliveries were measured after reactive deposition under considerably higher kinetic energies of Ir adatoms. XRD, SEM and the simulated diffusion lengths for the low-mobility metal process were evaluated. The results implied that optimal oxygen supply minimizes adatom surface mobility for both low- and medium-energy adatoms. The minimized diffusivity is caused by the oxidation of Ir on the film surface.

The specific surface available for charge transfer could only be further increased by enhancing the effects of shadowed growth. Film thickness increase was used as an illustration. The increase in film thickness provided a rougher surface for subsequently deposited atoms, leading to the development of stronger shadowing effects. Using a process supplying low-mobility Ir atoms to the surface, the thickest evaluated Ir film, at almost 3000 nm, delivered an anodic charge of 157 mC/cm^2 after 100-fold potential cycling, considerably more than earlier literature reports.

8.2   Outlook

The thermal evaporation of Ir provides the low adatom mobility needed for deposition of high-surface films. However, due to processing under ultra-high vacuum, self-shadowing effects are ruled out. Nevertheless, by making use of structured and inclined substrates, shadowed growth can be forced. Furthermore, the application of inclined and tilting or rotating substrates allows the deposition of open structures in form of separated pillars, helices or zigzags. These types of structure promise a high accessibility of redox centers by electrolyte.

Regarding the description of Ir thin film growth, the present model can be completed to incorporate thermally activated diffusion, the energy transported to the substrate via plasma particles, and deposition rate or time dependence of film growth.

The existing model includes a number of assumptions regarding the effects of latent heat release, resputtering probabilities and surface diffusion lengths. In order to improve the parameters, more detailed investigations such as molecular dynamics simulations need to be performed. However, compared to the deposition of metallic films, the understanding of substrate reactions and compound formation during reactive sputtering is not quite as advanced.

Apart from improvements in the description of film deposition, the modelling of the accessibility of redox centers by ionic solution promises further insights into electrode performance.

Glossary

Symbols

A_t	Simulated availability and accessibility of atoms for charge transfer
E	Electrode voltage vs. Ag/AgCl
E_{ad}	Incident kinetic energy of an adatom
E_b	Binding energy
E_{inc}	Mean incident kinetic energy of atoms on the substrate
E_{ion}	Kinetic energy of incident ions
E_m	Activation energy for thermally activated diffusion
d	Interatomic distance
f	Frequency
k	Boltzmann constant
M_i	Atomic weight of argon
M_t	Atomic weight of iridium
P	Sputter power or position label of atoms in simulated configurations
p	Pressure
$p(O_2)$	Oxygen partial pressure
Q_a	Anodic charge delivery capacity

$Q(Ar)$	Argon flow to the sputter chamber
$Q(O_2)$	Oxygen flow to the sputter chamber
R_I	Ratio of measured x-ray diffraction peak intensities {111}/{220}
R_N	Simulated ratio of atoms in {111}/{220}
r_{sg}	Interatomic separation of Ar and Ir in the gas phase
T	Temperature
T_{melt}	Melting temperature
$T_{substrate}$	Substrate temperature
V_b	Target bias voltage
v_f	Rate of oxygen integration into the growing film
v_p	System pumping speed
WD	Working distance, target-substrate distance
λ	Free path
ρ	Relative film density

Abbreviations and Acronyms

Ag	Silver
Ag/AgCl	Silver-silver chloride
AIROF	Anodic iridium oxide film
Al	Aluminium
Ar	Argon
Cr	Chromium
Cu	Copper

CV	Cyclic voltammetry
EIROF	Electrodeposited iridium oxide film
fcc	Face-centered cubic
Fe	Iron
HS	Hard sphere
Ir	Iridium
IrOx	Iridium oxide
MC	Monte Carlo
MD	Molecular dynamics
Mo	Molybdenum
Ni	Nickel
Pb	Lead
Pt	Platinum
PZT	$Pb(Zr, Ti)O_3$
SEM	Scanning electron microscopy
Si	Silicon
SIROF	Sputtered iridium oxide film
Ta	Tantalum
Ti	Titanium
ToF − SIMS	Time-of-flight secondary ion mass spectroscopy
VHS	Variable hard sphere
W	Tungsten
XPS	X-ray photoelectron spectroscopy
XRD	X-ray diffraction
XRR	X-ray reflectometry
Zr	Zirconium

Bibliography

[1] H. J. Cho, H. Horii, C. S. Hwang, J. W. Kim, C. S. Kang, B. T. Lee, S. I. Lee, Y. B. Koh, and M. Y. Lee. Preparation and characterization of iridium oxide thin films grown by DC reactive sputtering. *Japanese Journal of Applied Physics Part 1*, 36 (3B): 1722–1727, 1997.

[2] G. R. Fox, S. Sun, and T. Takamatsu. Properties of reactively sputtered IrOx for PZT electrode applications. *Integrated Ferroelectrics*, 31 (1-4): 47–56, 2000.

[3] N. Inoue and Y. Hayashi. Smart fabrication process of an Ir-IrOx top-electrode on a PZT film for reliable FeRAM. *Journal of the Electrochemical Society*, 151 (2): G113–G118, 2004.

[4] T. Nakamura, Y. Nakao, A. Kamisawa, and H. Takasu. Preparation of $Pb(Zr, Ti)O_3$ thin-films on electrodes including IrO_2. *Applied Physics Letters*, 65 (12): 1522–1524, 1994.

[5] C. U. Pinnow, I. Kasko, C. Dehm, B. Jobst, M. Seibt, and U. Geyer. Preparation and properties of DC-sputtered IrO_2 and Ir thin films for oxygen barrier applications in advanced memory technology. *Journal of Vacuum Science and Technology B*, 19 (5): 1857–1865, 2001.

[6] C. U. Pinnow, I. Kasko, N. Nagel, S. Poppa, T. Mikolajick, C. Dehm, W. Hosler, F. Bleyl, F. Jahnel, M. Seibt, U. Geyer, and K. Samwer. Influence of deposition conditions on Ir/IrO_2 oxygen barrier effectiveness. *Journal of Applied Physics*, 91 (12): 9591–9597, 2002.

[7] K. Kuribayashi, Y. Fujita, H. Isige, and T. Iwanuma. Sputter deposited Pt-Ir oxides thin films and their characterization. *Materials Science and Engineering B*, 109 (1-3): 188–191, 2004.

[8] H. S. Lee, W. S. Um, K. T. Hwang, H. G. Shin, Y. B. Kim, and K. H. Auh. Ferroelectric properties of $Pb(Zr, Ti)O_3$ thin films deposited on

annealed IrO_2 and Ir bottom electrodes. *Journal of Vacuum Science & Technology A*, 17 (5): 2939–2943, 1999.

[9] B. R. Chalamala, Y. Wei, R. H. Reuss, S. Aggarwal, B. E. Gnade, R. Ramesh, J. M. Bernhard, E. D. Sosa, and D. E. Golden. Effect of growth conditions on surface morphology and photoelectric work function characteristics of iridium oxide thin films. *Applied Physics Letters*, 74 (10): 1394–1396, 1999.

[10] T. J. Park, D. S. Jeong, C. S. Hwang, M. S. Park, and N. S. Kang. Fabrication of ultrathin IrO_2 top electrode for improving thermal stability of metal-insulator-metal field emission cathodes. *Thin Solid Films*, 471 (1-2): 236–242, 2005.

[11] R. S. Chen, Y. S. Huang, Y. M. Liang, D. S. Tsai, and K. K. Tiong. Growth and characterization of iridium dioxide nanorods. *Journal of Alloys and Compounds*, 383 (1-2): 273–276, 2004.

[12] J. Backholm, A. Azens, and G. A. Niklasson. Electrochemical and optical properties of sputter deposited Ir-Ta and Ir oxide thin films. *Solar Energy Materials & Solar Cells*, 90: 414–421, 2006.

[13] G. Beni and L. M. Schiavone. Matrix-addressable electrochromic display cell. *Applied Physics Letters*, 38 (8): 593–595, 1981.

[14] S. Hackwood, A. H. Dayem, and G. Beni. Amorphous-nonmetal to crystalline-metal transition in electrochromic iridium oxide-films. *Physical Review B*, 26 (2): 471–478, 1982.

[15] K. S. Kang and J. L. Shay. Blue sputtered iridium oxide-films (blue SIROFs). *Journal of the Electrochemical Society*, 130 (4): 766–769, 1983.

[16] G. Beni, C. E. Rice, and J. L. Shay. Electrochromism of anodic iridium oxide-films: 3. Anion mechanism. *Journal of the Electrochemical Society*, 127 (6): 1342–1348, 1980.

[17] T. Pauporte, D. Aberdam, J. L. Hazemann, R. Faure, and R. Durand. X-ray absorption in relation to valency of iridium in sputtered iridium oxide films. *Journal of Electroanalytical Chemistry*, 465 (1): 88–95, 1999.

[18] S. Hackwood, W. C. Dautremontsmith, G. Beni, L. M. Schiavone, and J. L. Shay. Volume changes induced by the electrochromic process in

sputtered iridium oxide films. *Journal of the Electrochemical Society*, 128 (6): 1212–1214, 1981.

[19] S. Hackwood, G. Beni, M. A. Bosch, K. Kang, L. M. Schiavone, and J. L. Shay. New process for optical information-storage. *Physical Review B*, 26 (12): 7073–7075, 1982.

[20] M. A. Bösch, K. Kang, S. Hackwood, G. Beni, and J. L. Shay. Optical writing on blue, sputtered iridium oxide films. *Applied Physics Letters*, 41 (1): 103–105, 1982.

[21] S. Yao, M. Wang, and M. Madou. A pH electrode based on melt-oxidized iridium oxide. *Journal of the Electrochemical Society*, 148 (4): H29–H36, 2001.

[22] D. O. Wipf, F. Ge, T. W. Spaine, and J. E. Baur. Microscopic measurement of pH with iridium oxide microelectrodes. *Analytical Chemistry*, 72: 4921–427, 2000.

[23] I. Lauks, M. F. Yuen, and T. Dietz. Electrically free-standing IrOx thin film electrodes for high-temperature, corrosive environment pH sensing. *Sensors and Actuators*, 4: 375–379, 1983.

[24] K. Kreider. IrO$_2$ radiofrequency sputtered thin-film properties. *Journal of Vacuum Science & Technology A*, 4 (3): 606–607, 1986.

[25] K. Kreider and M. Tarlov. Stability of iridium oxide films in high temperature, 200-250°, solutions. *4th Technical Digest of IEEE Solid-State Sensor and Actuator Workshop*, 42 – 43, 1990.

[26] I. M. Kodintsev, S. Trasatti, M. Rubel, A. Wieckowski, and N. Kaufher. X-ray photoelectron-spectroscopy and electrochemical surface characterization of IrO$_2$ + RuO$_2$ electrodes. *Langmuir*, 8 (1): 283–290, 1992.

[27] R. Kötz, H. Neff, and S. Stucki. Anodic iridium oxide-films - XPS-studies of oxidation-state changes and O$_2$-evolution. *Journal of the Electrochemical Society*, 131 (1): 72–77, 1984.

[28] S. Hackwood, L. M. Schiavone, W. C. Dautremontsmith, and G. Beni. Anodic evolution of oxygen on sputtered iridium oxide-films. *Journal of the Electrochemical Society*, 128 (12): 2569–2573, 1981.

[29] S. Gottesfeld and S. Srinivasan. Electrochemical and optical studies of thick oxide layers on iridium and their electrocatalytic activities for

oxygen evolution reaction. *Journal of Electroanalytical Chemistry*, 86 (1): 89–104, 1978.

[30] E. Slavcheva, R. Vitushinsky, W. Mokwa, and U. Schnakenberg. Sputtered iridium oxide films as charge injection material for functional electrostimulation. *Journal of the Electrochemical Society*, 151 (7): E226–E237, 2004.

[31] W. Mokwa. MEMS technologies for epiretinal stimulation of the retina. *Journal of Micromechanics and Microengineering*, 14 (9): 12–16, 2004.

[32] S.F. Cogan, T.D. Plante, and J. Ehrlich. Sputtered iridium oxide films (SIROF) for low-impedance neural stimulation and recording electrodes. In *Annual International Conference of the IEEE EMBS*, pages 4153–4156, San Francisco, USA, 2004.

[33] S. F. Cogan, P. R. Troyk, J. Ehrlich, T. D. Plante, and D. E. Detlefsen. Potential-biased, asymmetric waveforms for charge-injection with activated iridium oxide (AIROF) neural stimulation electrodes. *IEEE Transactions on Biomedical Engineering*, 53 (2): 327–332, 2006.

[34] S. F. Cogan, A. A. Guzelian, W. F. Agnew, T. G. H. Yuen, and D. B. McCreery. Over-pulsing degrades activated iridium oxide films used for intracortical neural stimulation. *Journal of Neuroscience Methods*, 137 (2): 141–150, 2004.

[35] A. Blau, C. Ziegler, M. Heyer, F. Endres, G. Schwitzgebel, T. Matthies, T. Stieglitz, J. U. Meyer, and W. Gopel. Characterization and optimization of microelectrode arrays for in vivo nerve signal recording and stimulation. *Biosensors & Bioelectronics*, 12 (9-10): 883–892, 1997.

[36] R. Fröhlich, A. Rzany, J. Riedmuller, A. Bolz, and M. Schaldach. Electroactive coating of stimulating electrodes. *Journal of Materials Science-Materials in Medicine*, 7 (7): 393–397, 1996.

[37] J. D. Weiland and D. J. Anderson. Chronic neural stimulation with thin-film, iridium oxide electrodes. *IEEE Transactions on Biomedical Engineering*, 47 (7): 911–8, 2000.

[38] In-Seop Lee, Chung-Nam Whang, Kyung Choi, Myung-Soo Choo, and Young-Hee Lee. Characterization of iridium film as a stimulating neural electrode. *Biomaterials*, 23: 2375–2380, 2002.

[39] I. S. Lee, C. N. Whang, J. C. Park, D. H. Lee, and W. S. Seo. Biocompatibility and charge injection property of iridium film formed by ion beam assisted deposition. *Biomaterials*, 24 (13): 2225–2231, 2003.

[40] S. J. Tanghe, K. Najafi, and K. D. Wise. A planar IrO multichannel stimulating electrode for use in neural prostheses. *Sensors and Actuators B*, B1: 464–467, 1990.

[41] M. P. Maher, J. Pine, J. Wright, and Y. C. Tai. The neurochip: a new multielectrode device for stimulating and recording from cultured neurons. *Journal of Neuroscience Methods*, 87 (1): 45–56, 1999.

[42] M. S. Humayun, J. D. Weiland, G. Y. Fujii, R. Greenberg, R. Williamson, J. Little, B. Mech, V. Cimmarusti, G. Van Boemel, G. Dagnelie, and E. de Juan. Visual perception in a blind subject with a chronic microelectronic retinal prosthesis. *Vision Research*, 43 (24): 2573–81, 2003.

[43] J. D. Weiland, D. J. Anderson, and M. S. Humayun. In vitro electrical properties for iridium oxide versus titanium nitride stimulating electrodes. *IEEE Transactions on Biomedical Engineering*, 49 (12): 1574–1579, 2002.

[44] E. Slavcheva, L. Ewe, U. Schnakenberg, and W. Mokwa. Electrochemical characterisation of different biocompatible metallic materials as planar and 3D-electrodes in neural stimulation microarrays. In *Proc. 2nd European Medical & Biological Engineering Conference*, Vienna, Austria, 2002.

[45] S. F. Cogan, P. R. Troyk, J. Ehrlich, and T. D. Plante. In vitro comparison of the charge-injection limits of activated iridium oxide (AIROF) and platinum-iridium microelectrodes. *IEEE Transactions on Biomedical Engineering*, 52 (9): 1612–1614, 2005.

[46] G. Beni and J. L. Shay. New electrochromism isotherm in anodic iridium oxide-films. *Physical Review B*, 21 (2): 364–367, 1980.

[47] L. D. Burke and D. P. Whelan. A new interpretation of the charge storage and electrical-conductivity behavior of hydrous iridium oxide. *Journal of Electroanalytical Chemistry*, 124 (1-2): 333–337, 1981.

[48] S. C. Mailley, M. Hyland, P. Mailley, J. M. McLaughlin, and E. T. McAdams. Electrochemical and structural characterizations of electrodeposited iridium oxide thin-film electrodes applied to neuro stim-

ulating electrical signal. *Materials Science & Engineering C*, 21 (1-2): 167–175, 2002.

[49] R. D. Meyer, S. E. Cogan, T. H. Nguyen, and R. D. Rauh. Electrodeposited iridium oxide for neural stimulation and recording electrodes. *IEEE Transactions on Neural Systems and Rehabilitation Engineering*, 9 (1): 2–11, 2001.

[50] J. Augustynski, M. Koudelka, J. Sanchez, and B. E. Conway. ESCA study of the state of iridium and oxygen in electrochemically and thermally formed iridium oxide-films. *Journal of Electroanalytical Chemistry*, 160 (1-2): 233–248, 1984.

[51] A. Karthigeyan, R. P. Gupta, K. Scharnagl, M. Burgmair, S. K. Sharma, and I. Eisele. A room temperature HSGFET ammonia sensor based on iridium oxide thin film. *Sensors and Actuators B*, 85 (1-2): 145–153, 2002.

[52] N. Bestaoui, E. Prouzet, P. Deniard, and R. Brec. Structural and analytical characterization of an iridium oxide thin-layer. *Thin Solid Films*, 235 (1-2): 35–42, 1993.

[53] K. Nishio, Y. Watanabe, and T. Tsuchiya. Preparation and properties of electrochromic iridium oxide thin film by sol-gel process. *Thin Solid Films*, 350 (1-2): 96–100, 1999.

[54] M. A. El Khakani and M. Chaker. Reactive pulsed laser deposition of iridium oxide thin films. *Thin Solid Films*, 335 (1-2): 6–12, 1998.

[55] A. M. Serventi, M. A. El Khakani, R. G. Saint-Jacques, and D. G. Rickerby. Highly textured nanostructure of pulsed laser deposited IrO_2 thin films as investigated by transmission electron microscopy. *Journal of Materials Research*, 16 (8): 2336–2342, 2001.

[56] R. S. Chen, Y. S. Huang, Y. M. Liang, D. S. Tsai, Y. Chi, and J. J. Kai. Growth control and characterization of vertically aligned IrO_2 nanorods. *Journal of Materials Chemistry*, 13 (10): 2525–2529, 2003.

[57] J.D. Klein, S. L. Clauson, and S. F. Cogan. The influence of substrate bias on the morphology and charge capacity of RF-sputtered iridium oxide films. *Journal of Materials Research*, 4 (6): 1505–1510, 1989.

[58] T. Katsube, I. Lauks, and J. N. Zemel. PH-sensitive sputtered iridium oxide-films. *Sensors and Actuators*, 2 (4): 399–410, 1982.

[59] I. Safi. Recent aspects concerning DC reactive magnetron sputtering of thin films: A review. *Surface and Coatings Technology*, 127 (2-3): 203–219, 2000.

[60] S. Berg, H.-O. Blom, T. Larsson, and C. Nender. Modelling of reactive sputtering of compound materials. *Journal of Vacuum Science & Technology A*, 5 (2): 202–207, 1987.

[61] R. H. Horng, D. S. Wuu, L. H. Wu, and M. K. Lee. Formation process and material properties of reactive sputtered IrO_2 thin films. *Thin Solid Films*, 373 (1-2): 231–234, 2000.

[62] J. D. Klein, S. L. Clauson, and S. F. Cogan. Morphology and charge capacity of sputtered iridium oxide-films. *Journal of Vacuum Science & Technology A*, 7 (5): 3043–3047, 1989.

[63] E. Eser, R. E. Ogilvie, and K. A. Taylor. Measurement of plasma discharge characteristics for sputtering applications. *Journal of Vacuum Science and Technology*, 15 (2): 199–202, 1978.

[64] B. Window and G. L. Harding. Characterization of radio-frequency unbalanced magnetrons. *Journal of Vacuum Science & Technology A*, 10 (5): 3300–3304, 1992.

[65] M. Bender, J. Trube, and J. Stollenwerk. Characterization of a RF/DC-magnetron discharge for the sputter deposition of transparent and highly conductive ITO films. *Applied Physics A–Materials Science & Processing*, 69 (4): 397–401, 1999.

[66] N. Martin and C. Rousselot. Use of a theoretical model to investigate RF and DC reactive sputtering of titanium and chromium oxide coatings. *Surface and Coatings Technology*, 110 (3): 158–167, 1998.

[67] R. Cremer, M. Witthaut, D. Neuschutz, G. Erkens, T. Leyendecker, and M. Feldhege. Comparative characterization of alumina coatings deposited by RF, DC and pulsed reactive magnetron sputtering. *Surface and Coatings Technology*, 121: 213–218, 1999.

[68] K. Ellmer and R. Wendt. DC and RF (reactive) magnetron sputtering of ZnO:Al films from metallic and ceramic targets: a comparative study. *Surface & Coatings Technology*, 93 (1): 21–26, 1997.

[69] R. Cebulla, R. Wendt, and K. Ellmer. Al-doped zinc oxide films deposited by simultaneous RF and DC excitation of a magnetron plasma:

Relationships between plasma parameters and structural and electrical film properties. *Journal of Applied Physics*, 83 (2): 1087–1095, 1998.

[70] R. Mientus and K. Ellmer. Reactive magnetron sputtering of TiN-doped indium oxide (ITO): influence of argon pressure and plasma excitation mode. *Surface & Coatings Technology*, 142: 748–754, 2001.

[71] D. Hariskos, R. Menner, S. Spiering, A. Eicke, M. Powalla, K. Ellmar, M. Oertel, and B. Dimmler. In_2S_3 buffer layer deposited by magnetron sputtering for $Cu(InGa)Se_2$ solar cells. *Proc. Solar Energy Conference* , Paris, France, 2004.

[72] A. Bogaerts and R. Gijbels. Similarities and differences between direct current and radio-frequency glow discharges: a mathematical simulation. *Journal of Analytical Atomic Spectrometry*, 15 (9): 1191–1201, 2000.

[73] R. M. Wightman and D. O. Wipf. Voltammetry at ultramicroelectrodes. *Electroanalytical Chemistry*, 15: 267–353, 1989.

[74] T. M. Silva, J. E. Rito, A. M. P. Simoes, M. G. S. Ferreira, M. D. Belo, and K. G. Watkins. Electrochemical characterisation of oxide films formed on Ti-6Al-4V alloy implanted with Ir for bioengineering applications. *Electrochimica Acta*, 43 (1-2): 203–211, 1998.

[75] X. Beebe and T. L. Rose. Charge injection limits of activated iridium oxide electrodes with 0.2ms pulses in bicarbonate buffered saline. *IEEE Transactions on Biomedical Engineering*, 35 (6): 494–495, 1988.

[76] EIC. www.eiclabs.com, 2007.

[77] L. M. Schiavone, W. C. Dautremontsmith, G. Beni, and J. L. Shay. Improved electrochromic behavior of reactively sputtered iridium oxide-films. *Journal of the Electrochemical Society*, 128 (6): 1339–1342, 1981.

[78] B. Wessling, K. Hungar, E. Slavcheva, W. Mokwa, and U. Schnakenberg. Sputtered iridium oxide as a top-layer of stimulating 3D-microelectrodes in retina implants. *Biomedical Engineering*, 50 (S1): 842–843, 2005.

[79] B. Wessling, A. van Ooyen, W. Mokwa, and U. Schnakenberg. Iridium sputtered at varying pressures and target-substrate distances evaluated for use as stimulation electrode material. In *Annual International Conference of the IEEE EMBS*, pages 3353–3356, New York City, USA, 2006.

[80] J. O. Zerbino, N. R. D. Tacconi, and A. J. Arvia. Activation and deactivation of iridium electrodes in acid electrolytes. *Journal of the Electrochemical Society*, 125 (8): 1266–1276, 1978.

[81] B. Lengeler and M. Hüppauff. Surface analysis by means of reflection, fluorescence and diffuse scattering of hard X-ray. *Fresenius Journal of Analytical Chemistry*, 346 (1-3): 155-161, 1993.

[82] E. Chason and T. M. Mayer. Thin film and surface characterization by specular X-ray reflectivity. *Critical Reviews in Solid State and Materials Science*, 22: 1-67, 1997.

[83] E. Kusano and D. M. Goulart. Time-dependent simulation modeling of reactive sputtering. *Thin Solid Films*, 193 (1-2): 84–91, 1990.

[84] R. A. Powell and S. Rossnagel. *PVD for microelectronics: Sputter deposition applied to semiconductor manufacturing*, vol. 26 of *Thin Films*. Academic Press, London, 1983.

[85] J. A. Thornton. Influence of apparatus geometry and deposition conditions on structure and topography of thick sputtered coatings. *Journal of Vacuum Science and Technology*, 11 (4): 666–670, 1974.

[86] J. A. Thornton. The microstructure of sputter-deposited coatings. *Journal of Vacuum Science & Technology A*, 4 (6): 3059–3065, 1986.

[87] Y. Abe, S.-H. Lee, E. O. Zayim, C. E. Tracy, J. R. Pitts, and S. K. Deb. Effect of O_2 flow concentration during reactive sputtering of Ni oxide thin films on their electrochemical and electrochromic properties in aqueous acidic and basic electrolyte solutions. *Japanese Journal of Applied Physics Part 1*, 45 (10A): 7780–7783, 2006.

[88] A. Kuzmin, R. Kalendarev, and J. Purans. Iridium l3-edge and oxygen k-edge x-ray absorption spectroscopy of nanocrystalline iridium oxide thin films. *Proceedings of SPIE*, Volume 5123: 210–214, 2003.

[89] R. Sanjines, A. Aruchamy, and F. Levy. Thermal stability of sputtered iridium oxide films. *Journal of the Electrochemical Society*, 136 (6): 1740–1743, 1989.

[90] A. Korotcov, Y. S. Huang, D. S. Tsai, and K. K. Tiong. Growth and characterization of well aligned densely packed IrO_2 nanocrystals on sapphire via reactive sputtering. *Journal of Physics: Condensed Matter*, 18: 1121–1136, 2006.

[91] Y. W. Jung, J. Lee, and Y. Tak. Electrochromic mechanism of IrO_2 prepared by pulsed anodic electrodeposition. *Electrochemical and Solid State Letters*, 7 (2): H5–H8, 2004.

[92] R. S. Chen, H. M. Chang, Y. S. Huang, D. S. Tsai, S. Chattopadhyay, and K. H. Chen. Growth and characterization of vertically aligned self-assembled IrO_2 nanotubes on oxide substrates. *Journal of Crystal Growth*, 271 (1-2): 105–112, 2004.

[93] M. Hüppauff and B. Lengeler. Valency and structure of iridium in anodic iridium oxide-films. *Journal of the Electrochemical Society*, 140 (3): 598–602, 1993.

[94] P. G. Pickup and V. I. Birss. The influence of the aqueous growth-medium on the growth-rate, composition, and structure of hydrous iridium oxide-films. *Journal of the Electrochemical Society*, 135 (1): 126–133, 1988.

[95] D. G. Coronell, E. W. Egan, G. Hamilton, A. Jain, R. Venkatraman, and B. Weitzman. Monte Carlo simulations of sputter deposition and step coverage of thin films. *Thin Solid Films*, 333 (1-2): 77–81, 1998.

[96] S. D. Ekpe and S. K. Dew. Theoretical and experimental determination of the energy flux during magnetron sputter deposition onto an unbiased substrate. *Journal of Vacuum Science & Technology A*, 21 (2): 476–483, 2003.

[97] V. V. Serikov and K. Nanbu. Monte Carlo numerical analysis of target erosion and film growth in a three-dimensional sputtering chamber. *Journal of Vacuum Science & Technology A*, 14 (6): 3108–3123, 1996.

[98] S. S. Nathan, G. M. Rao, and S. Mohan. Transport of sputtered atoms in facing targets sputtering geometry: A numerical simulation study. *Journal of Applied Physics*, 84 (1): 564–571, 1998.

[99] T. Motohiro. Applications of Monte-Carlo simulation in the analysis of a sputter-deposition process. *Journal of Vacuum Science & Technology A*, 4 (2): 189–195, 1986.

[100] T. Nakano and S. Baba. A hybrid simulation of high pressure sputtering, combining the Monte Carlo method and the diffusive approach. *Thin Solid Films*, 344: 24–26, 1999.

[101] G. M. Turner, I. S. Falconer, B. W. James, and D. R. McKenzie. Monte Carlo calculations of the properties of sputtered atoms at a substrate surface in a magnetron discharge. *Journal of Vacuum Science & Technology A*, 10 (3): 455–461, 1992.

[102] T. Smy, L. Tan, S. S. Winterton, S. K. Dew, and M. J. Brett. Simulation of sputter deposition at high pressures. *Journal of Vacuum Science & Technology A*, 15 (6): 2847–2853, 1997.

[103] M. J. Goeckner, J. A. Goree, and T. E. Sheridan. Monte-Carlo simulation of ions in a magnetron plasma. *IEEE Transactions on Plasma Science*, 19 (2): 301–308, 1991.

[104] M. W. Thompson. Energy spectrum of ejected atoms during high energy sputtering of gold. *Philosophical Magazine*, 18 (152): 377–414, 1968.

[105] M. Stepanova and S. K. Dew. Estimates of differential sputtering yields for deposition applications. *Journal of Vacuum Science & Technology A*, 19 (6): 2805–2816, 2001.

[106] Y. Yamamura, T. Takiguchi, and M. Ishida. Energy and angular-distributions of sputtered atoms at normal incidence. *Radiation Effects and Defects in Solids*, 118 (3): 237–261, 1991.

[107] S. D. Ekpe, L. W. Bezuidenhout, and S. K. Dew. Deposition rate model of magnetron sputtered particles. *Thin Solid Films*, 474 (1-2): 330–336, 2005.

[108] S. Ghosal, R.L. Kosut, J.L. Ebert, A. Kozak, and T.E. Abrahamson. Multi-scale model of the RF diode sputter deposition of GMR thin films. *Application Notes, SC Solutions, Santa Clara, USA*.

[109] A. A. Abrahamsom. Born-mayer-type interatomic potential for neutral ground-state atoms with z = 2 to z = 105. *Physical Review*, 178 (1): 76–79, 1968.

[110] L.D. Landau and E.M. Lifshitz. *Course of Theoretical Physics: Vol. 1: Mechanics.* Pergamon Press, Oxford, 1960.

[111] G. H. Gilmer, H. C. Huang, and C. Roland. Thin film deposition: fundamentals and modeling. *Computational Materials Science*, 12 (4): 354–380, 1998.

[112] I. Petrov, P. B. Barna, L. Hultman, and J. E. Greene. Microstructural evolution during film growth. *Journal of Vacuum Science & Technology A*, 21 (5): S117–S128, 2003.

[113] J. Dalla Torre, G. H. Gilmer, D.H. Windt, R. Kalyanaraman, F. H. Baumann, P. L. O'Sullivan, J. Sapjeta, T. Diaz de la Rubia, and M. Djafari Rouhani. Microstructure of thin tantalum films sputtered onto inclined substrates: Experiments and atomistic simulations. *Journal of Applied Physics*, 94 (1): 263–271, 2003.

[114] T. Smy, S. K. Dew, and R. V. Joshi. Efficient modeling of thin film deposition for low sticking using a three-dimensional microstructural simulator. *Journal of Vacuum Science & Technology A*, 19 (1): 251–261, 2001.

[115] R. Wuhrer and W.Y. Yeung. Effect of target-substrate working distance on magnetron sputter deposition of nanostructured titanium aluminium nitride coatings. *Scripta Materialia*, 49: 199–205, 2003.

[116] J. Lintymer, J. Gavoille, N. Martin, and J. Takadoum. Glancing angle deposition to modify microstructure and properties of sputter deposited chromium thin films. *Surface and Coatings Technology*, 174-175: 316–323, 2003.

[117] J. A. Thornton. Influence of substrate temperature and deposition rate on structure of thick sputtered Cu coatings. *Journal of Vacuum Science & Technology*, 12 (4): 830–835, 1975.

[118] H. C. Huang, G. H. Gilmer, and T. D. de la Rubia. An atomistic simulator for thin film deposition in three dimensions. *Journal of Applied Physics*, 84 (7): 3636–3649, 1998.

[119] H. C. Huang and G. H. Gilmer. Multi-lattice Monte Carlo model of thin films. *Journal of Computer-Aided Materials Design*, 6 (2-3): 117–127, 1999.

[120] H. Morikawa, M. Kokura, F. Iwatsu, and T. Terao. A field-ion microscope study on vapor-deposition of copper on tungsten. *Thin Solid Films*, 254 (1-2): 103–110, 1995.

[121] X. W. Zhou and H. N. G. Wadley. Hyperthermal vapor deposition of copper: athermal and biased diffusion effects. *Surface Science*, 431 (1-3): 42–57, 1999.

[122] Y. G. Yang, X. W. Zhou, R. A. Johnson, and H. N. G. Wadley. Monte Carlo simulation of hyperthermal physical vapor deposition. *Acta Materialia*, 49 (16): 3321–3332, 2001.

[123] Y. G. Yang, X. W. Zhou, R. A. Johnson, and H. N. G. Wadley. Atomistic simulations of deep submicron interconnect metallization. *Journal of Vacuum Science & Technology B*, 20 (2): 622–630, 2002.

[124] Z. L. Liu, L. Yu, K. L. Yao, X. B. Jing, X. A. Li, and X. Z. Sun. Kinetic Monte Carlo simulation of deposition of energetic copper atoms on a Cu(001) substrate. *Journal of Physics D-Applied Physics*, 38 (23): 4202–4209, 2005.

[125] J. C. S. Kools. Suppression of nanoscopic shadowing during physical vapor deposition by biased diffusion. *Journal of Vacuum Science & Technology A*, 23 (1): 85–89, 2005.

[126] B. W. Dodson. Molecular-dynamics simulation of low-energy beam deposition of silicon. *Journal of Vacuum Science & Technology B*, 5 (5): 1393–1398, 1987.

[127] J. Jacobsen, B. H. Cooper, and J. P. Sethna. Simulations of energetic beam deposition: From picoseconds to seconds. *Physical Review B*, 58 (23): 15847–15865, 1998.

[128] U. Hansen, P. Vogl, and V. Fiorentini. Atomistic modeling of large-scale metal film growth fronts. *Physical Review B*, 59 (12): R7856–R7859, 1999.

[129] X. W. Zhou and H. N. G. Wadley. Hyperthermal vapor deposition of copper: reflection and resputtering effects. *Surface Science*, 431 (1-3): 58–73, 1999.

[130] S. Hamaguchi and S. M. Rossnagel. Simulations of trench-filling profiles under ionized magnetron sputter metal-deposition. *Journal of Vacuum Science & Technology B*, 13 (2): 183–191, 1995.

[131] G. H. Gilmer and C. Roland. Simulations of crystal-growth - effects of atomic-beam energy. *Applied Physics Letters*, 65 (7): 824–826, 1994.

[132] W. F. Egelhoff and I. Jacob. Reflection high-energy electron-diffraction (RHEED) oscillations at 77 K. *Physical Review Letters*, 62 (8): 921–924, 1989.

[133] T. S. Cale and G. B. Raupp. A unified line-of-sight model of deposition in rectangular trenches. *Journal of Vacuum Science & Technology B*, 8 (6): 1242–1248, 1990.

[134] J. Dalla Torre, G. H. Gilmer, and M. Djafari Rouhani. Imperfect wetting of vapor-deposited thin films: Monte Carlo simulations and nucleation model. *Physical Review B*, 69 (195414): 1–6, 2004.

[135] G. H. Gilmer, H. C. Huang, T. D. de la Rubia, J. Dalla Torre, and F. Baumann. Lattice Monte Carlo models of thin film deposition. *Thin Solid Films*, 365 (2): 189–200, 2000.

[136] K.-H. Müller. Dependence of thin-film microstructure on deposition rate by means of a computer simulation. *Journal of Applied Physics*, 58 (7): 2573–2576, 1985.

[137] Y. G. Yang, R. A. Johnson, and H. N. G. Wadley. A Monte Carlo simulation of the physical vapor deposition of nickel. *Acta Materialia*, 45 (4): 1455–1468, 1997.

[138] T. Smy, M. Salahuddin, S. K. Dew, and M. J. Brett. Explanation of spurious features in tungsten deposition using an atomic momentum model. *Journal of Applied Physics*, 78 (6): 4157–4163, 1995.

[139] C. Busse, W. Langenkamp, C. Polop, A. Petersen, H. Hansen, U. Linke, P. Feibelman, and Th. Michely. Dimer binding energies on fcc (111) metal surfaces. *Surface Science Letters*, 539: L560, 2003.

[140] T. T. Tsong and C. L. Chen. Displacement distributions in diffusion by atomic replacement - Ir atoms on Ir surfaces. *Physical Review B*, 43 (3): 2007–2017, 1991.

[141] S. C. Wang and G. Ehrlich. Self-adsorption sites on a close-packed surface - Ir on Ir(111). *Physical Review Letters*, 62 (19): 2297–2300, 1989.

[142] M. Mueller, K. Albe, C. Busse, A. Thoma, and Th. Michely. Island shapes, island densities, and stacking-fault formation on Ir(111): Kinetic Monte-Carlo simulations and experiments. *Physical Review B*, 71 (075407): 1–8, 2005.

[143] S. K. Dew, T. Smy, and M. J. Brett. Simulation of elevated-temperature aluminum metallization using SIMBAD. *IEEE Transactions on Electron Devices*, 39 (7): 1599–1606, 1992.

[144] C. Chen and T. T. Tsong. Self-diffusion on the reconstructed and nonreconstructed Ir(110) surfaces. *Physical Review Letters*, 66 (12): 1610–1613, 1991.

[145] E. Lugscheider, K. Bobzin, N. Papenfuss-Janzen, and D. Parkot. Monte Carlo simulation of the PVD transport process for alloys. *Surface & Coatings Technology*, 200 (1-4): 913–915, 2005.

[146] A. M. Myers, J. R. Doyle, J. R. Abelson, and D. N. Ruzic. Monte Carlo simulations of magnetron sputtering particle transport. *Journal of Vacuum Science & Technology A*, 9 (3): 614–618, 1984.

[147] J. E. Greene, J.-E. Sundgren, L. Hultman, I. Petrov, and D. B. Dergstrom. Development of preferred orientation in polycrystalline TiN layers grown by ultrahigh vacuum reactive magetron sputtering. *Applied Physics Letters*, 13 (2): 3301–3304, 2003.

[148] N. N. Iosad, N. M. van der Pers, S. Grachev, M. Zuiddam, B.D. Jackson, P.N. Dmitriev, and T.M. Klapwijk. Texture-related roughness of (Nb, Ti)N sputter-deposited films. *IEEE Transactions on Applied Superconductivity*, 13 (2): 3301–3304, 2003.

[149] D. Pailharey, D. Tonneau, A. Kuzmin, R. Kalendarev, and J. Purans. Scanning probe microscopy of nanocrystalline iridium oxide thin films. *Proceedings of SPIE*, 5123: 259–265, 2003.

[150] Z. Lang and W. Xuiqin. Formation of nodular defects as revealed by simulation of a modified ballistic model of depositional growth. *Journal of Materials Science*, 33: 1487–1490, 1998.

[151] J. A. Thornton. High rate thick film growth. *Annual Review of Materials Science*, 7: 239–260, 1977.

[152] R. N. Tait, S. K. Dew, T. Smy, and M. J. Brett. Density variation of tungsten films sputtered over topography. *Journal of Applied Physics*, 70 (8): 4295–4300, 1991.

[153] J. T. Drotar, Y.-P. Zhao, T.-M. Lu, and G.-C. Wang. Surface roughening in shadowing growth and etching in 2+1 dimensions. *Physical Review B*, 62 (3): 2118–2125, 2000.

[154] J. H. Jeffries, J.-K. Zuo, and M. M. Craig. Instability of kinetic roughening in sputter-deposition growth of Pt on glass. *Physical Review Letters*, 76 (26): 4931–4934, 1996.

[155] Y.-L. He, H.-N. Yang, T.-M. Lu, and G-C. Wang. Measurements of dynamic scaling from epitaxial growth front: Fe film on Fe(001). *Physical Review Letters*, 69 (26): 3770–3773, 1992.

[156] R. M. Oeksuezoglu, A. Elmali, T. E. Weirich, H. Fuess, and H. Hahn. Evolution of surface roughness (dynamic scaling) and microstructure of sputter-deposited $Ag_{75}Co_{25}$ granular films. *Journal of Physics: Condensed Matter*, 12: 9237–9245, 2000.

[157] C. Eisenmenger-Sittner, A. Bergauer, H. Bangert, and W. Bauer. The growth dynamics of thick sputtered copper-coatings under the influence of surface diffusion: a quantitative atomic force microscopy study. *Journal of Applied Physics*, 78 (8): 4899–4905, 1995.

Lebenslauf

Börge Wessling, geboren am 16. November 1979 in Düsseldorf

Schule & Studium

1986 – 1990	Besuch der Grundschule in Bargteheide
1990 – 1999	Gymnasium Eckhorst in Bargteheide, Abschluss Abitur
1999 – 2004	Studium an der TU Hamburg-Harburg, Studiengänge Allgemeine Ingenieurwissenschaften (Abschluss Bachelor of Science) und Materialwissenschaften (Abschluss Diplom-Ingenieur)
2002 – 2004	Studium zum Master in Global Technology Management am Northern Institute of Technology, Hamburg-Harburg

Promotion

2004 – 2006	Stipendiat des Graduiertenkollegs 1035 (Biointerface) der deutschen Forschungsgemeinschaft, tätig am Institut für Werkstoffe der Elektrotechnik I der RWTH Aachen
2006 – 2007	Wissenschaftlicher Angestellter am Institut für Werkstoffe der Elektrotechnik I der RWTH Aachen